UNIVERSITY OF CALIFORNIA

Los Angeles

Metastructure-enhanced terahertz magnon-polaritons

A thesis submitted in partial satisfaction

of the requirements for the degree Master of Science

in Electrical & Computer Engineering

by

Yu Wu

2020

ABSTRACT OF THE THESIS

Metastructure-enhanced terahertz magnon-polaritons

by

Yu Wu

Master of Science in Electrical & Computer Engineering

University of California, Los Angeles, 2020

Professor Benjamin S. Williams, Chair

Magnons, *i.e.* the quanta of spin waves, are considered to be promising information carriers. Unlike electric currents, magnon-based spin currents could be used to transport information coherently over long distance without generating any Joule heat. Magnons in antiferromagnetic materials exhibit resonance frequencies extending up to the THz frequency range, which promises rapid response of magnon-based devices. However, it becomes difficult to control such rapid oscillations of magnetization using circuit-based electronic control. Instead, optical techniques have been investigated for the generation and control of AF magnons – however most techniques have been based upon ultrafast near-IR pump-probe techniques.

In this thesis, I investigate the feasibility of designing electromagnetic metastructures with subwavelength effective cavity volumes to realize strong light-matter coupling between suitable antiferromagnetic materials operating at over 1 THz. In these systems, light and material excitations are strongly coupled and mixed into superposition states with hybrid dispersion relation, which are termed as polaritons. Such magnon-polariton systems are of interest as they enable coherent information transferring between distinct physical platforms. While polaritons have been demonstrated between GHz-frequency photons and ferromagnetic magnons, only limited reports have been found on antiferromagnetic magnon-polaritons.

Moreover, as a potential application, the feasibility of THz magnon-polariton lasers is studied. In this thesis, I propose an idea which combines metal-metal waveguide with LC circuit-based microcavity, and introduce a design of metastructure with strong evanescent magnetic field, enabling the generation of magnon-polaritons even in a 200 nm thin antiferromagnetic film. Quantum cascade active region with intersubband transitions falling into THz frequency range can be applied into the metastructure, enabling direct amplification of magnon-polaritons. Magnon-polariton lasing becomes possible when this hybrid active metastructure/ antiferromganet is paired with an output coupler, building up a quantum cascaded vertical external cavity surface emitting laser (QC-VECSEL). The opportunity of magnon-polariton quantum cascade laser is also discussed when a thick antiferromagnetic slab is inserted in a standard VECSEL cavity.

The thesis of Yu Wu is approved.

Kang L. Wang

Chee Wei Wong

Benjamin S. Williams, Committee Chair

University of California, Los Angeles

2020

Table of Contents

Table of Figures

List of Tables

ACHKNOWLEDGMENTS

I would like to thank my advisor, Professor Benjamin Williams, who alway gives me great help with extraordinary patience and consistent encouragement. I want to thank my lab mates, especially Dr. Christopher Curwen, for their invaluable suggestions and willingness for discussion. I also want to thank Nezih Tolga Yardimci from Prof. Jarrahi's lab for helping me with TDS measurements.This project is in cooperation with Professor Jing Shi from University of California, Riverside, which I want to thank for their growth of antiferromagnetic materials used in our experiments. Finally, I am so grateful to my family and my boyfriend for backing me up all the time.

Chapter 1: Introduction

1.1 Polariton definition and applications

Interaction between light and matter gives rise to a wide variety of physical phenomena and has been extensively studied for centuries. The intuitive description of light-matter interaction is related to a series of elementary processes in which photons are absorbed, emitted, or scattered by an ensemble of particles in the materials. Particles could interact with each other in the ensemble, therefore any pattern of motion would be cooperative and affect the whole collection of particles in the system, which is called collective oscillations. Collective oscillations can be mechanical displacements, like lattice vibrations; they can also be electronic excitations among atomic energy levels. In either case, the whole system can be viewed as a giant harmonic oscillator contributed by all the particles in the system.

A straightforward mechanical illustration of the coupling system consists of two coupled springs (Fig. 1.1 (a)) [1]. Each single spring can be modeled as a simple harmonic oscillator. Its energy oscillates between the kinetic part and the potential part, at the same time dissipates to the environment through friction. Energy exchange between two springs becomes possible when they are connected through a third coupling spring whose elasticity coefficient decides the energy exchange rate. With the existence of the coupling spring, the oscillation modes no longer relate to the motion or position of either one of the single oscillators alone, instead, the normal modes become a hybrid of the original oscillating modes. Moreover, it's clear that when the energy exchanges between two springs in a rate slower than the rate of energy dissipating to the environment, only one-way energy transfer is observed before either one of the oscillators damps and stops moving. Only when the energy exchange rate becomes higher than the energy dissipation rate, energy oscillating between two oscillators back and forth can be observed.

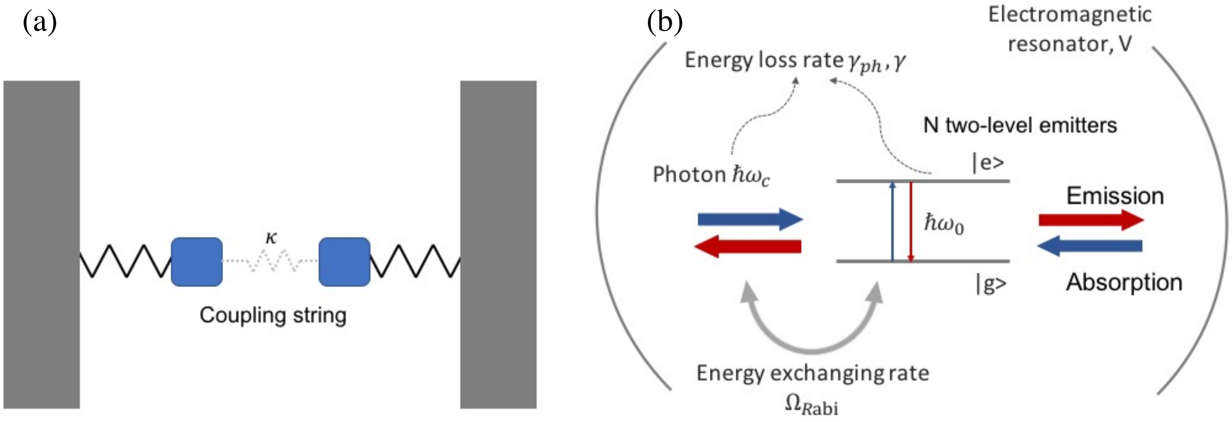

Figure 1.1 (a) Two coupled springs (b) Electric dipole coupling between photon and a two-level electronic system.

This mechanical analogy intuitively shows that whether the phenomenon of reversible energy oscillation is significant depends on the strength of coupling compared to other relevant dissipation rates. Accordingly, at least two regimes can be defined: the weak coupling regime and the strong coupling regime. In terms of light-matter coupling, the criteria of strong coupling is often worded that the reversible rate of energy transfer between the photon mode and the material excitation mode should be larger than the irreversible energy decay rate. In the strong coupling regime, the light and material excitations can not be viewed as separate entities, instead, two superposition states with hybrid dispersion relation are generated, which can be described as quasi-particles known as polaritons.

1.1.1 Classical description of strong coupling

A classical Lorentzian model can be used to describe the light-matter coupling system. Here, we take the simplest case of light-matter interaction, namely, the electric dipole coupling between photon and a two-level electronic system, as an example (Fig. 1.1 (b)). Electronic transitions between energy levels can be viewed as harmonic oscillation of electron clouds around their nucleus with oscillation frequency ω_0 and relaxation rate γ. The electromagnetic wave propagating in the medium has a wavelength much larger than the dimension of electric displacement and is in the form of $E(r,t) = E_0 e^{-i\omega t}$. It drives the movement of electrons, *i.e.* $r \propto e^{-i\omega t}$, resulting in an equation of motion:

$$m\left(\ddot{r} + \gamma\dot{r} + \omega_o^2 r\right) = -\,eE(r,t)\,. \tag{1.1}$$

The steady-state solution of equation (1.1) is written as:

$$r = -\frac{e}{m}\frac{1}{\omega_0^2 - \omega^2 - i\gamma\omega}E_0 e^{-i\omega t}\,. \tag{1.2}$$

The displacement of each electron gives rise to an electric dipole. For a medium consisting of N electrons, the macroscopic polarization in a volume of V is:

$$P = -\frac{Ner}{V} = \frac{Ne^2}{Vm}\frac{1}{\omega_0^2 - \omega^2 - i\gamma\omega}E_0 e^{-i\omega t}\,. \tag{1.3}$$

Thus the macroscopic electrical susceptibility is:

$$\chi = \frac{Ne^2}{V\epsilon_0 m}\frac{1}{\omega_0^2 - \omega^2 - i\gamma\omega} = \frac{\mu_r\omega_0^2}{\omega_0^2 - \omega^2 - i\gamma\omega}, \tag{1.4}$$

where $\mu_r = \dfrac{Ne^2}{V\epsilon_0 m\omega_0^2}$ is a parameter used to characterize the strength of material excitation contributing to Lorentzian-shaped susceptibility. In light-matter coupling system, the medium is polarized by the electromagnetic wave, while the polarization, in turn, will influence the electromagnetic field. After combing the above equation of electrical susceptibility with Maxwell's equations, we obtain the hybrid dispersion relation as:

$$\beta^2 c^2 = \omega^2 \ \big(1 + \chi(\omega)\big) = \omega^2 \ \left(1 + \frac{\mu_r \omega_0^2}{\omega_0^2 - \omega^2 - i\gamma\omega}\right). \tag{1.5}$$

To get the information of a light-matter coupling system from its dispersion relation, first an extreme case is considered when there is no dissipation, $i.e.\ \gamma = 0$. Dispersion of light in free space is linear with the expression of $\beta c = \omega$, while the electronic excitation in the medium is assumed to be dispersionless shown by the dotted lines in Figure 1.2. When the electromagnetic field is in resonance with the electronic transition, $i.e.$ around the crossing point between two original dispersions, the dispersion relation can be simplified under several approximations $\beta c + \omega \approx 2\omega_0$, $\omega_0 + \omega \approx 2\omega_0$ as [2]:

$$(\beta c - \omega)(\omega_0 - \omega) = \frac{\mu_r \omega_0^2}{4}. \tag{1.6}$$

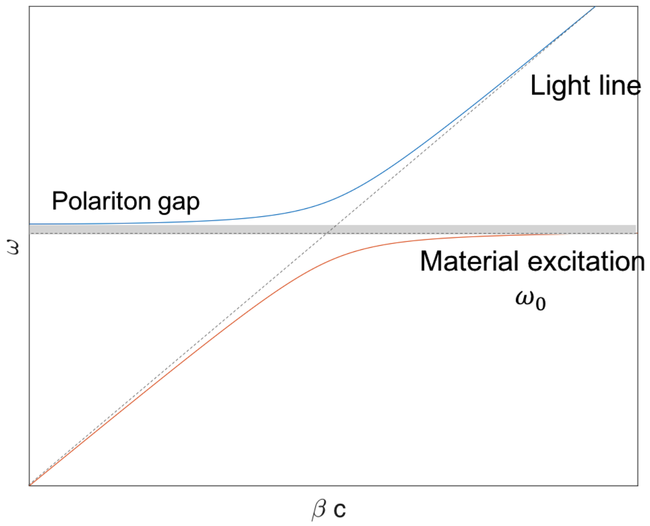

Figure 1.2. Hybrid dispersion of a strong light-matter coupling system in dissipationless case. Original dispersions of light and material excitation are represented by dotted lines. Frequency splitting at resonance and forbidden band colored in grey are signatures of strong light-matter coupling.

This equation produces two solutions, corresponding to two polariton modes with different frequencies:

$$\omega_{\pm} = \frac{\beta c + \omega_0}{2} \pm \frac{1}{2}\sqrt{\left(\beta c - \omega_0\right)^2 + \mu_r \omega_0^2}\,. \tag{1.7}$$

Either a large oscillator strength μ_r or closer resonance frequencies between light and electronic transition will lead to greater distortion of dispersion from the original ones, while as the two modes are far off-resonance, the original dispersions are recovered. The frequency splitting between normal modes at resonant point is an important parameter used to characterize the strength of coupling, and is named as Rabi splitting Ω_{Rabi}. Rabi splitting derived from classical Lorentzian model is proportional to the square root of volume density of electric dipoles which is in agreement with the quantum theory.

Moreover, a forbidden band can be found from the hybrid dispersion, when the term $1 + \frac{\mu_r \omega_0^2}{\omega_0^2 - \omega^2}$ becomes negative and only imaginary solutions of wave vector exist. The frequency range $\omega_0 < \omega < \omega_0\sqrt{1+\mu_r}$ is named as the "polariton gap" which is also a signature of strong light-matter coupling.

In the case when both electronic damping and phenomenology dissipation rate of photonic mode are taken into consideration, $i.e.\ \gamma \neq 0,\ \beta c = \beta c - i\frac{\gamma_{ph}}{2}$, the frequencies of normal modes at resonance are solved from equation (1.5) as:

$$\omega_{\pm} = \omega_0 - i\frac{\gamma}{4} - i\frac{\gamma_{ph}}{4} \pm \frac{1}{2}\sqrt{\mu_r \omega_0^2 - \left(\frac{\gamma}{2} - \frac{\gamma_{ph}}{2}\right)^2}\,. \tag{1.8}$$

The complex frequencies can be understood as damped modes with identical linewidth which is an average of the photon and material excitation modes: $\Delta\omega_{\pm} = \frac{\gamma}{2} + \frac{\gamma_{ph}}{2}$. In the experiments, to observe the frequency splitting between normal modes, the value of frequency splitting should be larger than that of the modal broadening, which leads to the relationship [2]:

$$\sqrt{\mu_r\omega_0^2 - \left(\frac{\gamma}{2} - \frac{\gamma_{ph}}{2}\right)^2} > \frac{\gamma}{2} + \frac{\gamma_{ph}}{2},$$

$$\mu_r\omega_0^2 > \frac{\gamma^2 + \gamma_{ph}^2}{2}. \tag{1.9}$$

This equation points out the condition required for strong light-matter coupling and is often worded as 'the splitting has to be larger than the widths of modes'. However, modal broadening may narrow the measured value of the splitting, and the actual measured splitting can be slightly smaller than the average width [3]. Therefore, another practical definition is usually used for the strong coupling regime which is termed as a regime with experimentally observable frequency splitting.

1.1.2 Quantum description of strong coupling

The classical model clearly demonstrates the hybrid dispersion relation with Rabi splitting in a strong light-matter coupling system. In this section, quantum mechanical description of material excitations and electromagnetic waves is introduced to better illustrate the problem.

Usually, a classical description of electromagnetic wave is used interacting with a quantum two-level system building up a semiclassical model. However, scientists found situations in which a free electromagnetic field exhibited properties and behaviors that could not be described by a classical field. Quantization of electromagnetic waves becomes necessary to build up a fully quantum framework for light-matter interaction systems, which requires the knowledge of many-body quantum physics and the technique of second quantization. Here, only the final quantum model of electromagnetic waves and main physics of light-matter coupling systems are presented, while the detailed derivation can be found in Chapter 4 of [4].

The Hamiltonian of a quantized electromagnetic wave is:

$$\hat{H}_p = \hbar\omega_c\left(\hat{\alpha}^\dagger\hat{\alpha} + \frac{1}{2}\right), \tag{1.10}$$

where ω_c is the frequency of light, $\hat{\alpha}^\dagger$, $\hat{\alpha}$ are the creation and annihilation operators whose product has an eigenvalue equals to the number of photons in the system.

This Hamiltonian is in the form of a quantum harmonic oscillator whose eigen-energies are equidistant: $E_p = \hbar\omega_c\left(n + \frac{1}{2}\right)$. Its eigenstate $|n>$ is called the "Fock" state, where n is the number of photons in the system. The $\frac{1}{2}$ term exists only in quantum theory and shows that even when there is no photon in the system, "vacuum fluctuations" leads to non-zero ground energy.

Moreover, the electric field of a single EM mode propagating along z-axis within a resonator of volume V is then expressed in quantum description as:

$$E(z,t) = \sqrt{\frac{\hbar\omega_c}{2\epsilon_0 V}}\left(\hat{\alpha}^\dagger + \hat{\alpha}\right)e^{ikz}. \tag{1.11}$$

Similar to a semiclassical model, the material excitation can be described as a quantum two-level system (spin-half system) with Hamiltonian represented by Pauli matrix as [4]:

$$\hat{H}_m = \frac{1}{2}\hbar\omega_0\hat{\sigma}_z, \tag{1.12}$$

where ω_0 is the frequency difference between the ground state and the excited state in the material.

Take the electric dipole coupling as an example, the interaction Hamiltonian can be represented as:

$$\hat{H}_{int} = -\hat{d}E(z,t), \tag{1.13}$$

in which the electric dipole matrix $\hat{d}$ in the quantum two-level system is further represented using Pauli matrices as $\hat{d} = -\left(\sigma\_M^* + \sigma_+ M\right)$, where M is the electric dipole element between the ground and excited state: $M = e < g|\hat{x}|e >$, and Pauli matrices $\sigma_- = |g >< e|$, $\sigma_+ = |e >< g|$ represent transitions between the ground and the excited state.

The final Hamiltonian of the whole system becomes:

$$\hat{H} = \frac{1}{2}\hbar\omega_0\hat{\sigma}_z + \hbar\omega_c\hat{\alpha}^\dagger\hat{\alpha} + \hbar\left(\hat{\alpha} + \hat{\alpha}^\dagger\right)\left(g\sigma_+ + c.c.\right). \tag{1.14}$$

This is the so-called quantum Rabi model introduced by Rabi around 80 years ago [5], and is considered to be one of the simplest and most fundamental models of light–matter interaction. In the strong coupling regime, rotating wave approximation can be applied considering the time evolution of operators $\hat{\alpha}, \hat{\alpha}^\dagger, \sigma_+, \sigma_-$, the quantum Rabi model is further simplified as:

$$\hat{H} = \frac{1}{2}\hbar\omega_0\hat{\sigma}_z + \hbar\omega_c\hat{\alpha}^\dagger\hat{\alpha} + \hbar\left(g\sigma_+\hat{\alpha} + c.c.\right), \tag{1.15}$$

which is called Jaynes-Cummings (JC) model, proposed by Jaynes and Cummings in 1963 [6].

$|e,n> = \begin{pmatrix}1\\0\end{pmatrix}$, $|g,n+1> = \begin{pmatrix}0\\1\end{pmatrix}$ is chosen to be the vector basis under the assumption that only one photon is considered emitting or absorbing when a transition is made between the ground and the excited states in the medium, *i.e*. the Hamiltonian only couples the states $|e,n>$ and $|g,n+1>$.

Since the state of the light field may has a distribution of photon numbers, the Hamiltonian can be written as:

$$\hat{H}_n = \sum_n \hat{H}_n,$$

$$\hat{H}_n = \hbar\left(n+\frac{1}{2}\right)\omega_c\begin{pmatrix}1 & 0\\ 0 & 1\end{pmatrix}+\frac{1}{2}\hbar\begin{pmatrix}-\delta & 2g\sqrt{n+1}\\ 2g\sqrt{n+1} & \delta\end{pmatrix},\ \delta=\omega_c-\omega_0. \quad (1.16)$$

The interaction between photon and material excitation is represented by the off-diagonal term. After rediagonalizing the Hamiltonian, energy eigenvalues are obtained as:

$$E_{n,\pm} = \hbar\left(n+\frac{1}{2}\right)\omega_c \pm \frac{\hbar}{2}\sqrt{\delta^2+4g^2(n+1)}\,. \quad (1.17)$$

The quantum Rabi model shows a similar dispersion relation as the classical Lorentzian model, while at resonance $\delta = 0$, the frequency splitting is $\Omega_{Rabi} = 2g\sqrt{n+1}$ with eigenmodes acting as a superposition of photon and material excitation, giving the definition of polaritons:

$$|\phi_{-,n}> = \frac{1}{\sqrt{2}}\left(|g,n+1> - |e,n>\right),$$

$$|\phi_{+,n}> = \frac{1}{\sqrt{2}}\left(|g,n+1> + |e,n>\right). \quad (1.18)$$

If the system is initially in the electronic ground state with $n+1$ photons, the initial state can be expressed as a superposition of the new eigenstates. Then the time-dependent wavefunction becomes:

$$|\phi(t_0)> = |g, n+1> = \frac{1}{\sqrt{2}}(|\phi_{-,n}> + |\phi_{+,n}>),$$

$$|\phi(t)> = \frac{1}{\sqrt{2}}\left(|\phi_{-,n}> e^{-i\frac{E_{n,-}}{\hbar}t} + |\phi_{+,n}>^{-i\frac{E_{n,+}}{\hbar}t}\right) = \frac{1}{\sqrt{2}}e^{i\phi}\left(|\phi_{-,n}> + |\phi_{+,n}>^{-i\Omega_{Rabi}t}\right)$$

$$= e^{i\phi'}\left(\cos(\frac{\Omega_{Rabi}}{2}t)|g, n+1> - i\sin(\frac{\Omega_{Rabi}}{2}t)|e, n>\right). \qquad (1.19)$$

The probability that the system initially in the state $|g, n+1>$ will transfer into state $|e, n>$ after a time period $t_0 - t$ under the influence of the resonant electromagnetic wave is represented as:

$$P_{a\to b}(t_0, t) = sin^2\left(\frac{\Omega_{Rabi}}{2}(t - t_0)\right). \qquad (1.20)$$

It then becomes clear that under the influence of the resonant electromagnetic wave, the eigenstates of the system are a hybrid of photon and material excitation, which means that the two-level system alternately emits photons and reabsorbs them in a rate equals to Rabi frequency. This energy exchange process between $|g, n+1>$ and $|e, n>$ states is therefore called Rabi oscillation. The criteria of strong coupling which requires the frequency splitting to be larger than the linewidths of eigenmodes, now has a physical interpretation that the energy oscillation period should be smaller than the lifetimes of both photon and material excitation states.

In the above equations, only one emitter is taking into consideration, while in real many-body system, all the N two-level emitters in the system interacting with electromagnetic wave should be taken into consideration.

$$\hat{H} = \frac{1}{2}\hbar\omega_0\sum_N\hat{\sigma}_z + \hbar\omega_c\hat{\alpha}^\dagger\hat{\alpha} + \hbar\left(g\sum_N\sigma_+\hat{\alpha} + c.c.\right). \qquad (1.21)$$

This is the so-called Dicke Hamiltonian which is also known as the Tavis–Cummings Hamiltonian. When only a few emitters in the system are excited, the contribution of single excited emitter can be viewed as the collective excitation of all the emitters in the system, while a quantum harmonic oscillator can be introduced to describe this collective excitation, with another set of creation and annihilation operators $\hat{\beta}^{\dagger}$, $\hat{\beta}$. After Holstein–Primakoff transformation:

$$\sum_N \hat{\sigma}_+ = \hat{\beta}^{\dagger}\left(N - \hat{\beta}^{\dagger}\hat{\beta}\right)^{1/2},$$

$$\sum_N \hat{\sigma}_- = \left(N - \hat{\beta}^{\dagger}\hat{\beta}\right)^{1/2}\hat{\beta},$$

$$\sum_N \hat{\sigma}_z = \hat{\beta}^{\dagger}\hat{\beta} - \frac{N}{2}. \tag{1.22}$$

The final Hamiltonian is expressed as [4]:

$$\hat{H} \simeq \hbar\omega_0\left(\hat{\beta}^{\dagger}\hat{\beta} - \frac{N}{2}\right) + \hbar\omega_c\hat{\alpha}^{\dagger}\hat{\alpha} + \hbar g\sqrt{N}\left(\hat{\alpha}^{\dagger}\hat{\beta} + c.c.\right). \tag{1.23}$$

This is the quantum equivalent of two coupled harmonic oscillators, with a Rabi splitting now shows a relationship proportional to the square root of number of emitters in the system, as well as the strength of electric field and electric dipole moment, where the $\sqrt{\frac{N}{V}}$ dependence is exactly what we get using classical Lorentzian model if the overlapping between light and material excitation modes are assumed to be unity.

$$2\Omega_{Rabi} = 2g\sqrt{N}\sqrt{n+1},\ g \propto M\sqrt{\frac{\omega_0}{V\hbar\epsilon_0}}. \tag{1.24}$$

Moreover, in the special case when $n = 0$, *i.e.* no photon in the system, vacuum fluctuations enable the emitter coupling with quantized electromagnetic field in an empty cavity. The frequency splitting in this case is therefore called vacuum Rabi splitting with eigenstates named as cavity polaritons. According to the relationship $\frac{1}{2}\epsilon_0 E_{vac}^2 V_{cav} = \frac{1}{2}\hbar\omega_c$ in the vacuum state, the cavity is expected to have small volume and high quality factor to support strong light-matter coupling. The exploration of different kinds of electromagnetic resonators to modulate the coupling strength between light and materials gives birth to a whole new field of research called cavity quantum electrodynamics (QED).

In 1946, Purcell found that the strength of interaction can be modified by engineering the electromagnetic environment, *i.e.* putting the emitter in an electromagnetic resonator [7]. The existence of cavity could structure the optical density of states and lead to modified spontaneous emission rate, however, the emission frequency remaining unaltered.

Since then, the resonators have been developed with higher quality factors and lower energy losses. In 1983, Haroche experimentally demonstrated the vacuum Rabi oscillation, using a collection of two-level Rydberg atomic systems coupling to a single mode electromagnetic wave in a high-Q millimeter-wave cavity [8].

Since this first observation, strong light–matter coupling was soon realized experimentally between single atom and a microwave cavity [9] as well as in the optical range both for several atoms [10] and for a single atom [11]. Following these pioneering experiments, cavity QED has been further developed using artificial atoms, such as quantum dots or superconducting qubits. Quantum dots have much smaller mode volumes compared with Fabry–Perot optical resonators and have been strongly coupled to the field of photonic-crystal-slab nanocavity [12], micropillar [13], and micro-disk [14]. Superconducting two-level system has been experimentally demonstrated coupling to an on-chip cavity consisting of a superconducting transmission line resonator. This system is expected to promote possible applications in quantum information and computation [15].

Today, strong coupling can be achieved in much simpler systems and offers the possibility of a wide range of practical applications, such as modifying and controlling the chemical reaction rate [16], boosting conductivity in organic semiconductors [17], enhancing high-harmonic generation efficiency by modifying nonlinear optical susceptibility [18], enabling room-temperature Bose–Einstein condensate and novel coherent light sources [19, 20], etc. [21].

So far, the cavity-enhanced strong coupling has been realized between light and a diverse range of material excitations including excitons [22], plasmons [23], phonons [24], magnons [25], intersubband transition dipoles [26], etc. In this thesis, the focus will be on the generation of THz magnon-polaritons using carefully designed electromagnetic structures, and the possible application of novel THz magnon-polariton lasers going through intersubband transitions will be exploited.

1.2 Overview and introduction of magnon-polariton

1.2.1 Definition of magnon

In the past century, semiconductor based electronics have been developed rapidly in information science and technology. However, the scaling trends which have driven these advances are slowing down as small size of transistor introduces quantum limitation, and the huge Joule heat generated by flowing electrons prevents the improvement of integrated level. As scientists work to break the bottleneck, they surprisingly find that only one of the fundamental properties of electron was used, *i.e.* its charge. Spin, another inherent property of electron, has been almost neglected and is expected to be a promising option to power the next wave of electronics. Spin current carried by magnons is therefore considered to be a promising information carrier which is free from the drawbacks inherent to modern electronics, such as dissipation of energy due to ohmic losses.

Magnons are the collective excitation states of magnetic material. To understand the physical picture of magnon, a simple ferromagnet is taken as an example with all the N spins aligned in their ground states [27]. Only exchange interaction between the nearest neighbor spins is taken into consideration with a Hamiltonian written as:

$$\hat{H_{int}} = -\frac{1}{2}\left(2J\sum_{i,j}^{N}\hat{\mathbf{S}}_i\hat{\mathbf{S}}_j\right), \tag{1.25}$$

where J is the nearest-neighbor exchange integral of the wave functions between atoms at lattice point i and j with spin angular momentum operators $\hat{\mathbf{S}}_i$, $\hat{\mathbf{S}}_j$. The $\frac{1}{2}$ factor is introduced because the interaction between the same two spins is counted twice in the summation.

If one of the spins is flipped over, the system gains energy and enters the first excited state. Due to the exchange interaction between neighboring spins, the deviation of one spin from its equilibrium state will lead to the deviation of all the adjacent spins, giving rise to a so called spin wave throughout the whole lattice. Therefore, instead of only one spin flips over while all the other spins stay unchanged, the real microscopic picture includes all the spins in the crystal precessing along the original orientation but with a phase shift. The energy of spin wave is quantized with the unit of energy called magnon, which is similar to the definition of phonon describing all the atoms vibrating as a lattice wave throughout the whole crystal.

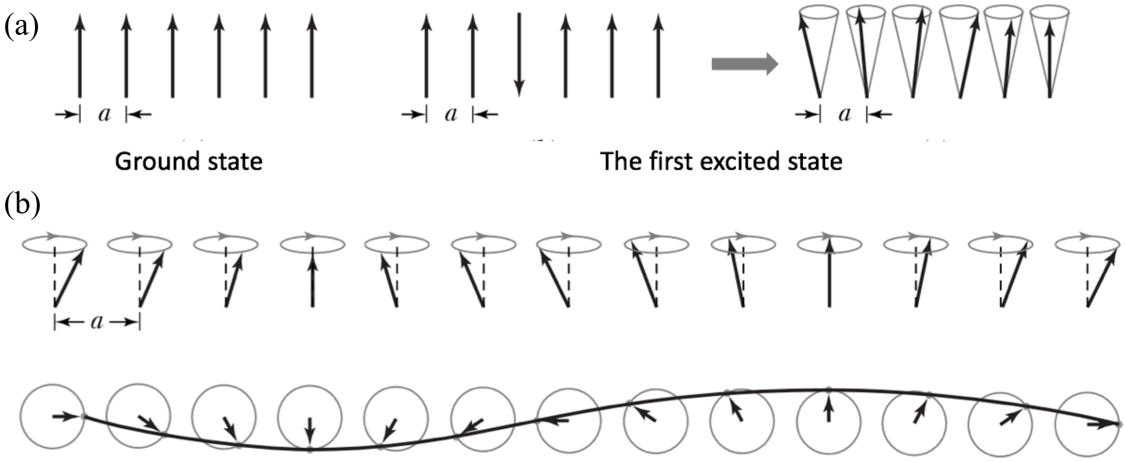

Figure 1.3 (a) Spin alignment in one-dimensional ferromagnet at ground and excited state. (b) Sketch of spin wave [27].

In the above simplified one-dimensional model, all the spins are assumed to be lined up. But in a real crystals, there is another energy term which directs the magnetization along certain crystallographic axis, *i.e.* the direction of easy magnetization, which ensures that the crystal is magnetized with lowest energy. The directional dependence of magnetic properties is known as magnetic anisotropy.

Since the first concept of magnon was introduced by Felix Bloch in 1930 [28], its properties have been widely studied, promoting various range of potential applications [29, 30]. For example, (1) a spin wave has both amplitude and phase which enables operations with vector variables rather than scalar variables. If instead of an electron, a spin wave is used as a data carrier, an additional degree of freedom can be introduced in data processing process with fewer processing elements needed, which benefits the idea of magnonic logic circuits [31, 32]. (2) The magnon spectrum covers the GHz frequency range used nowadays in communication and radar systems [33], and it reaches into the very promising THz range [34, 35]. This inherent frequency enables high clock rate and computing speed of magnon-based devices which could respond very rapidly to external stimuli. (3) Ultrafast coherent control of magnons using external electromagnetic field has been experimentally demonstrated, enabling the development of magnon spintronics not only in magnetic metals or semiconductors but also in magnetic dielectrics [36, 37].(4) Spin waves have a wavelength limited by the lattice constant of a magnetic material, which is orders of magnitude smaller than electromagnetic waves at the same frequency. A shorter wavelength enables the design of micro- or even nanometer-sized elements for data processing or spintronics [38, 39].

1.2.2 Previous studies on ferromagnetic/antiferromagnetic magnon-polaritons

Systems with strong light-matter interaction enable coherent information transfer between distinct physical platforms – a concept at the core of quantum information processing. In contrast to electrical dipole coupling, magnetic coupling between photon and spin system has been mostly ignored, due to typically much weaker magnetic component of the electromagnetic field, before scientists found out the significance of magnon in quantum information processing .

Strong light-matter interaction between ferromagnets and light was predicted theoretically in 2010 [40, 41] while the experimental demonstrations were soon after reported around 2013 using microwave cavity photons and magnons in yttrium iron garnet (YIG) [25, 42]. Rabi-like oscillation was observed through vector network analysis, demonstrating the generation of cavity magnon-polaritons. YIG is one of the prime platforms for studying FM magnon-polaritons due to its long magnon lifetime, high spin density and flexibility in fabrication. Its magnon frequency can be tuned from a few hundred MHz to GHz frequency range with the applied external magnetic field. Many interesting dynamic features including Rabi oscillation, magnetically induced transparency, Purcell effect and ultrastrong coupling have been demonstrated using YIG, promoting the development of ferromagnetic magnon-polariton study [43].

The earliest experimental demonstration for the existence of magnon-polaritons in antiferromagnets was reported by Sanders *et al.* in 1978 [44] using iron fluoride (FeF_2) with magnon mode resonant at 1.58 THz. More recently, scientists have turned their attention to antiferromagnetic spintronics attracted by its high-frequency nature of spin waves and the wide array of antiferromagnetic insulators [45]. In 2010, Kampfrath *et al.* used ultrashort THz pulses to exert direct control over antiferromagnetic magnons in nickel oxide coherently [36]. There have also been demonstrations of the inverse Faraday effect [46, 47] and nonlinear spin control [48, 49] based on THz antiferromagnetic magnons. However, the study of antiferromagnetic spintronics and antiferromagnetic magnon-polaritons is still in its infancy compared with ferromagnetic based research. One of the major challenges comes from a lack of appropriate THz sources and detection techniques. Also, generally, magnons in antiferromagnets couple more weakly to magnetic fields compared with that in ferromagnets, which makes them harder to excite and detect. Moreover, a cavity-enhanced version is harder to achieve due to the additional requirement of a highly confining THz cavity. So far, only a few reports have been found on magnon-polaritons using antiferromagnetic rare-earth orthoferrite materials at a sub-THz frequency [50-52].

1.2.3 Approach to THz antiferromagnetic magnon-polaritons

In this thesis, we will focus on antiferromagnetic magnons, not only to compensate for the lack of studies in this area, but also for the following benefits provided by antiferromagnetic materials [53]:

1) It's easier to achieve an antiferromagnetic order in semiconductors than a ferromagnetic order, which is compatible to both electronics and spintronics devices.

2) The absence of net angular momentum makes antiferromagnets more insensitive to external magnetic field. It results in orders of magnitude faster antiferromagnetic spin dynamics, and characteristic frequency of antiferromagnetic resonance operating beyond GHz frequency range (as ferromagnets) and reaching THz range.

Here, several antiferromagnetic insulators are taken into consideration with magnon frequency falling into THz frequency range.

Iron(II) fluoride FeF_2 is a classic uniaxial antiferromagnet with rutile-structure (Fig. 1.4 (a)). Below its Neel temperature $T_N = 78$ K, the transition-metal-ion Fe^{2+} spins align along the (001)-axis of the crystal with those at the cell corners antiparallel to those on the body-centered to produce overall antiferromagnetic arrangement of spins. The antiferromagnetic magnon located around 1.6 THz has been observed experimentally using far-infrared transmission spectroscopy, Raman scattering, or inelastic neutron scattering [54-56] at liquid helium temperature, and the signal decays as well as the linewidth broadens rapidly with the increase of temperature.

As I have discussed in Section 1.1, a classical Lorentzian oscillator model is introduced to describe the magnon-photon coupling system. Here, I provide a detailed derivation of a model

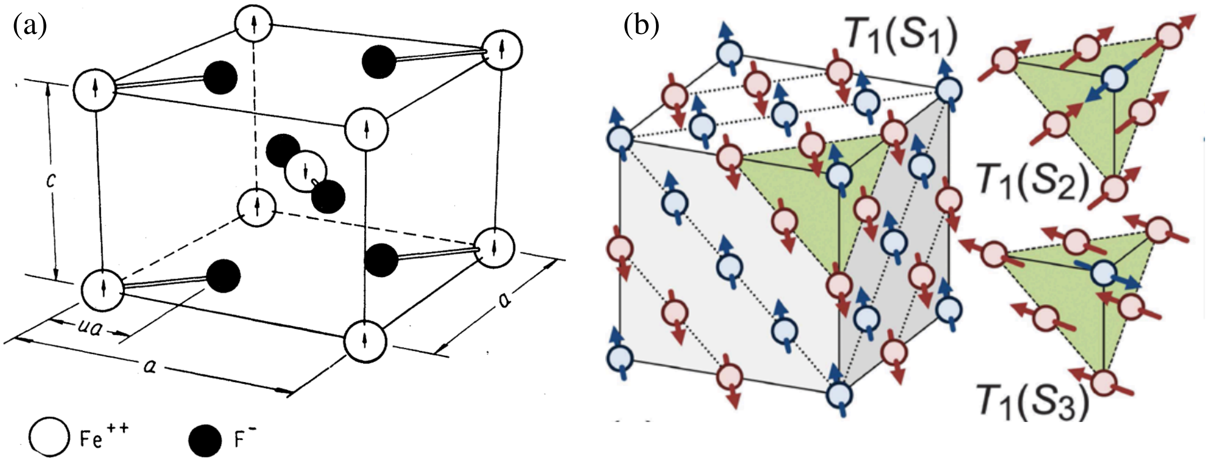

Figure 1.4 (a) Crystal structure of uniaxial antiferromagnet FeF_2 showing antiferromagnetic spin arrangement [54] and (b) easy-plane antiferromagnet NiO with antiferromagnetic spin alignments in three S domains belonging to the T1 domain [60].

for magnon-polaritons in simple uniaxial antiferromagnets, like MnF_2 or FeF_2, which was first introduced by C. Manohar [57].

Starting with the Hamiltonian:

$$H = -J\sum_{i,j}^{N} \boldsymbol{S}_i \boldsymbol{S}_j - \gamma\left(\sum_{i}^{N} \boldsymbol{S}_{iz} - \sum_{j}^{N} \boldsymbol{S}_{jz}\right)\boldsymbol{H}_{\boldsymbol{A}} - \gamma\left(\sum_{i} \boldsymbol{S}_{\boldsymbol{i}} + \sum_{j} \boldsymbol{S}_{\boldsymbol{j}}\right)\boldsymbol{H}_{\boldsymbol{ext}}, \quad (1.26)$$

where $\gamma = \frac{g\mu_B}{\hbar}$, the subscripts i and j label the spins on the two sublattices pointing to antiparallel directions respectively.

The first term in the equation describes the exchange interaction between the adjacent spins. The second term accounts for the magnetic anisotropy, where $\boldsymbol{H}_{\boldsymbol{A}} = H_A \boldsymbol{z}$ denotes the anisotropic field which directs spins along z axis, *i.e*, (001)-axis of the uniaxial crystal. The last term describes the interaction between magnetic moment and external magnetic field.

The Hamiltonian can be rewritten in the form of $H = -\boldsymbol{\mu_i B_{eff}} = -\gamma \sum_i \boldsymbol{S_i B_{eff}}$, where the overall effects of the second sublattice on the first sublattice can be summarized into an effective magnetic field:

$$\boldsymbol{B_{eff}} = \frac{J}{\gamma}\sum_j^n \boldsymbol{S_j} + \boldsymbol{H_A} + \boldsymbol{H_{ext}}, \tag{1.27}$$

where n is the number of nearest neighbors for any S_i. Spins on each set of sublattice can be further expressed by the macroscopic magnetization defined as the volume density of magnetic moments associated with spins, *i.e.* $\boldsymbol{M_{1,2}} = \frac{\gamma \sum_{i,j}^N \boldsymbol{S_{i,j}}}{V}$. Then equation (1.27) can be rewritten as:

$$\boldsymbol{B_{eff}} = \frac{JnV}{\gamma^2 N}\boldsymbol{M_2} + \boldsymbol{H_A} + \boldsymbol{H_{ext}} = \lambda \boldsymbol{M_2} + \boldsymbol{H_A} + \boldsymbol{H_{ext}}, \tag{1.28}$$

where $\lambda = \frac{JnV}{\gamma^2 N}$.

To excite a magnon from its equilibrium state, this external magnetic field should have a component perpendicular to z axis, *i.e.* $\boldsymbol{H_{ext}} = H_{ext,x}\boldsymbol{x} + H_{ext,y}\boldsymbol{y}$. Excited spin fluctuations associated with spin waves are of small amplitude, therefore $M_{1,2;z}$ is assumed to be fixed which represents the saturation magnetization of each sub lattice $M_s = -M_{1z} = M_{2z}$. λM_{2z} is then the exchange field in the equilibrium state, and is denoted as H_E, similarly, $\lambda M_{1z} = -H_E$ considering antiparallel magnetization direction.

The equation of motion for spins on each sublattice is written as:

$$\frac{d\boldsymbol{M_1}}{dt} = -\gamma \boldsymbol{M_1} \times \left(\lambda \boldsymbol{M_2} + \boldsymbol{H_A} + \boldsymbol{H_{ext}}\right), \tag{1.29}$$

$$\frac{d\boldsymbol{M_2}}{dt} = -\gamma \boldsymbol{M_2} \times \left(\lambda \boldsymbol{M_1} - \boldsymbol{H_A} + \boldsymbol{H_{ext}}\right), \tag{1.30}$$

which can be decomposed in component form as:

$$\dot{M}_{1x} = -\gamma \left[M_{1y}(H_E + H_A) + M_s(\lambda M_{2y} + H_{ext,y})\right], \tag{1.31}$$

$$\dot{M}_{1y} = -\gamma \left[-M_{1x}(H_E + H_A) - M_s(\lambda M_{2x} + H_{ext,x})\right], \tag{1.32}$$

$$\dot{M}_{1z} = 0, \tag{1.33}$$

$$\dot{M}_{2x} = -\gamma \left[-M_{2y}(H_E + H_A) - M_s(\lambda M_{1y} + H_{ext,y})\right], \tag{1.34}$$

$$\dot{M}_{2y} = -\gamma \left[M_{2x}(H_E + H_A) + M_s(\lambda M_{1x} + H_{ext,x})\right], \tag{1.35}$$

$$\dot{M}_{2z} = 0. \tag{1.36}$$

Excited by the external electromagnetic field, all the magnetization components are in the form of $\propto e^{i(\boldsymbol{kr}-\omega t)}$, where in the long-wave approximation *i.e.* the wavelength of light is much larger than the dimension of spin fluctuations, all the spins are assumed in phase.

Sum equation (1.31) and (1.34), while subtract equation (1.32) and (1.35), we get:

$$-i\omega\left(M_{1x} + M_{2x}\right) = -i\omega M_x = -\gamma\left(M_{1y} - M_{2y}\right)H_A, \tag{1.37}$$

$$-i\omega\left(M_{1y} - M_{2y}\right) = -\gamma\left[-(M_{1x} + M_{2x})(H_E + H_A) - M_s(\lambda(M_{1x} + M_{2x}) + 2H_{ext,x})\right]. \tag{1.38}$$

Substitute the equation (1.38) into equation (1.37), we get the magnetic response of an anti-ferromagnetic material to external electromagnetic field as:

$$M_x = \frac{2\gamma^2 M_s H_A}{\omega^2 - \gamma^2 H_A\left(2H_E + H_A\right)} H_x, \tag{1.39}$$

where the resonance frequency of antiferromagnetic magnon is therefore:

$$\omega_{AFMR} = \gamma\sqrt{H_A\left(2H_E + H_A\right)}\ . \tag{1.40}$$

With H_A = 200 kOe, H_E = 540 kOe in FeF_2 [54], magnon frequency calculated from the Lorentzian model is 1.59 THz, which is in good agreement with experimental results.

Considering phenomenological magnon decay term, the final expression for magnetic susceptibility is:

$$\chi_x = \chi_y = \frac{2\gamma^2 M_s H_A}{\omega^2 - \omega_{AFMR}^2 - \frac{i\omega}{\tau_{magnon}}},\ \chi_z = 1. \tag{1.41}$$

Even though FeF_2 shows antiferromagnetism at a really low temperature and the magnon frequency is slightly lower than the working frequency of common THz quantum cascade laser, it is considered to be a good platform to study strong light-matter coupling benefited by its large spin density, or equivalently saturation magnetization M_s = 560 Gauss. The existence of magnon-polaritons has been demonstrated in Ref. [44] with the experimental observation of "polariton gap".

The second material taken into consideration is the easy-plane antiferromagnet NiO, in which anisotropic field aligns Ni^{2+} spins in parallel within {111} planes with adjacent planes oppositely magnetized, and pointing along the ⟨11-2⟩ axes. There are four diagonals in the unit cell which defines four equivalent easy-planes and divides the crystal in to four twin (T) domains. These micrometer-order domains are randomly distributed. In each T domain, there are further three possible ⟨11-2⟩ directions and is defined as S domains (Fig. 1.4 (b)).

NiO has been widely used in THz spintronics benefited by its room-temperature antiferromagnetism ($T_N = 523$ K) [36], with a magnon resonance around 1 THz [58, 59], which is, however, too low for any intersubband transition. Moreover, the overall magnetic response in polycrystal NiO becomes isotropic but weaker, considering the coherent superposition and averaging over twelve variant domains with spins pointing to different equilibrium directions [60].

CoO is another kind of easy-plane antiferromagnet with positive and negative spins aligning alternatively on every other {111} planes and pointing to ⟨11-7⟩ directions. Its magnon mode has been experimentally demonstrated both far-IR [61] and Ramen active [62] around 4.3 THz at liquid helium temperature. Even though the Neel temperature of CoO approaches room temperature with $T_N = 289$ K, the intensity and lifetime of its magnon mode decrease rapidly and become unobservable when temperature approaches 200 K [63], which makes the properties of magnon and magnon-photon interaction much less exploited in CoO, compared with room-temperature antiferromagnet NiO. However, the high magnon frequency of CoO makes it compatible with intersubband transition-based THz sources and is therefore considered to be a promising antiferromagnetic material for the study of THz magnon-polariton quantum cascade laser.

Orthoferrite $RFeO_3$ is another kind of antiferromagnetic materials, where R can be any rare-earth element, such as Y, Tm, Dy, Gd, Ho, Er, Tb. Orthoferrite is classified as weak ferromagnet because the antiferromagnetically ordered spins cant toward one direction leading to a macroscopic magnetization. This unique spin orientation generates two optically-active magnon modes in the sub-THz frequency region [64]. The polarization and temperature dependences of magnon modes, as well as room-temperature antiferromagnetism make orthoferrite an attractive candidate in the study of sub-THz spintronics [46-48] and sub-THz magnon-photon coupling system [50-52].

Some of the properties of different antiferromagnetic materials are summarized in Table 1.1 which will be further discussion in the main text. μ_r and Q_m are the oscillator strength and quality factor used to characterize the intensity and lifetime of magnon mode in a classical Lorentzian mode, as derived in equation (1.4): $\chi = \dfrac{\mu_r \omega_{AFMR}^2}{\omega_{AFMR}^2 - \omega^2 - i\omega_{AFMR}\omega / Q_m}$.

	FeF_2	**NiO**	**CoO [61]**	**$DyFeO_3$ [64]**
Permittivity (THz)	5.2	10 [111]	14.44	24
Absorption coefficient (THz)	Neglected in thin film	8 cm^{-1} [111]	11 cm^{-1}	$\epsilon'' = 0.20$
$\omega_{AFMR}/(2\pi)$	1.58 THz	1.1 THz	4.44 THz	510 GHz
μ_r	0.011	0.0197 [110]	0.00045	0.0007
Q_m	230 [44]	100 [110]	20	48
T_N	78 K	523 K	289 K	645 K
Availability	Thin film grown by MBE	Commercial thick crystal	Commercial thick crystal	Commercial thick crystal

Table 1.1 Properties of different antiferromagnetic materials.

1.3 Introduction of polariton lasers

1.3.1 Introduction of Bose-Einstein condensation and polariton laser

Polaritons, as quantized quasi-particles used to describe the strong light-matter coupling system, are bosons, which exhibit unique properties and potential applications other than fermions, e.g. electrons. One of the potential applications is a novel type of coherent light source—polariton laser, which has raised great attention due to its ultra-low lasing threshold and has been studied in various polariton systems.

The fundamental of polariton laser lies on the coherent nature of Bose condensates of bosonic polaritons. As given in equation (1.42), once the separation between each particle becomes smaller compared with their thermal de Broglie wavelengths, their wavefunctions will overlap and indistinguishabily become relevant, making the ensemble of particles looks like a single entity with all the particles staying in the same state.

$$n_v > \lambda_{dB}^{-3},\ \lambda_{dB} = \sqrt{\frac{2\pi^2\hbar^2}{m^* k_B T}}. \tag{1.42}$$

To achieve the condition of Bose-Einstein condensation, either the density of particles has to be increased to decrease their separation, or the temperature has to be decreased, so the momentum of particle deceases with increased de Broglie wavelength.

In solid-state systems, excitons in semiconductors have been considered promising candidates for Bose-Einstein condensation, since excitons are light-mass bosons which enable the realization of BEC at lower density or equivalently higher temperature. For the same reason, exciton-polaritons are also widely studied, because compared with excitons, the mass of exciton-polaritons is dominated by its photon part which results in a polariton mass orders of magnitude lighter than the exciton one. Therefore, polaritonic condensates can exist at much higher temperatures (few hundreds of Kelvin) than excitonic ones and have been observed in several material systems.

In contrast to thermal equilibrium Bose-Einstein condensates, systems are driven far from equilibrium in matter lasers or polariton lasers. In 1996, Imamoglu *et al*. proposed such a novel type of exciton-polariton laser, bridging the relationship between a thermal equilibrium BEC and a nonequilibrium traditional photon laser which requires electronic inversion [19]. A polariton laser works mainly via two processes: first, a large number of bosons condense into a macroscopically occupied coherent quantum state via stimulated scattering, e.g. acoustic and optical phonon scattering or polariton-polariton scattering; then, the condensate of polaritons goes through spontaneous radiative decay and provides coherent emission of light. The working mechanism of polariton laser is different compared with conventional laser device, which does not rely on population inversion but on bosonic final-state stimulation. Bosonic final-state stimulation describes that, in a bosonic system, the probability of transition toward a final state is proportional to the population of said state [65]. This property is in contrast to the behavior of fermions, whose scattering is Pauli blocked by final-state occupation. Polariton lasing happens when the stimulated scattering time toward the coherent ground state, *i.e.* state of condensates, is shorter than the lifetime of the final state. In this case, the population is built up abruptly, with the output power expressed as [66]:

$$P_{out} = \frac{\hbar \omega N}{\tau_{rad}} S, \tag{1.43}$$

where ω is the frequency of radiation, N is the sheet density of polaritons in the final state, τ_{rad} is the radiative lifetime of the final state, and S is the device surface area.

Owing to its working mechanism, a polariton laser promises a more energy-efficient laser operation. The low lasing threshold is inherited from the light mass of polaritons, which allows the formation of condensates at modest particle densities, while the actual threshold is determined by the details of device dynamics, such as pumping schemes or polariton decay rates including cavity decay rate of photon mode and the excitonic spontaneous emission to all other radiation field modes. Another pronounced advantage of polariton laser is based on the one-to-one correspondence between polaritons and the spontaneously emitted photons which carry direct information of the polaritons. Therefore, the quantum statistical properties of the emission intensity provide a direct insight into the instantaneous polariton distribution. What's more, the half-matter nature makes polariton laser a unique platform to study many-body theories and cavity quantum electrodynamics, especially in the system with high density polaritons.

An early experimental demonstration of exciton-polariton laser was performed by Hui Deng *et al.* in 2003 using optical pumping at a temperature of 4 K, where the threshold pump intensity was proven one or two orders of magnitude lower than that needed for a normal photon laser in the same structure [67]. In order to further promote the practical use of energy-efficient polariton lasers, there are several requirements have to be taken into consideration. The first essential is the coherence of the emitted radiation which is inherited in Bose condensates based polarton lasers. The second requirement is the room-temperature operation, which has been demonstrated in 2007 in an optically pumped polariton laser [20], benefited by the high exciton binding energy of GaN which stabilizes the quasi-particles beyond the thermal energy of 25 meV at 300 K. Finally, a laser that is driven by another pump laser is limited in its applicability, which makes electrical pumping become necessary. And the electrically pumped polariton laser was demonstrated until 2013, using GaAs-based quantum well microcavity diode at cryogenic temperature [68, 69]. Further implementing such electrically pumped devices into material systems with large exciton binding energies, such as GaN, ZnO, promotes the development of electrically pumped polariton lasers for room temperature applications, and has been observed in a bulk GaN-based microcavity diode at a wavelength around 365 nm [70].

1.3.2 Intersubband-polariton and intersubband-polariton laser

As a limitation of exciton-polariton lasers, the density of exciton-polaritons cannot be chosen at will and is limited by the so called Mott transition density. Above that density, excitons or exciton-polaritons, cannot be considered as bosons anymore since the interparticle distance becomes comparable to the Bohr radius of the exciton (a_B). As the exciton character of the polariton becomes negligible, an exciton–polariton laser is expected to continuously transform to a standard photon laser with electronic inversion in requirement again [71]. Mott transition density of excitons is decided by different material systems and thus puts an intrinsic upper limit to the maximum operating temperature, via equation (1.42), and also to the output power of polariton laser as indicated by equation (1.43).

Intersubband-polaritons, whose material component is the intersubband transition dipole, are also considered to be promising platforms. Intersubband transitions are supported by semiconductor heterostuctures with periodic series of well and barrier materials of only a few monolayers thicknesses. The alternatively varying material composition forms a electric potential varying spatially along the growth direction, which acts as one-dimensional quantum wells. Electronic motion is therefore confined by these quantum wells with eigen-energies quantized into discrete electronic subbands.

Compared with exciton-polaritons, intersubband-polaritons have much more design flexibility benefited by the tailorable intersubband transition energy over a broad frequency range just by engineering layer thicknesses, which enables the realization of coherent mid-IR and promising THz semiconductor light source. What's more important, the upper density limit is not fixed by Mott density as excitons. Instead, it can be engineered to a large extent by electronic doping. In fact, the maximum doping level is limited by the sheet electronic doping concentration at which the higher energy state of intersubband transition starts to be filled with electrons, which naturally increases with the transition frequency.

Intersubband-polaritons with hybrid dispersion were first observed in the mid-IR range using a resonator based on total internal reflection [72], while the realization of ISB polaritons in THz frequency range is enabled by metal-dielectric-metal microcavity supporting high confinement optical mode [26]. Potential applications of ISB polaritonic devices working in strong light-matter coupling regime have been widely studied, including mid-IR ISB polariton light-emitting devices (LED) [73], optically and electrically pumped THz polariton emitters [74, 75], midinfrared photodetectors [76, 77] and ultrafast optical modulation [78, 79]. Highly doped ISB polariton systems also offer the access to ultrastrong light-matter coupling regime, where new quantum phenomena and applications would occur [80, 81].

The roadmap towards the development of ISB polariton lasers was introduced by R. Colombelli in 2015 [66], where ISB polariton lasers are expected to be able to operate at room temperature and become relatively high output power devices benefitted by high doping level. Optical pumping is preferred over electrical pumping, because the presence of dark states which do not couple to electromagnetic field will dramatically reduce the quantum efficiency of an electrical injection process, leading to only a small fraction of electrons injected into the bright polaritonic states since a narrow spectral-width injector which selectively injects electrons to the bright polariton states is hard to achieve. Dispersive metal-dielectric-metal resonator with positive, parabolic dispersion is depicted in Fig. 1.5 (a). Such microcavities, supporting mid-IR and THz electromagnetic waves, are extremely practical due to their compatibility with both optical pumping and electrical injection, as well as pump-probe measurement.

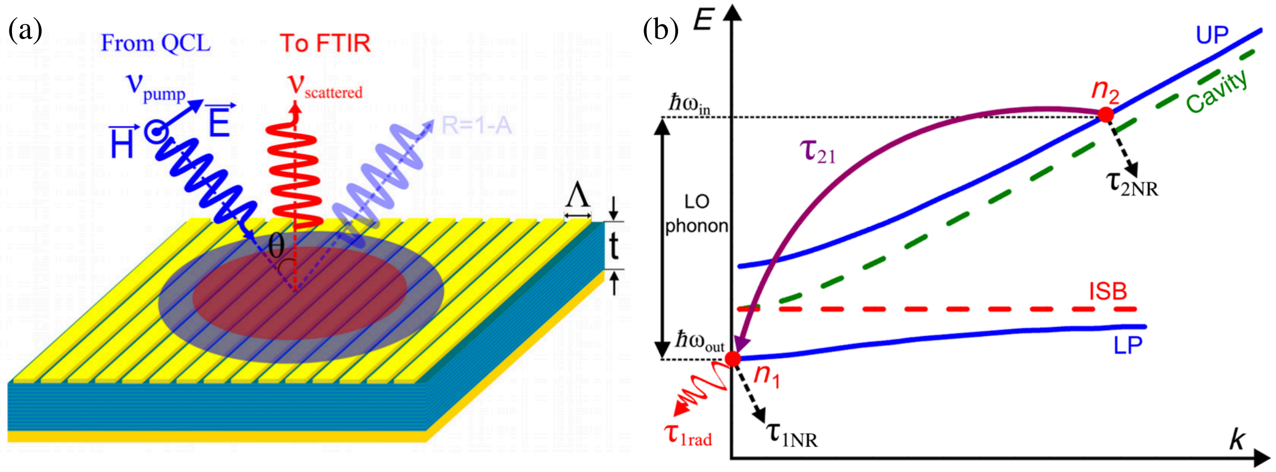

Figure 1.5 (a) Schematic view of grating based metal-active region-metal resonator [82]. (b) Hybrid dispersion of intersubband-polaritons with the solid lines represent the two polariton states, and the dashed lines are the bare cavity and ISB modes. The various loss channels as well as the LO phonon assisted scattering mechanism are symbolized by arrows, which are relevant to the operation of a bosonic laser. [66]

The working principle of ISB polariton lasers is based on several processes depicted in Fig. 1.5 (b). First, a polariton is optically pumped resonantly into the upper polariton branch. Then, it scatters into a final state in the lower polariton branch with the assistance of a longitudinal optical phonon which is typically the most important scattering channel affecting semiconductor intersubband transitions. The generation of polariton condensates is the key process of a polariton laser, and has been carefully studied both theoretically based on bosonic final-state simulation [82] and experimentally [83], followed by spontaneous radiative decay of lower branch polaritons, giving out coherent radiation. An estimate polariton lasing threshold intensity on the order of 70 kW/cm^2 was predicted by R. Colombelli [83], which is an important step towards the hopefully forthcoming demonstration of an intersubband-polariton laser.

1.3.3 Idea of phonon-polariton quantum cascade laser

Just recently, J. Faist's group has invented the first electrically pumped phonon-polariton laser which instead of photons, phonon-polaritons are emitted coherently in the quantum cascade structure [84].

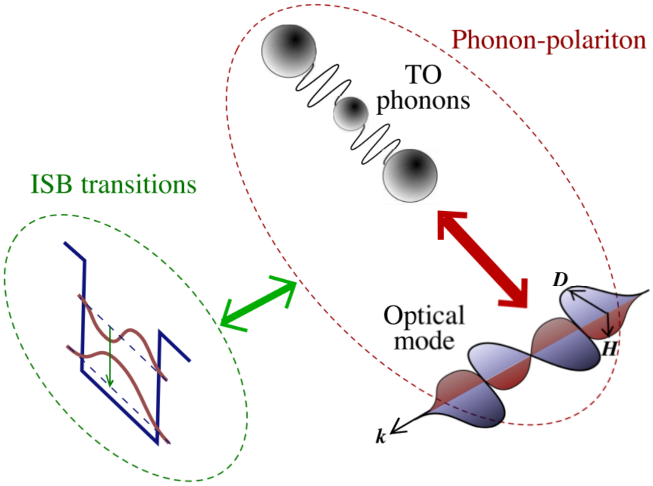

Figure 1.6 Schematic microscopic picture of phonon-polariton laser involving an unique tripartite coupling, where the red arrow symbolizes the strong coupling between cavity photons and TO phonons which generates phonon-polaritons, and the green arrow symbolizes the weak interaction between the phonon-polaritons and the ISB transitions that provides the laser gain [85].

In the system, both cavity photons and intersubband transition dipoles are carefully designed in resonance with transverse optical phonons within the semiconductor material, therefore, a unique tripartite coupling is achieved and is indicated in Figure 1.6 [85]. Optical cavity modes strongly couple with TO phonons and create phonon-polaritons, while phonon-polaritons only weakly interact with the ISB transitions. Optical gain is provided through ISB transitions mainly into the photon component of the phonon-polaritons, leading to lasing of phonon-polaritons with a phonon fraction up to 65%.

One of the promising features of intersubband systems carried by semiconductor quantum well heterostructures is that it can be electrically pumped to provide optical gain. Electrons going through intersubband transitions could tunnel along the growth direction under external bias into the next module, causing the emission of multiple photons with the injection of a single electron. Once population inversion between two subbands is built up through suitable design of layer thicknesses, compositions and doping, optical gain can be achieved in the intersubband system, giving rise to the so-called quantum cascade active region and quantum cascade laser, which have been widely studied with a much higher quantum efficiency and thus higher output power compared with semiconductor laser diodes based on interband transitions.

In the implementation of the intersubband transition based phonon-polariton laser in Ref. [84], a quantum cascade active region composed of InGaAs/AlInAs is designed based on a bound-to-continuum transition scheme to provide gain for intersubband transition at a wavelength of 26.3 μm (11 THz); phonon excitation is naturally confined within the AlInAs layers and the phonon mode participating in the strong coupling is the TO phonon of AlAs; the photonic part of polariton is guided along metal-insulator-metal waveguide which has been widely used for quantum cascade lasers [86]. High conductivity metal layers both on top and bottom of the active region enable the confinement of light in a resonator with very small effective cavity volume, resulting in high overlapping integral and low waveguide loss.

The realization of electrically pumped phonon-polariton quantum cascade laser has been experimentally demonstrated though the direct observation of the photon, phonon, and polariton signatures of the emission. Compared with exciton-polariton and intersubband-polariton lasers, where the coherent emission of light is based on an effect closely related to Bose-Einstein condensation, this kind of phonon-polariton laser works in a way similar as traditional photon lasers, in which case population inversion among electronic states is still required, and coherent radiation of phonon-polaritons is achieved.

Moreover, the idea of phonon-polariton quantum cascade laser can be applied and extended to any other types of designs and material systems, for example, magnetic materials with magnetic excitations. In this thesis, I will seek the possibility of a similar magnon-polariton quantum cascade laser based on the novel realization of tripartite intersubband-magnon-photon coupling. Specifically, antiferromagnetic insulators supporting magnon modes with resonance frequency falling into QCL working frequency are carefully chosen, while a special design of hybrid antiferromagnetic/electromagnetic structure is exploited for the realization of strongly-coupled magnon-polaritons.

Chapter 2: Electromagnetic structure supporting magnon-polariton: Split ring resonator

2.1 Introduction of split ring resonator

Considering the light-matter interaction, magnetic contribution is usually neglected, because the effect of light on the magnetic permeability is orders of magnitude weaker than the electric permittivity. To enhance the magnetic response, artificially structured materials with assemblies of meta-atoms called metamaterials have been introduced to provide new electromagnetic properties not available in naturally found materials, like negative refractive index [87]. Similarly, metasurfaces are artificially designed two-dimensional metastructures with subwavelength thickness. An array of split ring resonators (SRR) is one typical example of magnetic metasurface which provides artificial magnetic response built from nonmagnetic conducting elements [88, 89].

A SRR consists of a high-conductivity metal ring that acts as an effective inductor, and a gap introduced into the metal ring that acts as an effective capacitor. This makes SRR equivalent to a LC circuit that shows a resonant magnetic response at $\omega_0 = \dfrac{1}{\sqrt{LC}}$. If the electromagnetic wave illuminating the SRR array has an electric field component perpendicular to the metal gap or a magnetic field component perpendicular to the metasurface plane, the resonant LC mode can be excited. At resonance, induced current flows circularly around the metal ring, which in turn, generates an enhanced electric field within the metal gap, and a magnetic field along the horizontal direction. The enhanced field decays rapidly away from the SRR plane. In the THz frequency range, this near field extends only several microns in the horizontal direction, which provides a small effective cavity volume and highly-confined photon mode.

The resonant field enhancement and subwavelength field localization provided by split ring resonators enable the realization of strong or even ultrastrong light-matter coupling when the dielectric containing material excitations is put in proximity. The choice of SRR geometry plays an important role in engineering the LC resonance frequency, coupling strength and radiative decay rates, makes it a good platform to investigate the hybrid dispersion relation and criteria of strong light-matter coupling system. SRR-enhanced light-matter strong coupling has been demonstrated in a wide range of material systems, such as two-dimensional electron gas (2DEG) with cyclotron transitions [90, 91]; intersubband dipoles in quantum wells [92, 93]; infrared active phonons in SiO_2 film [94]; ferromagnetic magnons in yttrium iron garnet (YIG) films [95, 96]. Moreover, SRR arrays have also been investigated in antiferromagnetic systems, where the resonantly-enhanced magnetic field enables the study of antiferromagentic magnon excitation and nonlinear magnetization dynamics [97, 98].

In this chapter, strong light-matter coupling between SRR-enhanced THz cavity photons and antiferromagnetic magnons are exploited using thin-film of antiferromagnetic FeF_2 with AF magnon mode at 1.6 THz. First, the geometry of high conductivity SRR array is carefully designed and its effects on LC resonance frequency, quality factor and light-matter coupling strength are characterized theoretically, followed by the fabrication and experimental measurements of SRR array with the optimum geometry. Rabi splitting observed in simulated transmission spectra demonstrates the realization of strong coupling between highly-confined THz photons and AF magnons in hybrid SRR/FeF_2 structure.

2.2 HFSS simulations and characterization

Strong light-matter interaction enhanced by metallic U-shaped SRR has already been demonstrated to provide increasing quality factor and near-field enhancement with decreasing gap width between two metal arms at near-infrared frequency range [99]. Here, the geometry dependence of quality factor as well as the light-matter coupling strength are theoretically studied at THz frequency range, and the optimum design parameters are carefully chosen.

Numerical simulations are performed based on a commercial finite element method solver (HFSS). The computational space is separated by SRR array into two parts, vacuum on one side and substrate on the other side. The coordinate is chosen so that SRR array is located in the x-y plane with y-axis pointing along the metal arms. The simulation unit contains a single SRR element, while considering the tradeoff between quality factor and signal strength or signal-to-noise ratio (SNR), the dimension of each unit is chosen to be 40 μm × 25 μm in order to reduce the effects of mutual coupling between neighboring elements and also avoid any lattice surface mode [93].

The SRR array is modeled by 200 nm thick gold whose electrical permittivity is described by Drude model:

$$\sigma(\omega) = \frac{ne^2\tau}{m^*(1 - i\omega\tau)}, \ \epsilon(\omega) = \epsilon_{core} + i\frac{\sigma}{\omega}, \tag{2.1}$$

where $m*$ is the effective carrier mass, ϵ_{core} is the core permittivity excluding free carrier contributions, n and τ are the free carrier density and relaxation time respectively. In the simulation, the doping concentration of high conductivity gold is assumed to be 5.6×10^{22} cm^{-3} with relaxation time of 39 fs.

The SRR array is deposited on top of dielectric substrate consisting of 200 nm thick antiferromagnetic FeF_2 film and around 500 μm thick MgF_2 substrate. The dielectrics are assumed to be frequency and temperature independent with optical properties fitting the room-temperature THz experimental results shown in section 2.3 as $\epsilon_{FeF_2} = 5.2$; $\epsilon_{MgF_2} = 4.71$, $\alpha_{MgF_2} = 6$ cm^{-1}, which are close to the optical properties obtained experimentally in Ref. [100, 101]. Periodic boundary conditions are applied to the four sidewalls of simulation unit under the assumption that the THz spot size is much smaller than the dimension of metasurface. Electric field pointing perpendicular to the metal arm, *i.e.* x-polarized, is incident from the top boundary, while the reflection from the back facet is neglected to get rid of extra dispersion brought by FP oscillations.

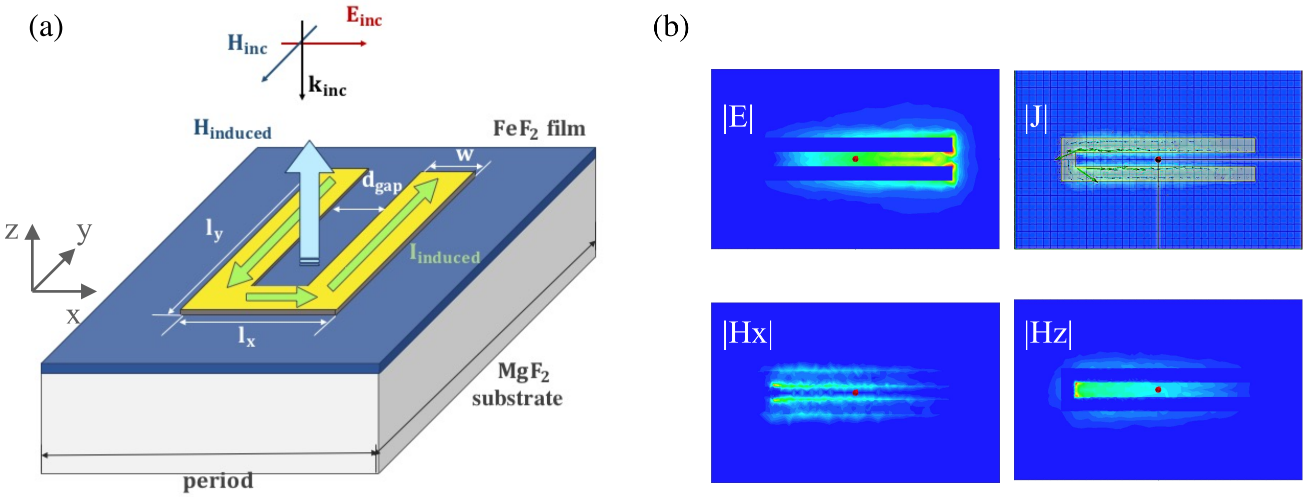

Figure 2.1 (a) Schematic view of a U-shaped split-ring resonator and the incident field polarization configuration. (b) Electric field, magnetic field and current distributions at the resonance frequency for SRR with dimension of $l_y = 28$ μm, $d_{gap} = 2$ μm, $w = 2$ μm.

The metallic U-shaped SRRs with defined geometry parameters are schematically depicted in Fig. 2.1 (a). While the electric field, magnetic field and current distributions within SRR at resonance frequency are plotted in Fig. 2.1 (b), demonstrating circulating current along the metallic split ring, which excite electric field strongly confined between the tips of metal arms, and surrounding magnetic field mainly in z and x directions.

The geometry parameters determine the resonance frequency and quality factor of the LC resonant mode carried by SRR. First, the effect of gap width between two metal arms (d_{gap}) is investigated. The gap width is varied in the simulation, while the SRR arm length (l_y) is changed correspondingly to maintain the resonance frequency at 1.6 THz, *i.e.* $d_{gap} = 1\ \mu$m, $l_y = 28\ \mu$m; $d_{gap} = 2\ \mu$m, $l_y = 27\ \mu$m; $d_{gap} = 4\ \mu$m, $l_y = 26\ \mu$m; $d_{gap} = 8\ \mu$m, $l_y = 24.5\ \mu$m, and the arm width is fixed in all the simulations as $w = 2\ \mu$m.

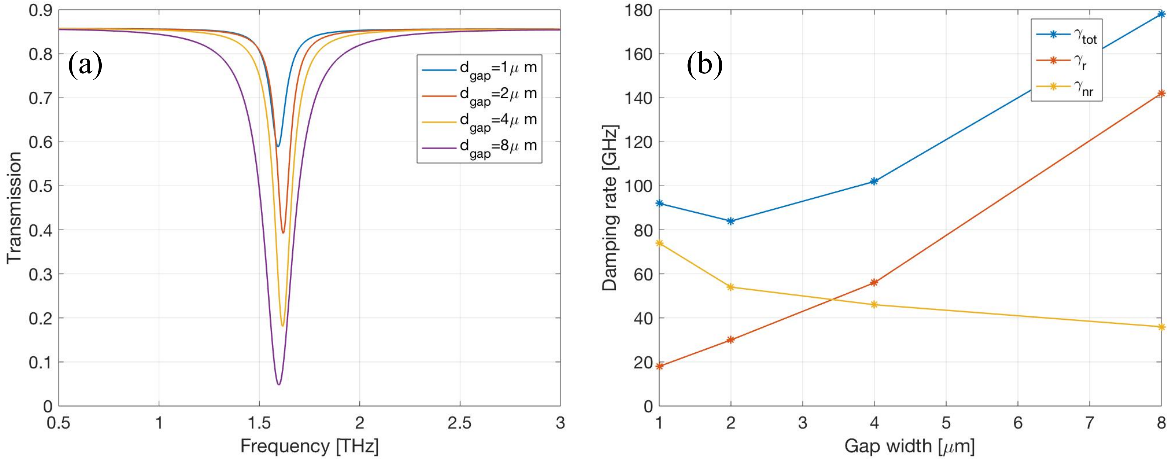

Figure 2.2 (a) The simulated transmission spectra of U-shaped SRRs with different gap widths but the same LC resonance frequency around 1.6 THz. (b) Different damping rates with respect to gap width.

Transmission spectra are plotted in Fig. 2.2 (a), which show that in the case when there is no magnon mode excited at room temperature, the increasing gap width between two metal arms results in the full width half maximum (FHWM) of transmission dips to be 92 GHz, 84 GHz, 102 GHz, 178 GHz respectively, contributed by absorption loss in metal and lossy substrate as well as radiative loss. In order to distinguish the relative value of each damping rate, the metallic array is further modeled as perfect electrical conductor (PEC) and the substrate is also assumed to be lossless, in which case only the radiative loss is included in the FHWM. Fig. 2.2 (b) plots the radiative loss and non-radiative loss with respect to gap width, with their values summarized in Table 2.1. It is now clear that, as the separation between two metal arms increases, the radiative loss dramatically increases while the non-radiative loss, which is mostly contributed by the metallic absorption, keeps decreasing, leading to the optimum quality factor at a gap width around 2 μm.

d_{gap}	γ_{tot}	γ_{rad}	γ_{nr}	Ω_r
1 μm	92 GHz	18 GHz	74 GHz	65 GHz
2 μm	84 GHz	30 GHz	54 GHz	58 GHz
4 μm	102 GHz	56 GHz	46 GHz	53 GHz
8 μm	178 GHz	142 GHz	36 GHz	47 GHz

Table 2.1 Different damping rates of the LC resonant mode and the Rabi splitting of hybrid system with respect to gap width between SRR arms.

The reason can be explained as that the anti-parallel currents in two SRR arms cancel each other, giving rise to nearly no electric dipole radiation and thus the net electric dipole moment is mainly contributed from the SRR base-line, *i.e.* l_x. Therefore, SRR with larger gap width or equivalently longer base-line, will contribute to more radiative loss [99]. Also, as the gap width between two SRR arms becomes super narrow, like in the case of $d_{gap} = 1$ μm, the highly confined subwavelength optical field will be forced penetrating into the lossy metallic regions, resulting in higher metallic loss.

Then, the gap width d_{gap} is fixed at 2 μm, while the width and length of metal arms are changed as w = 1 μm, l_y = 26.5 μm; w = 2 μm, l_y = 27 μm; w = 3 μm, l_y = 27.5 μm; w = 4 μm, l_y = 28 μm, maintaining the resonance frequency at 1.6 THz. Transmission spectra are plotted in Fig. 2.3 (a). The radiative and non-radiative losses of the LC resonant mode in each geometry are obtained in the similar way. The values are summarized in Table 2.2 and their dependences on the arm width are plotted in Fig. 2.3 (b).

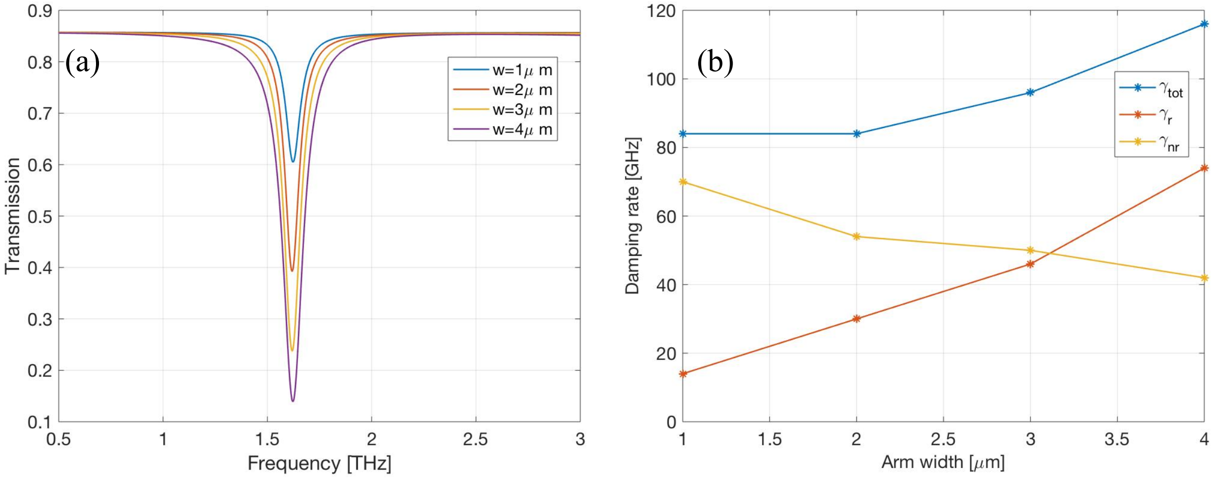

Figure 2.3 (a) The simulated transmission spectra of U-shaped SRRs with different arm widths but the same LC resonance frequency around 1.6 THz. (b) Different damping rates with respect to arm width.

w	γ_{tot}	γ_{rad}	γ_{nr}	Ω_r
1 μm	84 GHz	14 GHz	70 GHz	64 GHz
2 μm	84 GHz	30 GHz	54 GHz	58 GHz
3 μm	96 GHz	46 GHz	50 GHz	57 GHz
4 μm	116 GHz	74 GHz	42 GHz	54 GHz

Table 2.2 Different damping rates of the LC resonant mode and the Rabi splitting of hybrid system with respect to SRR arm width.

As the width of SRR arms increases, the radiative loss as well as the total damping rate increases, resulting in decreasing quality factor. This relationship agrees with the expression of quality factor in a series LC resonant circuit which is proportional to $\sqrt{\frac{L}{C}}$, as the inductance carried by a metallic strip will decrease with the increase of its width. Also, the metallic loss coming from the metallic inductor is proportional to $\frac{l_{ind}}{w}$ and will decrease with increasing arm width, which is in agreement with the simulated non-radiative damping rate.

Once the system is cooled down to liquid helium temperature, the antiferromagnetic magnon modes in FeF_2 film beneath the SRR array become active and will interact with the highly-confined cavity photons resonant at the same frequency. A Lorentzian-shaped magnetic excitation is therefore included to describe the optical property of FeF_2 film in HFSS simulations. The equilibrium magnetization direction of FeF_2 points to y-axis, in parallel with SRR arms, in order to interact with the induced magnetic field in x and z directions.

$$\chi_{mag} = \begin{bmatrix} \frac{2\gamma^2 M_s H_A}{\omega^2 - \omega_{AFMR}^2 - \frac{i\omega\omega_{AFMR}}{Q_{magnon}}} & 0 & 0 \\ 0 & 1 & 0 \\ 0 & 0 & \frac{2\gamma^2 M_s H_A}{\omega^2 - \omega_{AFMR}^2 - \frac{i\omega\omega_{AFMR}}{Q_{magnon}}} \end{bmatrix} \tag{2.2}$$

Where ω_{AFMR} = 1.6 THz is the AF magnon frequency in FeF_2, Q_{magnon} characterizes the lifetime of magnon mode and is assumed to be $Q_{magnon} = 230$ [44], M_s = 560 Gauss, H_A = 200 kOe are provided by [54].

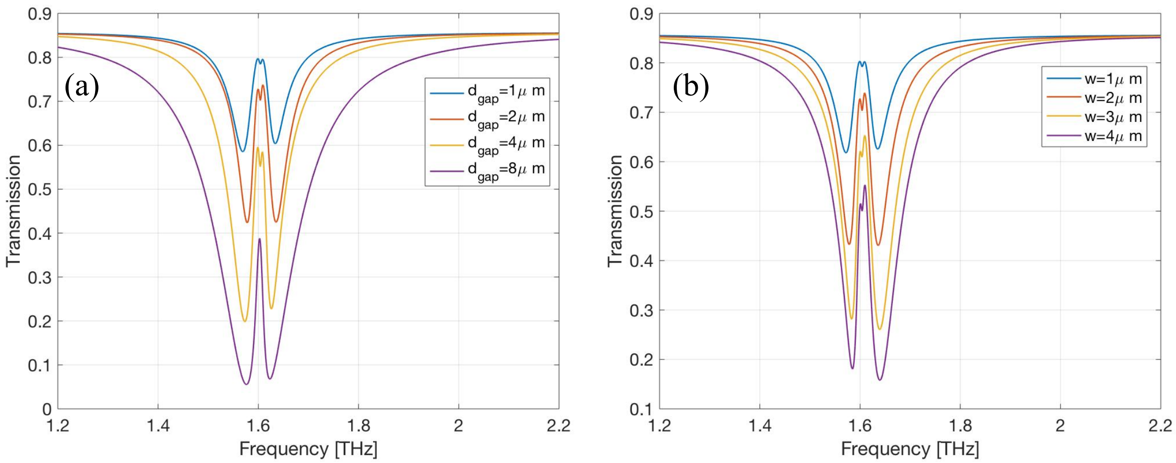

Figure 2.4 The simulated transmission spectra of U-shaped SRRs with different gap widths (a) and arm widths (b) but the same LC resonance frequency around 1.6 THz when magnon modes are excited in FeF_2 film and couple with strongly-localized photon modes.

Figure 2.4 plots the transmission spectra of hybrid SRR/FeF_2 system in the case when the arm width is fixed and gap width is varied (Fig. 2.4 (a)), and when the gap width is fixed and arm width is varied (Fig. 2.4 (b)). Frequency splitting between two resonant modes shown in the spectra demonstrates the realization of strong coupling between AF magnons and cavity photons even in the SRR designed with low quality factor. The values of Rabi splitting provided in the tables show downtrend with respect to the increase of gap width and arm width, which are supposed to be determined by the overlapping factor between LC resonant mode and antiferromagnetic film in each SRR design, and also slightly affected by the values of damping rates. The highest achievable Rabi splitting between photons and AF magnons in FeF_2 is around 166 GHz, decided by the equation (1.6) and the oscillator strength of magnon mode in FeF_2. However, the simulated Rabi splitting in the hybrid SRR/FeF_2 system is around 50-60 GHz, implying that the overlapping factor with the ultra-thin FeF2 film is no more than 15%.

2.3 Fabrication

Following the analyses above, both metal gap width and SRR arm width are chosen as small as possible to enlarge the light-matter coupling strength. While considering the photolithography limitation, the geometry of SRR is designed to have a gap width and arm width of 2 μm with arm length tuned from 25 μm to 28 μm. Each design shows slightly different LC resonance frequency which enables the exploration of hybrid dispersion relation around the resonance point.

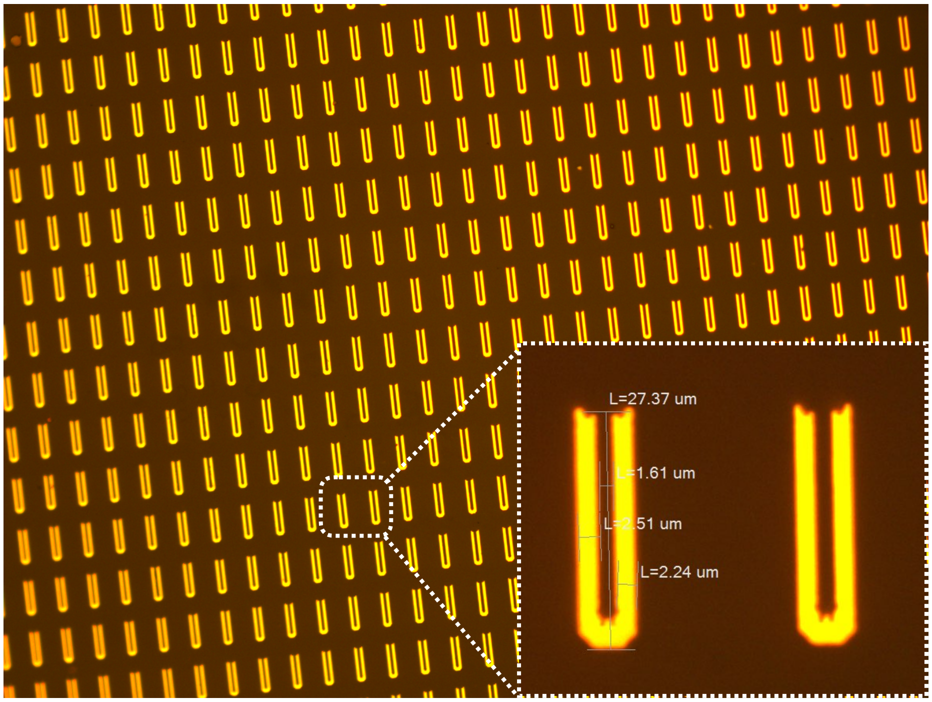

Figure 2.5 Metallic split ring resonator pattern under microscope. The designed pattern has a gap width of 2 μm and arm length of 28 μm, while the inset shows the exact dimension.

Negative photoresist nlof 2020 is used in the photolithography process, followed by 200 nm Ti/Au layer deposited through e-beam evaporation. The final metallic SRR pattern under microscope is depicted in Figure 2.5. During the photolithography process, there is more diffracted light around the corners and tips of the SRR pattern, which strengthens the negative photoresist there and leads the weird shape and shorter effective arm length compared with the designed pattern. This deviation can be improved by carefully controlling the exposure time and development time during photolithography process or deliberately compensating for the light diffraction during photomask design.

2.4 Experimental results

First, the optical properties of MgF_2 substrate are characterized through its transmission spectra plotted in Fig. 2.6 (a). The blue line is measured using house-made THz time-domain spectroscopy (TDS) with a resolution of 4 GHz by Nezih Tolga Yardimci from professor Mona Jarrahi's lab, while the orange line shows the experimental result measured by Nicolet Fourier Transform Infrared (FTIR) spectrometer with a resolution of 0.5 cm^{-1} (15 GHz), a liquid helium cooled bolometer is used as the detector which is required to obtain sufficient detectivity at a frequency around 1.6 THz, and the obtained spectra are averaged over 30 scans. Both experiments are done at room temperature, with the incident electric field perpendicular to the (001) axis of (110)-oriented MgF_2 crystal. The transmission spectrum measured by FTIR reveals a low signal-to-noise ratio below 1 THz due to the lack of power intensity of light source at low frequency range, which is in opposite to the TDS measurement, while around the target frequency of 1.6 THz, both measurements give out similar spectra. Fig. 2.6 (b) provides the FTIR experimental spectrum zoomed in 1.2 THz ~ 2 THz frequency range, and an analytical fitting is applied with the expression:

$$t = \frac{4n}{(n+1)^2 e^{-in\frac{\omega}{c}d-\alpha/2d} - (n-1)^2 e^{in\frac{\omega}{c}d+\alpha/2d}}, \ T = |t|^2 \qquad (2.3)$$

The room temperature optical properties of MgF_2 substrate around 1.6 THz are therefore obtained as $n_{MgF2}^2 = \epsilon_{MgF_2} = 4.71$, $\alpha_{MgF_2} = 6$ cm^{-1}, considering the thickness of MgF_2 slab measured to be $d = 523$ μm using micrometer. As the frequency increases, the transmission signal keeps decreasing, demonstrating an increasing absorption coefficient of MgF_2 with respect to frequency.

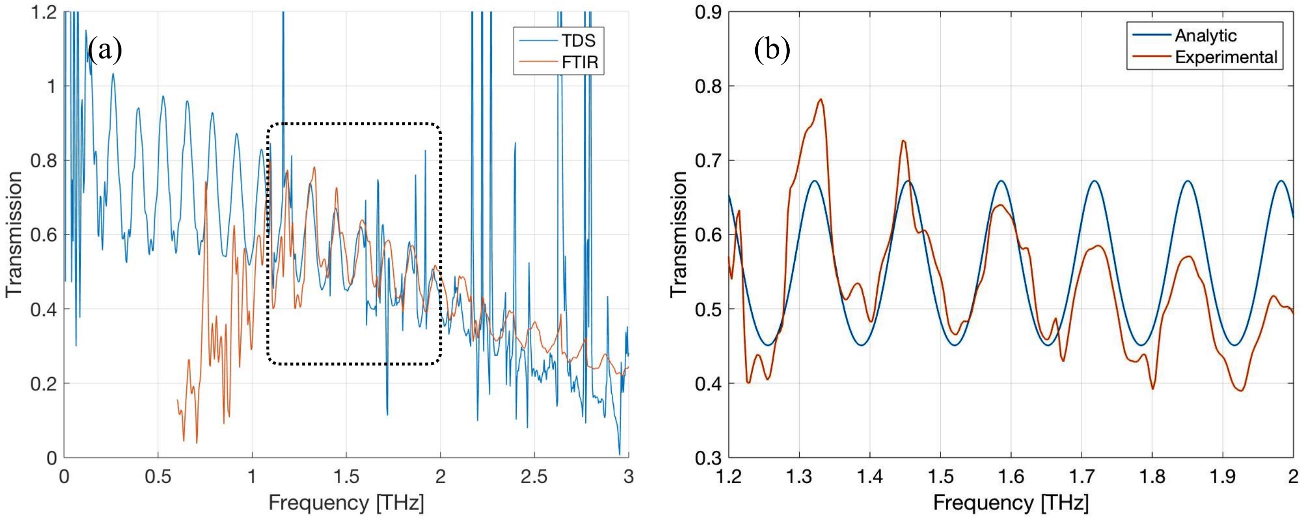

Figure 2.6 (a) Transmission spectra of MgF_2 slab measured by TDS (blue) and FTIR (orange) at room temperature and (b) spectrum zoomed in 1.2 THz~2 THz frequency range (dotted box). Blue line is the analytic fitting of orange FTIR experimental result.

The transmission spectra of U-shaped SRRs deposited on bare MgF_2 substrate are measured by both TDS and FTIR at room temperature as shown in Fig. 2.7 (a) with the dimension of SRR as $l_y = 28$ μm, $d_{gap} = w = 4$ μm. The experimental results roughly fit, while TDS measurement provides higher SNR.

Thin antiferromagnetic FeF_2 films used in the experiments have a thickness around 200 nm and is grown on thick commercial MgF_2 substrate by Professor Jing Shi's research group from UC Riverside using molecular beam epitaxy. Both FeF_2 film and its substrate are (110)-oriented,

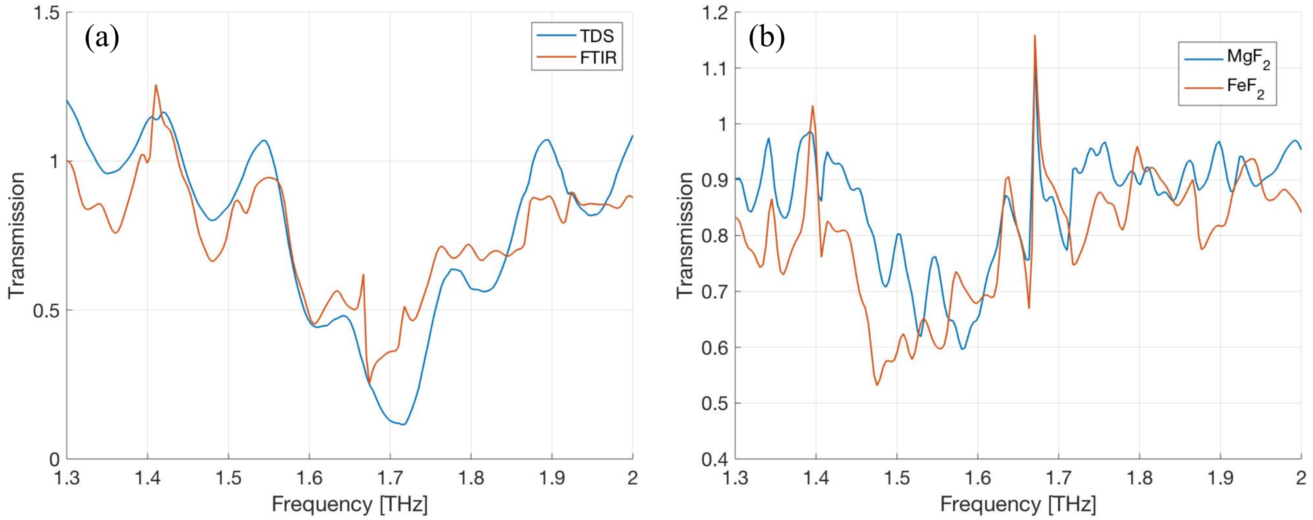

Figure 2.7 (a) Transmission spectra of hybrid U-shaped SRR/FeF$_2$ measured by TDS (blue) and FTIR (orange) at room temperature. (b) Transmission spectra of U-shaped SRRs with the same dimension deposited directly on top of MgF$_2$ substrate (blue) and on FeF$_2$ film grown on MgF$_2$ substrate (orange).

and the metallic SRR array is deposited directly on top of FeF$_2$ with metal arms pointing to its (001)-direction, *i.e*. y-axis in the coordinate defined in Fig. 2.1 (a). The incident wave has a polarization perpendicular to the metal gap, which induces the LC resonant mode and the excited localized metamaterial plasmons then radiate SRR-enhanced evanescent magnetic field perpendicular to the (001)-axis. We have discussed in Section 1.2.3 that the external magnetic field with a component perpendicular to the orientation of Fe^{2+} spins in their equilibrium state could excite AF magnon mode in FeF$_2$. However, all the spectra provided in this thesis are measured at room temperature—well above the Neel temperature of FeF$_2$—therefore, no spin fluctuation can be observed and the absorption dips belong to metasurface resonant modes. As plotted in Fig. 2.7 (b), the transmission spectra of SRR array deposited directly on MgF$_2$ substrate is compared with that deposited on FeF$_2$ film supported by MgF$_2$ substrate, while the SRR arrays have the same dimension: $l_y = 28\ \mu$m, $d_{gap} = w = 2\ \mu$m. Even though there is no signature of AF magnons in

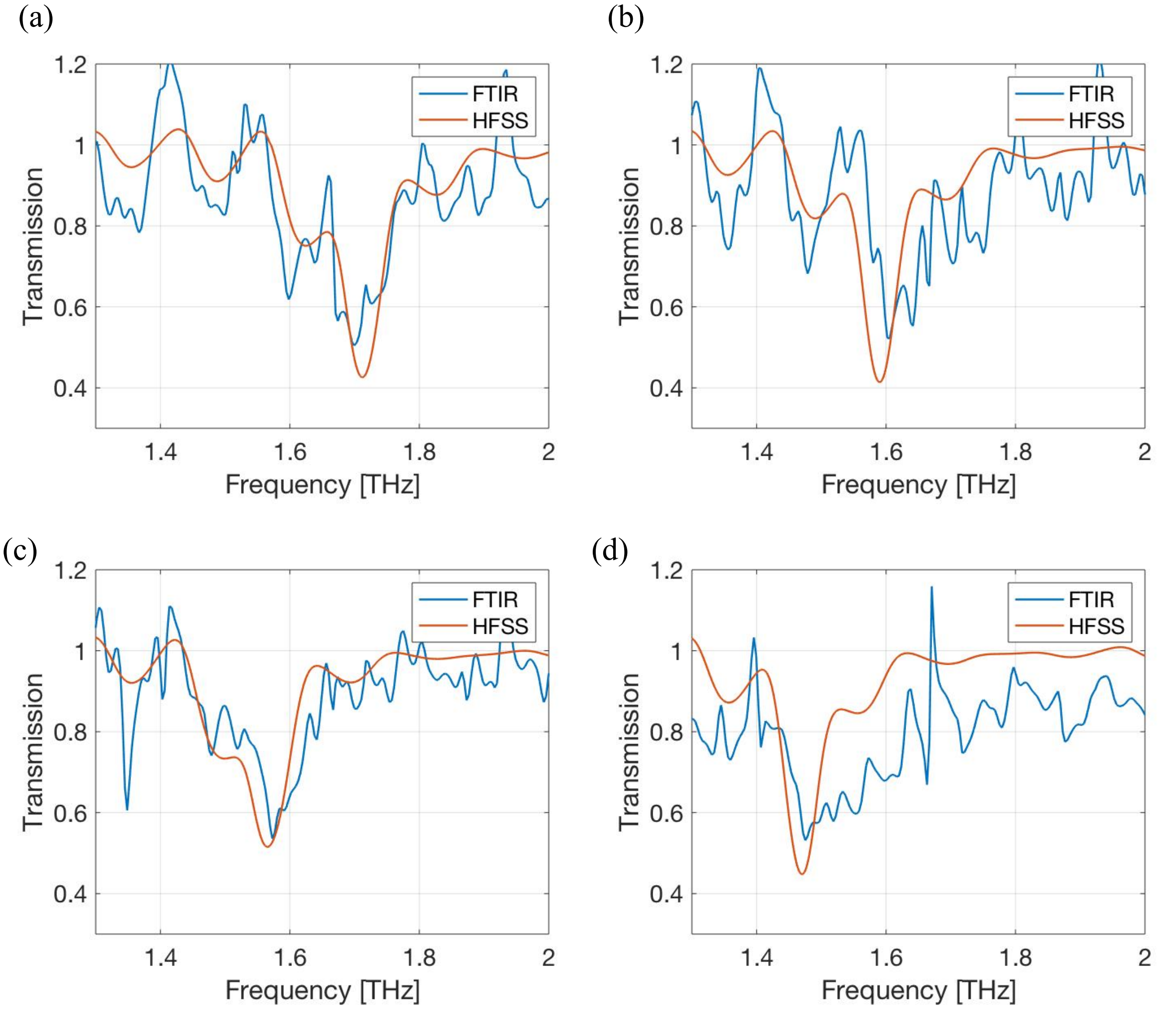

Figure 2.8 Transmission spectra of hybrid SRR/FeF_2 with SRR arm lengths changing from 25 μm to 28 μm ((a)~(d)). Blue lines are the experimental results measured by FTIR at room temperature, while orange lines are obtained from HFSS fitting, with determined permittivity of FeF_2 as $\epsilon_{FeF_2} = 5.2$.

FeF_2, the redshift of LC resonance frequency in the same sized SRR arrays indicates the effect coming from ultra-thin FeF_2 film simply due to the modified index of refraction of the thin film.

In order to study the dispersion relation of hybrid system, SRR arrays designed with different metallic arm lengths, *i.e.* $l_y = 25$ μm, 26 μm, 27 μm, 28 μm, are fabricated, leading to the frequency shift of LC resonant mode. The transmission spectra in Figure 2.8 exhibit resonance peaks at different frequencies ranging from 1.48 THz to 1.7 THz. Bare MgF_2 slab without any SRR pattern is used as a reference during transmission measurements, in order to get rid of the effects coming from multiple reflections within the thick substrate. Experimental results demonstrate frequency shift of LC resonant mode with respect to lithography tuning, and is fitted through HFSS simulation with the permittivity of FeF_2 set to be $\epsilon_{FeF_2} = 5.2$.

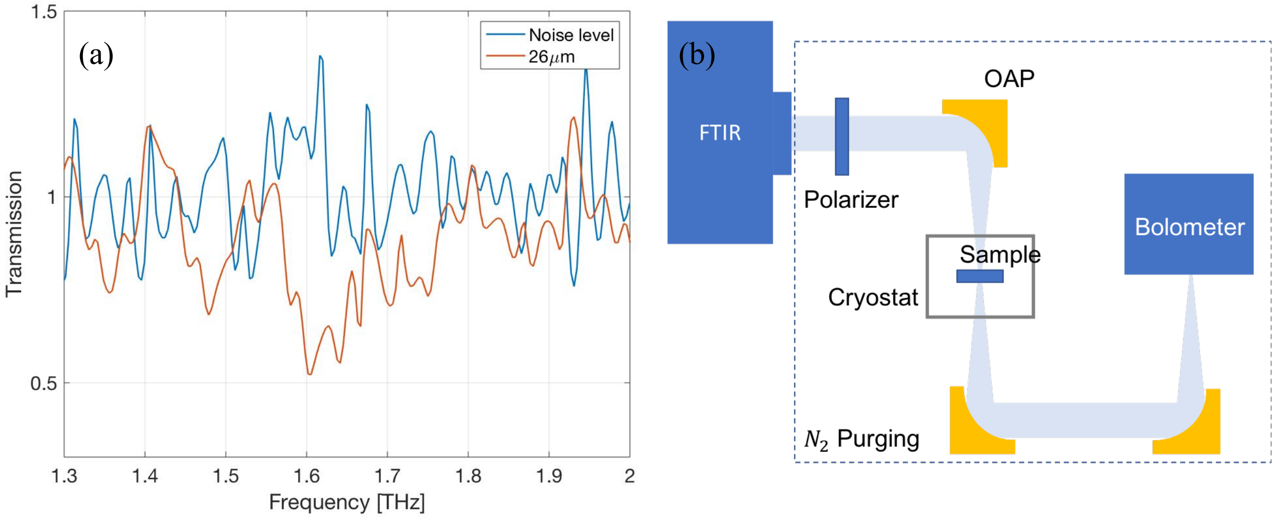

Figure 2.9 (a) Comparison between noise level (blue) and transmission spectrum of SRR with arm length of 26 μm (orange). (b) Experimental setup aims to focus the beam spot and increase the SNR.

However, there seems to be so many random fluctuations in the transmission spectra. And the relative strength of these fluctuations, *i.e.* noise level, is obtained by taking the ratio of the transmitted signals measured through two sequential scans. While a comparison between noise level and one of transmission spectra of SRR/FeF_2 sample is provided in Fig. 2.9 (a) which attributes these small fluctuations to high detection noise and therefore results in small SNR. The reason leading to this low SNR is multifold, while some possible causes can be 1) loss introduced by the polarizer; 2) the source used in FTIR instrument is the glo-bar, a resistively heated filament that emits black-body radiation, which only provides low power intensity within the frequency range of 1 ~ 2 THz; 3) the size of each SRR design is 5 mm by 5 mm which is smaller than the spot size of incident THz wave, so that most of the incident power is blocked. Further experimental plan includes building up an extra setup to focus the beam spot and increase SNR (Fig. 2.9 (b)), and put the sample into a cryostat cooled down to 4 K to study the properties of AF magnon and magnon-photon interaction in FeF_2.

Chapter 3: Design and simulation of inductor-capacitor (LC) circuit-based metal-metal waveguide

3.1 Introduction of LC circuit-based microcavity

In order to seek the possibility of intersubband transition based magnon-polariton laser, optical cavity modes supported by well-designed electromagnetic structures should maintain both high overlapping factor between its electric field component and the intersubband active region, as well as strong magnetic coupling to the antiferromagnetic materials. What's more, the effective cavity volume is expected to be as small as possible to enhance strong light-matter coupling.

The inductor-capacitor (LC) resonant circuit-based microcavity introduced by Wather *et al.* in 2010 becomes a promising approach [102]. It is similar to the commonly used THz metal-metal waveguide made of two high-conductivity metal plates with semiconductor layer sandwiched in between, where the use of metal enables smaller effective cavity volume and higher overlapping factor. What's different is that the top metal and semiconductor layer are further shaped into two half-circular–shaped capacitors connected by a narrow line acting as an inductor. The whole resonator can be viewed as an electronic lumped LC circuit, with resonance frequency determined by the dimension of its capacitive and inductive part (Figure 3.1). In this way, the effective cavity volume can be reduced almost at will, since the reduction in the capacitance can be compensated by an increase of the inductance, while the resonance frequency is kept constant. Moreover, LC circuit-based resonator enables spatial separation of the electric field and magnetic field components of optical mode. Electric field is highly confined uniformly between capacitor plates, while the magnetic field is mainly concentrated around the inductor, which enables an efficient overlapping with adjacent antiferromagnets.

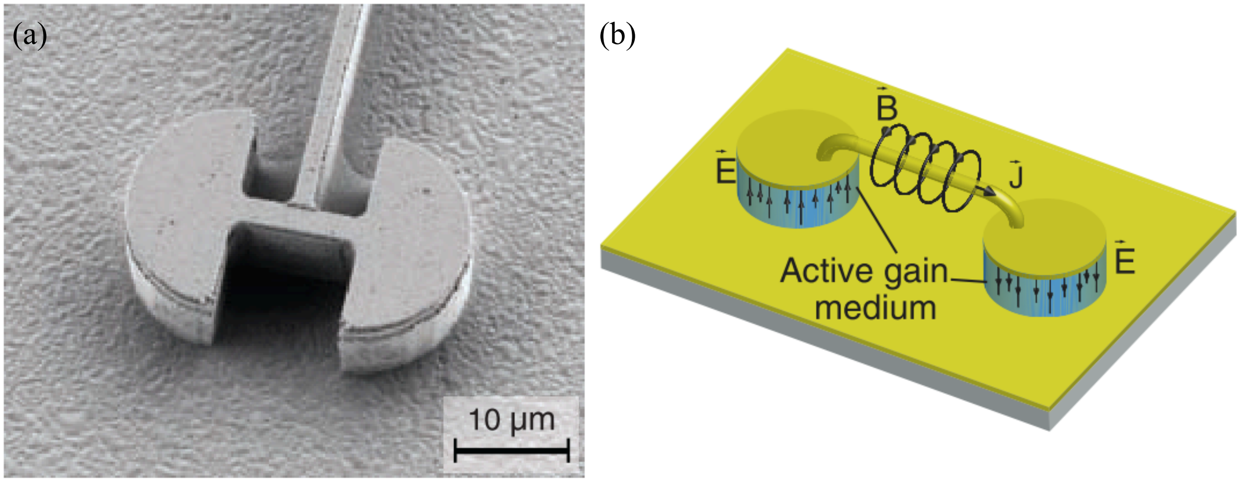

Figure 3.1 (a) Scanning electron micrograph picture of the LC circuit-based microcavity provided in Ref. [102] (b) Schematic of equivalent LC resonant circuit made of a wire connecting two capacitor plates put on a ground plane.

Highly subwavelength mode volume and strongly confined optical mode make LC circuit-based microcavity a good platform studying light-matter interaction and cavity QED in THz frequency range. Purcell effect [103], strong coupling [104] and ultrastrong coupling [105] between cavity photons and THz intersubband transition dipoles have been experimentally demonstrated, when the intersubband transitions carried by multiple quantum wells are inserted between the capacitor plates. Moreover, amplification of the electric field confined in the capacitors can be realized once the quantum wells are well designed into quantum cascade active region. With the external electrical pumping applied between the metallic capacitors which builds up the optical gain among the active region, a self-sustained LC cavity-based quantum cascade laser has been experimentally demonstrated in the presence of external magnetic field [102]. Other than traditional quantum cascade lasers which work in weak coupling regime, LC cavity-based polariton emitters have also been explored whose electroluminescence spectra with anticrossing between two polariton peaks have been observed experimentally even at room temperature [75]. These kinds of electroluminescent polaritonic devices working in the THz frequency range are considered to be promising proof-of-concept devices for more powerful THz sources.

As has been discussed above, the LC resonant mode of LC circuit-based microcavity is determined by the geometry of its capacitive and inductive components. Therefore, in order to tune the resonance frequency and study the hybrid dispersion of a strongly coupled light-matter system, multiple microcavities designed with different dimensions need to be fabricated which bring much more inconvenience. In contrast, the fact that metal-metal waveguides support a dispersive mode within the light cone provides the ability to tune the resonance frequency simply by changing the incidence angle during a reflectance measurement..

In this section, I propose the idea of combining metal-metal waveguide with the concept of LC circuit-based microcavity by etching holes along the ridge waveguides (as depicted in Fig. 3.2), and introduce a design of metasurface array with strong magnetic fringing field, enabling the generation of magnon-polaritons once an antiferromagnetic material is put in proximity to the metasurface. The properties of this LC circuit-based metal-metal waveguide (LC MM waveguide) will be first characterized using HFSS simulation, after which the antiferromagnetic FeF_2 film with magnon mode located around 1.6 THz is assumed on top of it and strongly couples with the induced surrounding magnetic field. The signatures of strong light-matter coupling, *i.e.* Rabi splitting between polariton states and hybrid dispersions, will be demonstrated using reflection spectroscopy. Furthermore, to realize a tripartite intersubband-magnon-photon coupling, the magnon-polariton system will be further coupled to another "matter" part - intersubband transition dipoles by inserting semiconductor quantum wells between metal plates of capacitors. Once semiconductor quantum wells are well-designed into quantum cascade gain medium, amplification and lasing of metasurface-confined magnon-polaritons become possible, and will be discussion into detail in the end of this section.

3.2 HFSS simulations and characterization

Numerical simulations are preformed based on a commercial finite element method solver (HFSS). The simulation unit cell is shown in Fig. 3.2 (a) with a length equals to the distance between periodic inductors along the ridge and width equals to period between ridges. Periodic boundary conditions are applied to the four sidewalls of simulation unit, so the unit cell repeats in two dimensions and forms a metasurface array as shown in Fig. 3.2 (b). The coordinate is chosen with z-axis perpendicular to the metasurface array and y-axis pointing along the MM waveguides. Electric field polarized along x-axis is incident from the top boundary.

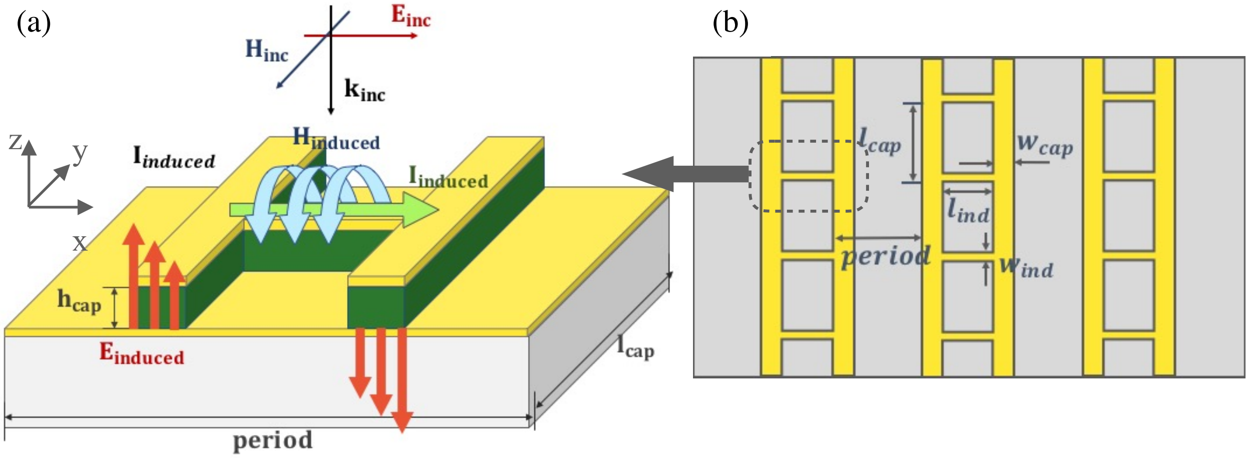

Figure 3.2 (a) Schematic view of LC circuit-based metal-metal waveguide unit cell. Arrows point out the direction of induced current (green), magnetic field (blue) and electric field (red) at resonance. (b) Bird's-eye illustration of the metasurface array consisting multiple LC MM waveguides, while the dashed box points out a single simulation unit as shown in (a).

Similar as the simulations on split ring resonators, both the patterned top metal and ground plane are modeled by 200 nm thick high conductivity gold whose electrical permittivity is described using Drude model with the doping concentration assumed to be 5.6×10^{22} cm^{-3} and relaxation time to be 39 fs. I first assume the semiconductor layer sandwiched between two metal plates to be purely GaAs, in which case no intersubband transitions within quantum wells are taken into consideration yet. The free electron absorption in GaAs is also modeled by Drude model, with doping concentration of 5×10^{15} cm^{-3} and relaxation time of 0.5 ps. Its relative permittivity is $\epsilon_{GaAs} = 12.9$ at THz frequency range.

Design parameters are labelled in Figure 3.2 describing the geometry of LC circuit-based metal-metal waveguide, which includes the length and width of the inductive metal strip: l_{ind}, w_{ind}; the length of capacitor plates, or equivalently, the distance between metal strips along the waveguide: l_{cap}; the width of capacitor plates: w_{cap}; the thickness of semiconductor layer sandwiched between metal plates: h_{cap}, and the period of LC MM waveguides spaced along x direction. All these parameters work together contributing to the resonance frequency and quality factor of cavity-enhanced LC resonant mode, which can be exploited through reflectance spectroscopy. And in order to realize the strong coupling between cavity photons confined in LC MM waveguides and AF magnons carried by antiferromagnetic FeF_2 film, the design parameters have to be carefully chosen so that the LC resonance frequency is located around AF magnon frequency at 1.6 THz, and the quality factor is large enough for the system entering strong light-matter coupling regime.

To characterize the effect of each design parameter to the overall quality factor, first, I fix the dimension of inductive metal strip to be l_{ind} = 15 μm, w_{ind} = 1 μm, as well as the width of capacitor plates: w_{cap} = 6 μm, and increase the distance between two capacitor plates h_{cap} from 1 μm to 10 μm, at the same time reducing the length of capacitor plates correspondingly to fix the resonance frequency. The reflectance spectra are plotted in Fig. 3.3 (a) indicating that, as the values of h_{cap} are set to be 1 μm, 3 μm, 5 μm, 8 μm, 10 μm, the full width half maximum (FHWM) of reflectivity dips are 128 GHz, 124 GHz, 148 GHz, 194 GHz and 230 GHz respectively.

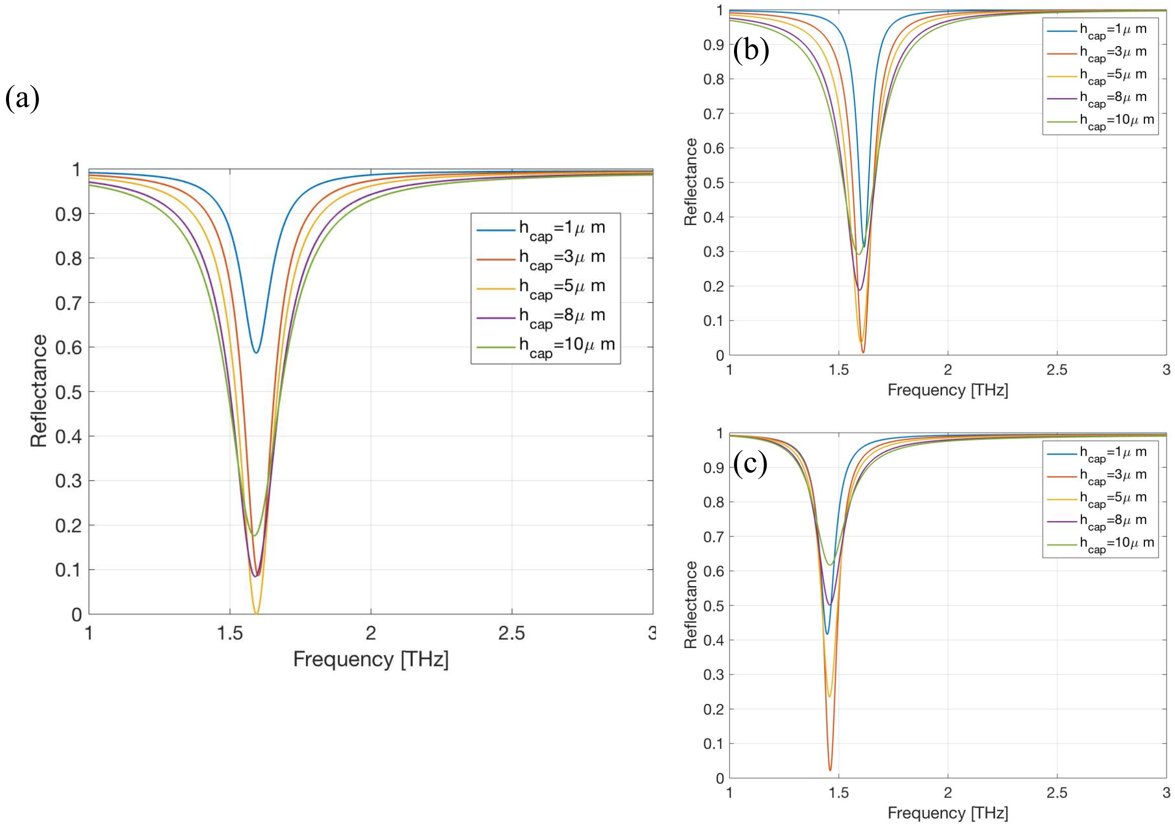

Figure 3.3 Reflectance spectra as the distance between capacitor plates are changed while the resonance frequency is fixed at 1.6 THz by changing the value of l_{cap} in the case when (a) both metal plates and GaAs layer are modeled using Drude model; (b) metal plates are modeled as PEC; (c) GaAs layer is assumed to be undoped with constant permittivity.

In order to analyze how the design parameters determine the quality factor of LC resonant mode, all the damping rates contributing to the overall quality factor are taken into consideration and analyzed separately, which includes both radiative damping γ_r and non-radiative damping γ_{nr} consisting of metallic loss and free carrier absorption in doped semiconductor $\gamma_{nr} = \gamma_m + \gamma_{sc}$. In the reflectance spectra shown in Fig. 3.3 (a), both high conductivity gold plates and doped GaAs layer are described using Drude model, while the damping rates obtained from FHWM are therefore a summation of radiative and non-radiative losses: $\gamma_{tot} = \gamma_m + \gamma_{sc} + \gamma_{rad}$.

h_{cap}	γ_{tot}	γ_m	γ_{sc}	γ_r
1 μm	128 GHz	59 GHz	44 GHz	25 GHz
3 μm	124 GHz	27 GHz	48 GHz	49 GHz
5 μm	148 GHz	21 GHz	50 GHz	77 GHz
8 μm	194 GHz	15 GHz	51 GHz	128 GHz
10 μm	230 GHz	13 GHz	52 GHz	165 GHz

Table 3.1 Different damping rates in LC MM waveguide designed with varies distances between capacitor plates.

If now, the metal plates are modeled as perfect electrical conductor (PEC) or the GaAs layer is replaced by undoped GaAs, the term of metallic loss or free carrier absorption in GaAs will be removed from total damping rate. Such simulations are done with exactly the same geometry, whose bandwidths shown in the reflectance spectra provide the values of $\gamma_{sc} + \gamma_{rad}$ (Fig. 3.3 (b)) and $\gamma_m + \gamma_{rad}$ (Fig. 3.3 (c)) respectively. Comparing damping rates shown in these sets of simulations, the values of radiative damping rate γ_r, metallic loss γ_m, absorption loss γ_{sc} at each distance between two capacitor plates are obtained and summarized in Table 3.1 and Fig. 3.5 (a). Moreover, the radiative loss can also be obtained through the phase shift of reflection coefficient in the simulation excluding all the non-radiative losses, *i.e.* using both PEC and undoped GaAs layer. After an analytical fitting of the simulated phase shift (Figure 3.4), the radiative damping rates are very close to the values shown in Table 3.1, demonstrating the reliability of data.

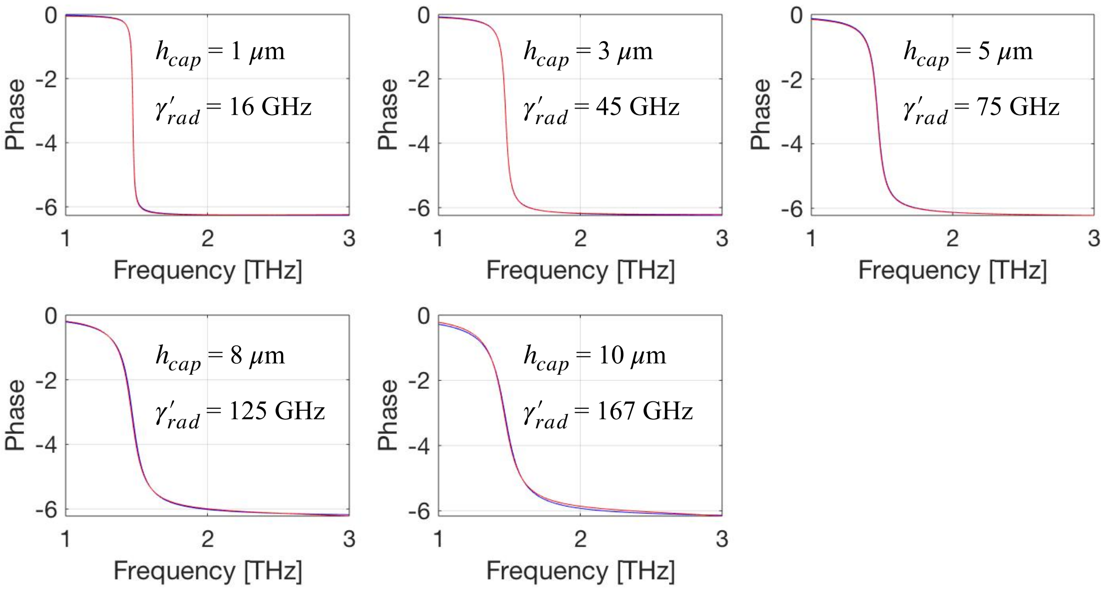

Figure 3.4 Reflection phase shifts in the case when metal plates are modeled as PEC and GaAs layer is assumed to be undoped with constant permittivity in the HFSS simulation (red lines). Blue lines are the analytical fittings with the obtained radiative damping rates labeled in the graphs.

It's now clear that as the distance between two capacitor plates increases, free carrier absorption in doped GaAs layer only slightly increases while the radiative loss increases rapidly as thicker semiconductor layer increases the radiation scattering regions, which explains the decreasing quality factor in thicker LC MM waveguides, except at h_{cap} = 1 μm, where the extremely high metallic loss leads to overall low quality factor. The metallic loss decreases with h_{cap} because in a thinner MM waveguide, where the optical field confinement factor is lower, the long wavelength radiation is forced into the lossy metallic regions resulting in larger penetration length and therefore higher metallic loss.

Another feature obtained from the spectra in Fig. 3.3 (a) is that the reflectance at resonance frequency decreases with the increase of h_{cap} before it reaches 5 μm, while as h_{cap} keeps increasing, the reflectance at resonance frequency increases. This phenomenon can be understand as a situation called critical coupling. As discussed in Ref. [106, 107], structures like the LC MM waveguide metasurface can be described as one port systems whose electromagnetic coupling to the free space is described by its radiative damping rate γ_r, while the losses coming from the system is characterized by the non-radiative rate γ_{nr}. Critical coupling is realized when the two damping rates are matched, *i.e.* $\gamma_r = \gamma_{nr}$, in which case all the incoming photons are coupled and confined into the resonant cavity mode with the reflectance at resonance frequency equals to zero. In our simulations, as the distance between two capacitor plates is increased, the radiation decay rate is increased dramatically and compared with the relative value of non-radiative decay rate which also changes correspondingly, the system transits from the under-coupling regime ($\gamma_r < \gamma_{nr}$) to the over-coupling regime ($\gamma_r > \gamma_{nr}$). While at a thickness around 5 μm, the critical coupling condition has been realized, as shown by the intersection between radiative and non-radiative damping rates in Fig. 3.5 (b).

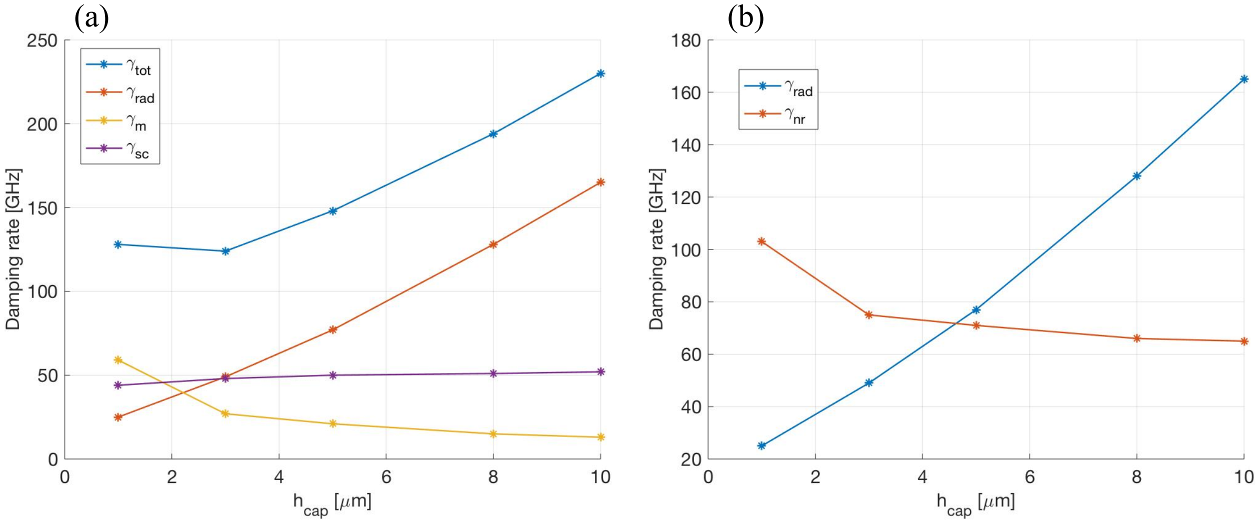

Figure 3.5 (a) Different damping rates at different h_{cap}; (b) Radiative and non-radiative damping rates plotted at different h_{cap}.

After fully analyzing how the distance between two capacitor plates influences various damping rates, the effects of width and length of the capacitor plates w_{cap}, l_{cap} are studied by changing l_{cap} from 5 μm to 20 μm while decreasing w_{cap} corresponding with other design parameters fixed *i.e.* l_{ind} = 15 μm, w_{ind} = 1 μm, h_{cap} = 3 μm. The simulation results are plotted in Fig. 3.6 (a) which demonstrate that capacitor plates designed with longer length but shorter width are expected to provide a higher quality factor, as well as larger reflectance minimum. That is different from a traditional parallel plate capacitor whose capacitance is only related to the area, but not the shape of capacitor plates. Different kinds of damping rates are obtained in the same way discussed above whose values are summarized in Table 3.2. And by plotting the capacitor length dependence of each damping rate (Fig. 3.6 (b)), the possible reason of increasing quality factor with respect to l_{cap} can be attributed to lower radiative damping rate.

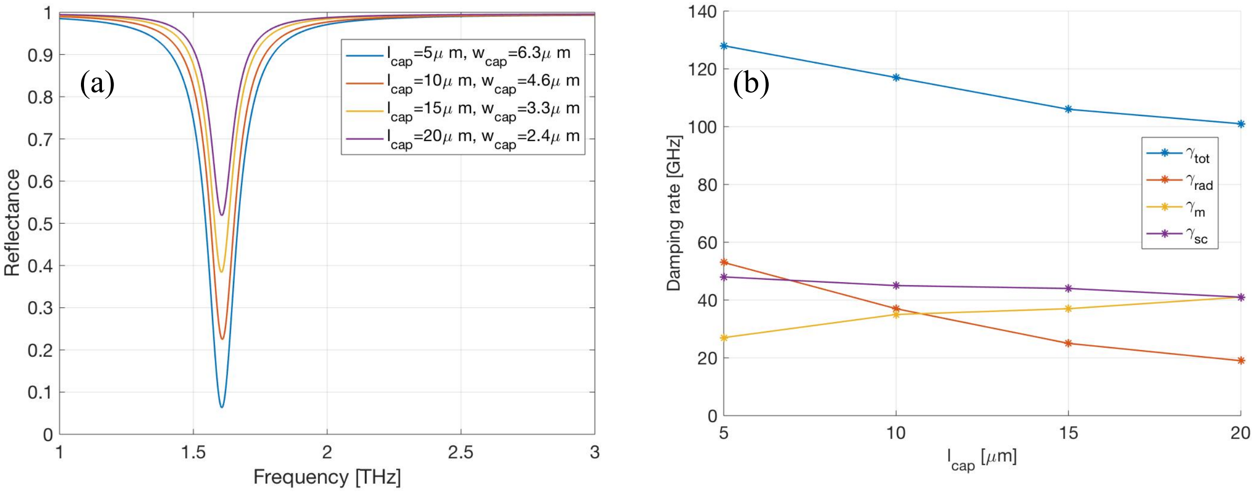

Figure 3.6. (a) Reflectance spectra as the shape of capacitor plates are changed in the case when both metal plates and GaAs layer are modeled in Drude model; (b) Different damping rates with respect to l_{cap}.

l_{cap}	γ_{tot}	γ_m	γ_{sc}	γ_r
5 μm	128 GHz	48 GHz	27 GHz	53 GHz
10 μm	117 GHz	45 GHz	35 GHz	37 GHz
15 μm	106 GHz	44 GHz	37 GHz	25 GHz
20 μm	101 GHz	41 GHz	41 GHz	19 GHz

Table 3.2 Different damping rates in LC MM waveguide designed with varies length of capacitor plates.

What's more, the relative values of inductance and capacitance of a LC circuit-based structure will also affect the quality factor. The overall geometry of LC MM waveguide is in analogy to an electronic lumped LC resonant circuit, where the inductor is implemented as a wire connecting two capacitor plates which are situated above a ground plane. The electric fields excited within two capacitors have opposite directions which lead to zero potential in the middle of the inductive metal strip, and build up a parallel LC resonant circuit together with the ground plane. The circuit representation is shown in Fig. 3.7 (a). In a parallel LC resonant circuit, the quality factor of resonant mode is proportional to $\sqrt{\frac{C}{L}}$, and to demonstrate this relationship in the LC MM waveguide, two geometries designed with different relative values of inductance and capacitance are simulated with fixed resonance frequency, *i.e.* the products of inductance and capacitance are the same. The reflectance spectra are plotted in Fig. 3.7 (b) with design parameters provided in the caption. The geometry designed with relatively larger inductance has a FWHM of 125 GHz, while the one with larger capacitance has a FWHM of 94 GHz, following the expression of quality factor in a parallel LC resonant circuit. And the reason can be explained as, with the metal strip designed to be longer but narrower, its inductance is higher but the metallic loss

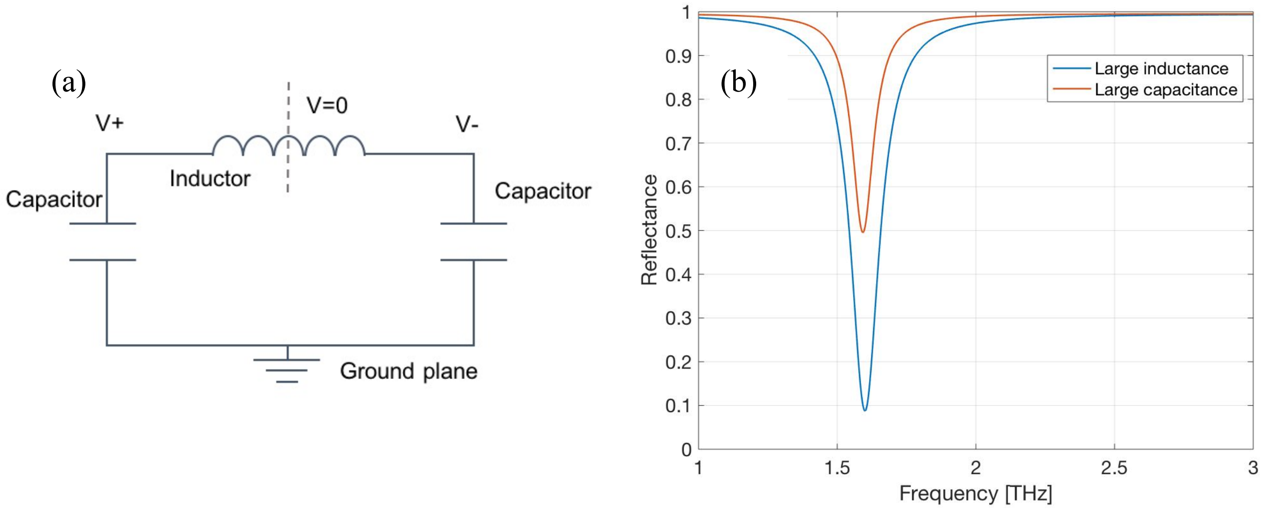

Figure 3.7 (a) Circuit representation of the LC circuit-based MM waveguide. (b) Reflectance spectra of two geometries, one has relatively larger inductance with l_{ind} = 15 μm, w_{ind} = 1 μm, l_{cap} = 6 μm, another one has relatively larger capacitance with l_{ind} = 6 μm, w_{ind} = 3 μm, l_{cap} = 24 μm. The other parameters are set to be the same.

coming from the inductor, which is proportional to $\frac{l_{ind}}{w_{ind}}$, is also increased, leading to lower quality factor of LC resonant mode.

As many other metastructures, the period between MM waveguides will also affect the quality factor. Period defines the Bragg diffraction modes, in which case radiation coming from periodic units interfere with each other constructively, and at the frequency $\nu = \frac{c}{\Lambda}$, where Λ represents the period, the diffracted light is confined and travels among the metasurface plane, which reduces the radiative loss in the perpendicular direction and therefore increases the quality factor. If the optical cavity mode supported in LC MM waveguide is in resonance with surface Bragg mode when the period is set to be $\Lambda = \lambda_{cav}$, hybridization between these two modes is realized and higher quality factor LC mode is achieved. However, the propagating surface wave in a finite metasurface will also lead to diffraction loss through the edges. As the cavity resonant mode becomes closer to the surface Bragg mode, the degree of hybridization will increase the diffraction loss, which indicates that the metasurface period should be kept less than ≈ 80% of the resonance wavelength. If light is not radiating into free space, as I will discuss later, in the case when an antiferromagnetic layer is put on top of the metasurface, the ideal period in this case should be modified by the effective wavelength in the dielectric, *i.e.* $\Lambda \approx 80\% \times \lambda_{cav} n_d$ and is chosen to be 60 μm with $n_{MgF_2} \approx 2.2$ in all the above simulations.

3.3 Strong coupling with AF magnons in thin FeF_2 film

Considering all the design parameters contributing to the quality factor of LC resonant mode in LC circuit-based MM waveguide, the inductive metal strip is designed with a length of 6 μm and a width of 3 μm to keep the inductance relatively small. The distance between capacitor plates is chosen to be 3 μm, considering both metallic loss and radiative loss. The width and length of the capacitors are set to be 4 μm and 28 μm respectively, so the quality factor is large enough for the system entering strong light-matter coupling regime, while the signal strength, *i.e.* minimum reflectance at resonance frequency is also strong, which ensures a large signal-to-noise ratio during further experimental measurements. Generally, once the quality factor of electromagnetic structure enables the strong coupling between cavity photons and material excitations, light-matter coupling strength is determined by the volume density of material excitations and overlapping factor, and will only slightly affected by the damping rates. Therefore, the quality factor of LC circuit-based metal-metal waveguide is not designed to be as high as possible, in order to reach relatively stronger reflection signal and easier fabrication process.

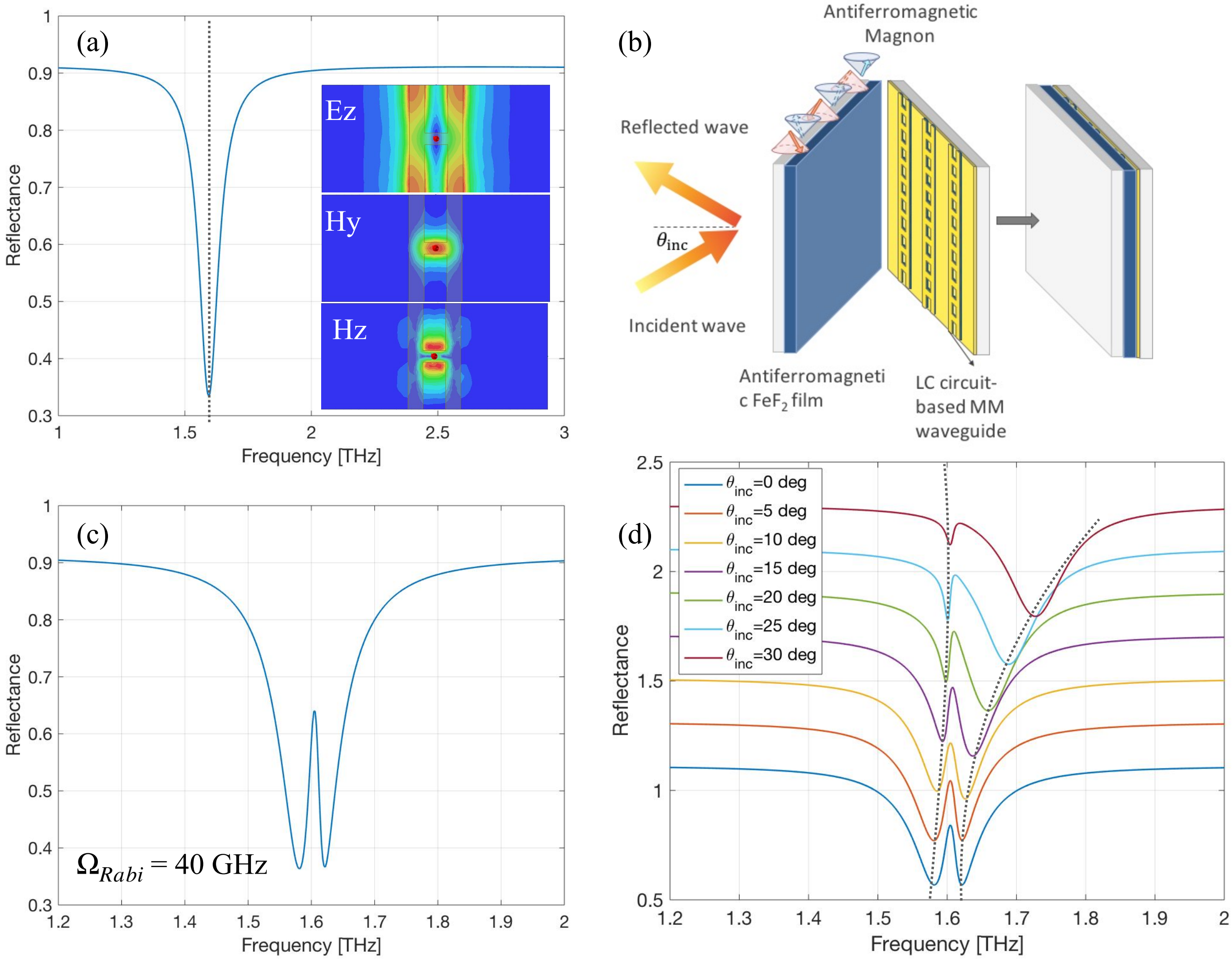

Figure 3.8 (a) Reflectance spectrum of bare LC resonant mode. Inset shows the electric and magnetic field distributions on the plane crosscutting the LC MM waveguide. (b) Schematic view of the LC circuit-based MM waveguides and an antiferromagnetic FeF$_2$ film grown on MgF$_2$ substrate, which are put together indicated by the grey arrow. (c) Reflectance spectrum of hybrid metasurface/antiferromagnet system. (d) Reflectance spectra at different incidence angles show the hybrid dispersion relations of magnon-polaritons.

Fig. 3.8 (a) shows the reflectance spectrum of such a LC MM waveguide with LC resonant mode. MgF$_2$ substrate with optical properties of $\epsilon_{MgF_2} = 4.71$, $\alpha_{MgF_2} = 6$ cm^{-1} is applied in replacement of the air box, simulating light incident from the thick substrate into the metasurface instead of free space. The LC resonant mode in existence of MgF$_2$ substrate is design with a frequency of 1.6 THz, around the resonance frequency of AF magnons in FeF$_2$, while its quality factor is lower due to absorption in MgF_2 with a total damping rate increases from 84 GHz with free space radiation to 96 GHz. The inset plots the z-component electric field as well as y- and z-component magnetic field distributions on the plane crosscutting the LC MM waveguide, which demonstrates the spatial separation of electric and magnetic fields within the capacitive and inductive components of LC MM waveguide respectively.

In order to realize strong light-matter coupling, antiferromagnetic FeF_2 film grown on MgF_2 substrate is put in proximity to the metasurface and strongly couples with the induced surrounding magnetic field. This hybrid system is sketched in Fig. 3.8 (b). Similar as the simulations of split ring resonators, a Lorentzian-shaped magnetic excitation is used to characterize the optical properties of FeF_2 film used in HFSS simulations, while its frequency-independent permittivity is $\epsilon_{FeF_2} = 5.2$. The easy axis of FeF_2 is set aligned with the x-axis of the coordinate system considering the direction of circulating magnetic field around the inductive metal strip. The reflectance spectra are plotted in Fig. 3.8 (c), with a Rabi splitting around 40 GHz, demonstrating the system entering strong light-matter coupling system. As the incident light is tilted resulting in in-plane wave vector along the MM waveguide, the frequency of cavity resonant mode is shifted with respect to AF magnon mode fixed at 1.6 THz, revealing the hybrid dispersion relation of magnon-polaritons as shown in Fig. 3.8 (d).

3.4 Intersubband-magnon-polariton

Electromagnetic resonators made of metal-dielectric-metal structures have been considered as ideal systems to study the generation of cavity intersubband-polaritons in mid-infrared or terahertz frequency range, benefited by their convenience of combination with quantum well intersubband transitions and highly confined optical cavity modes between metallic plates. Strong and even ultrastrong coupling between intersubband transition dipoles and cavity photons have been demonstrated both in traditional metal-dielectric-metal microcavities [26, 81] and LC circuit-based microcavities [104, 105] with a theoretical coupling strength in terms of Rabi frequency given as [81]:

$$2\Omega_r = \sqrt{f_w}\omega_P,\ \omega_P^2 = \frac{e^2}{\epsilon_0 n_r^2 m^*}\frac{f_{12}\left(N_1 - N_2\right)}{L_{QW}}, \tag{3.1}$$

where ω_P is termed as plasma frequency and f_w is the overlapping factor between optical cavity mode and intersubband dipoles. n_r is the refractive index of semiconductor layer, m^* is the effective electron mass, f_{12} is the oscillator strength of intersubband transitions, $N_{1,2}$ are the electron populations of the initial and final subbands during the intersubband transitions and L_{QW} is the thickness of quantum well and barrier in one module.

Multiple quantum wells with intersubband absorption can be modeled through a Drude-Lorentz dielectric tensor. Electrons move freely among the plane perpendicular to the growth direction and are describe by Drude model:

$$\epsilon_{xx} = \epsilon_{yy} = \epsilon_{core} - \frac{n_s e^2}{\epsilon_0 m^* L_{QW}\left(\omega^2 + i\frac{\omega}{\tau_m}\right)}, \tag{3.2}$$

while the intersubband transitions occurring only along the growth direction due to selection rule are described by a Lorentzian oscillator similar as any other material excitations, in the form of:

$$\epsilon_{zz} = \epsilon_{core} - \frac{n_s e^2 f_{12}}{\epsilon_0 m^* L_{QW}\left(\omega^2 - \omega_{12}^2 + i\frac{\omega}{\tau}\right)}. \tag{3.3}$$

It is a phenomenological model bridging the relationship between intersubband and free carrier absorption, while in the limit of $\omega_{12} = 0$, a Drude-like expression for the permittivity is recovered. τ is a phenomenological relaxation time of intersubband transitions chosen to agree with the momentum relaxation time τ_m of free electrons in Drude model, and is assumed to be $\tau = \tau_m = 0.5$ ps in the simulations, *i.e.* the corresponding FWHM of the intersubband transition is around 640 GHz.

In the HFSS simulation, each quantum well with intersubband transition is assumed with an oscillator strength of $f_{12} = 0.96$ and thickness of $L_{QW} = 50$ nm. The overlapping between intersubband dipoles carried by quantum wells and optical mode confined in the metal-metal waveguide which is designed to be 3 μm thick is characterized by the overlapping factor f_w. The intersubband transition ω_{12} is targeted at the frequency of 2 THz, so the lower branch of generated

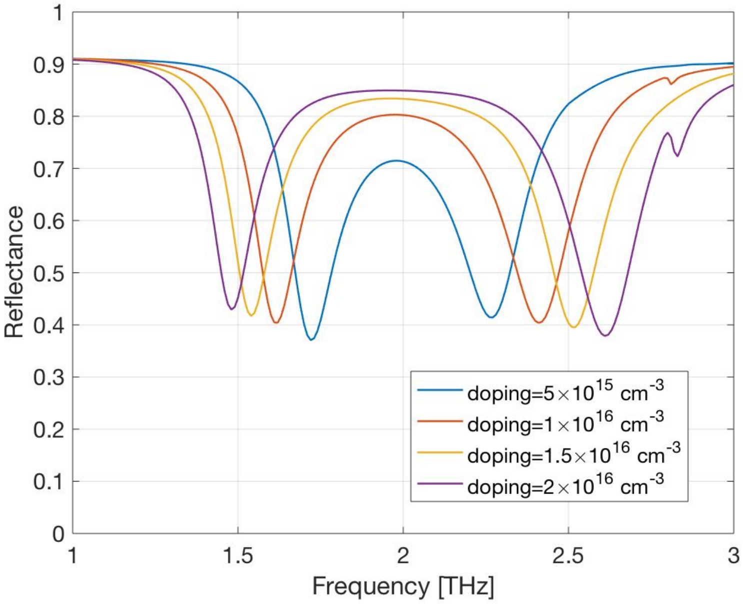

Figure 3.9 Reflectance spectra of LC MM waveguide with multiple quantum wells sandwiched between metallic capacitors at different doping levels. While the frequency splitting demonstrates the strong coupling between intersubband transition dipoles and cavity photons.

intersubband-polaritons is located around 1.6 THz, in resonance with the AF magnons in FeF$_2$. And the length of capacitor plates in the LC MM waveguide design is reduced to 18 μm in order to obtain an optical cavity mode in resonance with intersubband transitions at 2 THz. According to equation (3.1), coupling strength is proportional to the square root of volume density of population difference between subbands, *i.e.* $\frac{N_1 - N_2}{L_{QW}}$. As the sheet density used in the HFSS simulation increases from $N_1 - N_2 = 2.5 \times 10^{10}$ cm^{-2}, 5×10^{10} cm^{-2}, 7.5×10^{10} cm^{-2} to 1×10^{11} cm^{-2} , the frequency splitting between polariton states shown in the reflectance spectra in Fig. 3.9 increases from 0.55 THz, 0.79 THz, 0.98 THz to 1.13 THz, generally follows the square root relationship. And compared with the analytical values calculated from equation (3.1), the overlapping factor is obtained around $f_w \approx 0.7$.

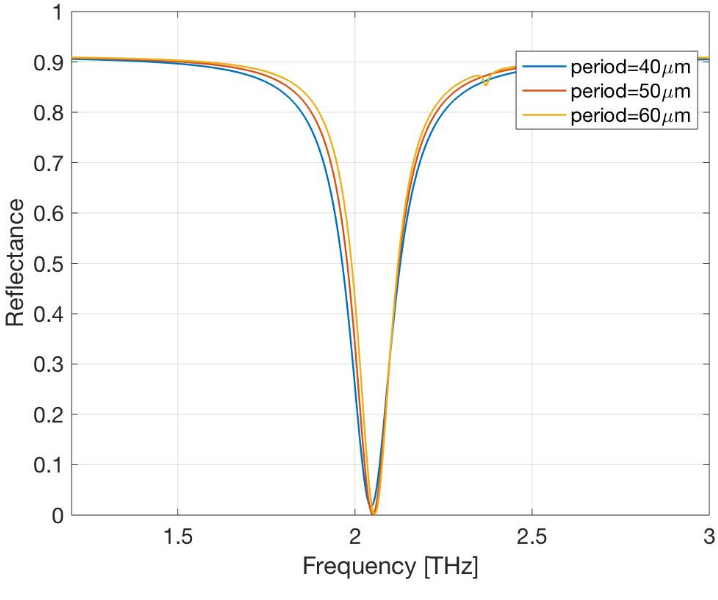

Figure 3.10 Reflectance spectra of LC resonant mode with various period in the case when bulk GaAs layer with Drude loss is inserted between capacitor plates.

With a doping concentration of 5×10^{10} cm^{-2}, the polariton states are located at frequencies of $\omega_{\pm} = \omega_{12} \pm \Omega_r$ with the lower polariton branch around 1.6 THz and the upper polariton branch around 2.41 THz at which frequency Bragg diffraction modes will be excited with a period of 60 μm. In order to avoid the hybridization between Bragg modes and higher polariton branch, the period between waveguides is deliberately made smaller with a value of 50 μm and the Bragg diffraction now starts from 2.78 THz. However, the quality factor of LC resonant mode is also decreased with smaller period. As simulated in Figure 3.10 in the case when quantum well heterostructure is replaced by bulk GaAs layer with Drude loss, as the period is set to be 60 μm, 50μm, 40 μm, the linewidth of LC resonant mode is 118 GHz, 131 GHz and 149 GHz respectively. As will be shown later, this reduced quality factor still enables the system reaching strong light-matter coupling regime.

Other than period and length of the capacitor plates, the rest of the design parameters used in the geometry of the LC MM waveguide are the same as discussed in the previous sections. And other materials used in the HFSS simulations, *i.e.* high conductivity metal layers, antiferromagnetic FeF_2 film with its lossy MgF_2 substrate, are still modeled using the same optical properties.

The optical cavity mode of LC MM waveguide with modified design parameters and bulk GaAs layer sandwiched between capacitor plates is simulated, whose reflectance spectrum is plotted in Fig. 3.11 (a), with LC resonance frequency around the intersubband transition frequency at 2 THz. Once the bulk GaAs is replaced by intersubband transition based quantum wells, the Rabi splitting between intersubband-polariton states shown in Fig. 3.11 (b) demonstrates the strong coupling between intersubband transition dipoles and cavity photons confined in LC MM waveguides.

Then, antiferromagnetic FeF_2 film is put in proximity on the metasurface, with Lorentzian-shaped magnetic excitations in resonance with the lower-branch intersubband-polaritons, and the lower intersubband-polariton state is further splitted into two with frequency splitting of 36 GHz, which reveals the strong coupling between intersubband-polaritons and AF magnons, leading to the generation of tripartite intersubband-magnon-polaritons. As the optical cavity mode is shifted by changing the dimension of LC MM waveguide, dispersion of hybrid intersubband-magnon-polaritons is shown in Fig. 3.11 (d).

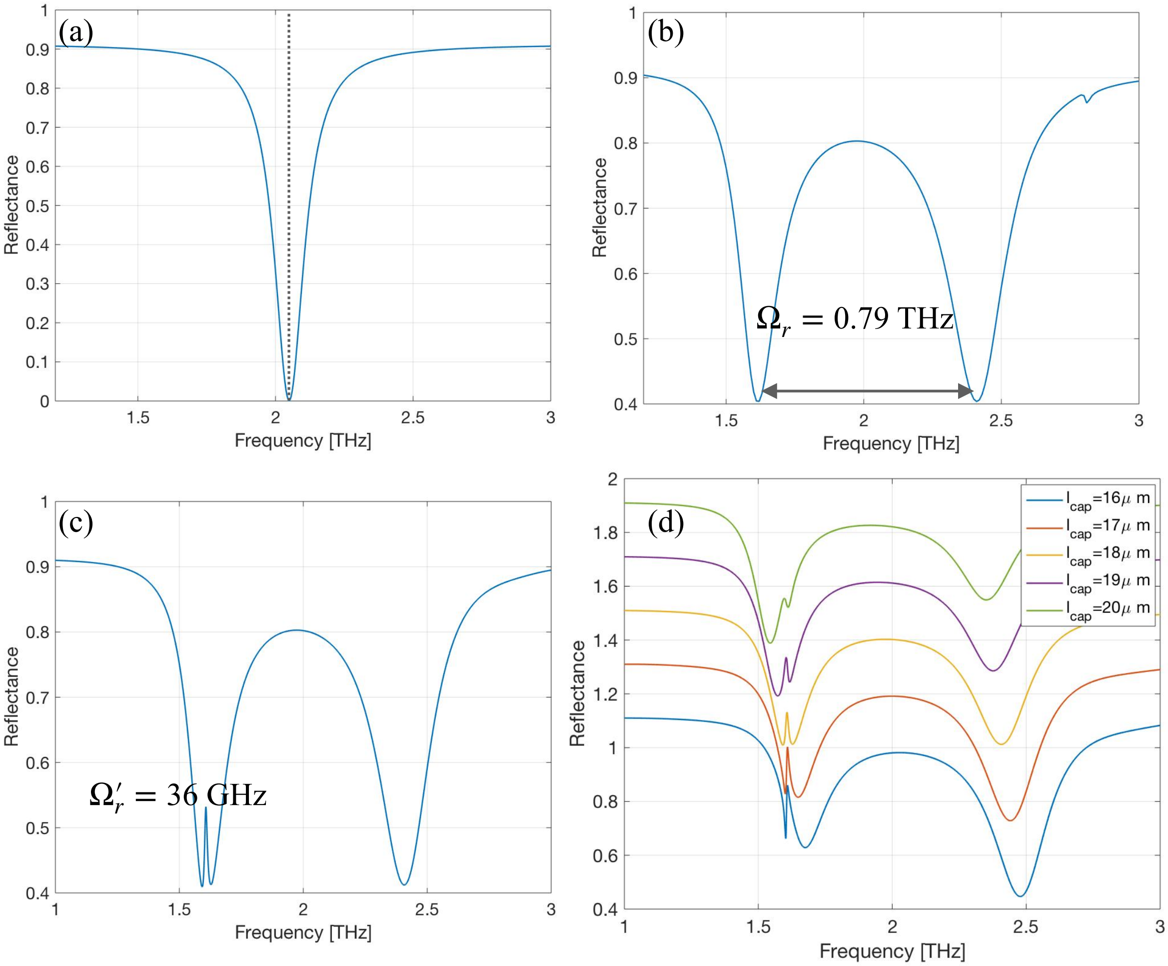

Figure 3.11 (a) LC resonant mode of LC MM waveguide with bulk GaAs layer. (b) Once the bulk GaAs layer is replaced by multiple quantum wells with intersubband transitions, Rabi splitting shown in reflectance spectrum demonstrates the generation of intersubband-polaritons. (c) The lower intersubband-polariton branch located at 1.6 THz further strongly couples with AF magnons in FeF_2. (d) Dispersion of hybrid system.

3.5 Approach to magnon-polariton quantum cascade laser

To seek the possibility of magnon-polariton quantum cascade laser, semiconductor layer sandwiched between capacitor plates is well-designed into quantum cascade active region. Once the external electrical pumping is applied between top and bottom metallic plates, population inversion is built up among electronic states and electron injection and extraction are realized across cascaded quantum wells, leading to intersubband transition based optical gain which makes amplification or even lasing of metasurface-confined magnon-polaritons possible.

The permittivity of quantum cascade active region is also described by Drude-Lorentzian model, with free electron absorption within epitaxial layers and intersubband absorption along the growth direction. The intersubband absorption in this case is attributed to transitions between the ground state $|1\rangle$ and the higher energy states $|2\rangle$, $|3\rangle$ and $|4\rangle$, since most of the doped electrons are assumed to reside on the ground state within the injection well.

The quantum cascade active region considered for the approach to magnon-polariton quantum cascade laser consists of four quantum wells with resonant LO-phonon depopulation mechanism. The layer thicknesses are **50.9**/ 108.8/ **19.8**/ 103.1/ **36.7**/ 87.6/ **39.6**/ 177.4 A starting with the injector barrier, where the $Al_{0.15}Ga_{0.85}As$ barriers are indicated in bold font. Band structure of the investigated design is plotted in Fig. 3.12 (a) simulated using shooting method under an applied bias of 45.2 mV per module, at which the injection state $|1'\rangle$ aligns with the upper lasing state $|5\rangle$. Optical transition between levels $|5\rangle$ and $|4\rangle$ gives out the radiation at around 2 THz, whereas the intersubband absorption is contributed by transition from level $|1\rangle$ to $|2\rangle$ with energy difference nearly in resonance with the LO-phonons of GaAs, *i.e.* E_{21} = 29.73 meV, and the calculated oscillator strength of f_{21} = 0.31, as well as level $|1\rangle$ to $|3\rangle$ with E_{31} = 33.77 meV, f_{31} = 0.25 and level $|1\rangle$ to $|4\rangle$ with E_{41} = 36.78 meV, f_{41} = 0.42. The sheet doping concentration is assumed to be $n_s = 4.4 \times 10^{10}$ cm^{-2}, and considering the thickness of one module which is 62.3 nm, the averaged bulk electron concentration is 7.1×10^{15} cm^{-3}. Substituting all these parameters into the Drude-Lorentzian permittivity tensor provided by equation (3.2) and (3.3), the absorption losses in this kind of quantum cascade active region are characterized. While optical gain provided by the electrically pumped active region is represented by a simplified frequency independent gain coefficient, considering usually broadband intersubband transitions.

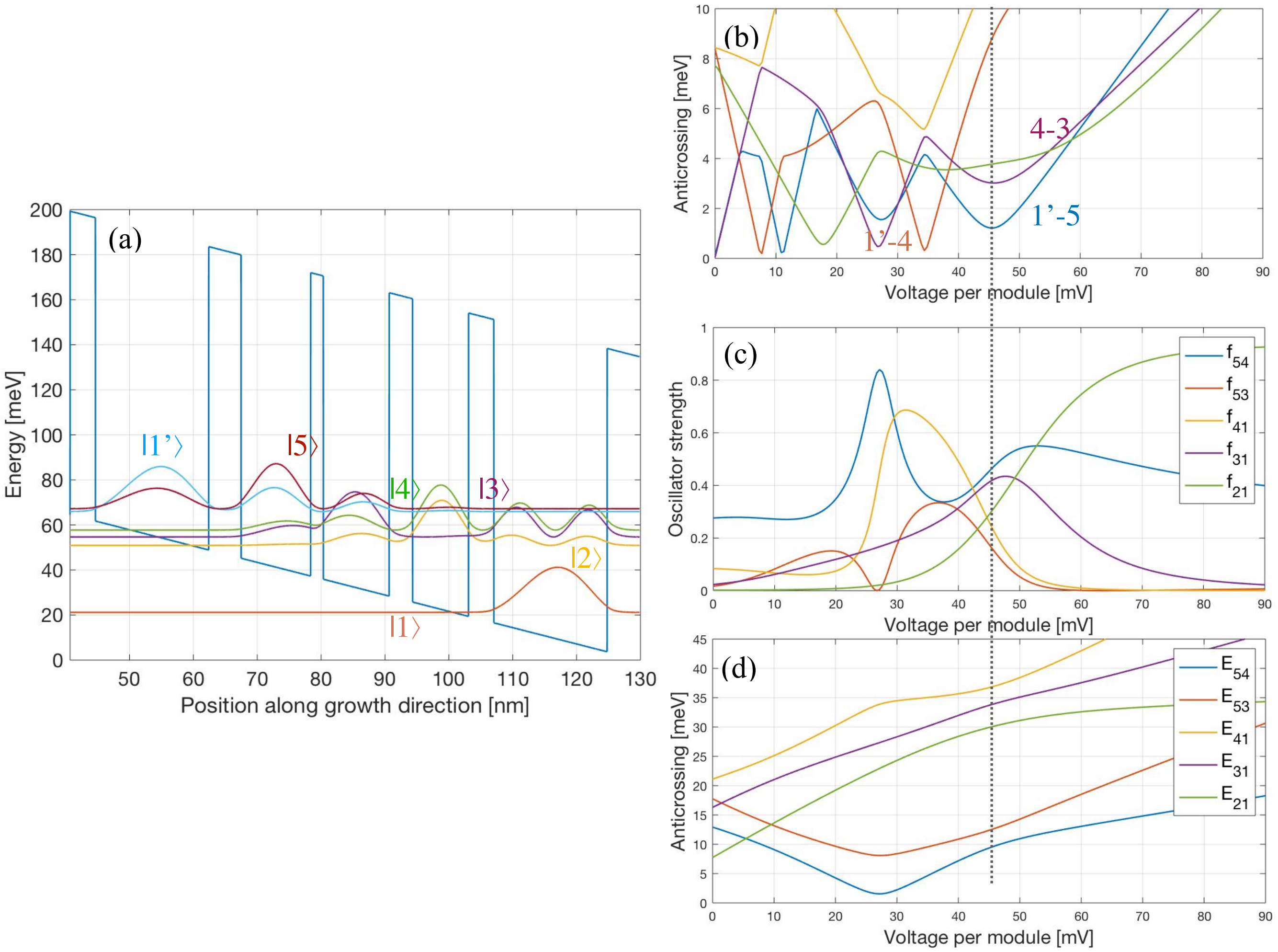

Figure 3.12 (a) Band structure of four-quantum-well resonant LO-phonon design quantum cascade active region. Each of the electronic states is labeled. (b) The anticrossings between subbands at different biases. While the energy separation between injection state |1'⟩ and upper lasing state |5⟩ reaches its minimum at a bias of 45.2 mV/mod and is indicated by the dotted line . (c) Oscillator strength and (d) energy difference of each intersubband transition with respect to applied bias using one module simulation.

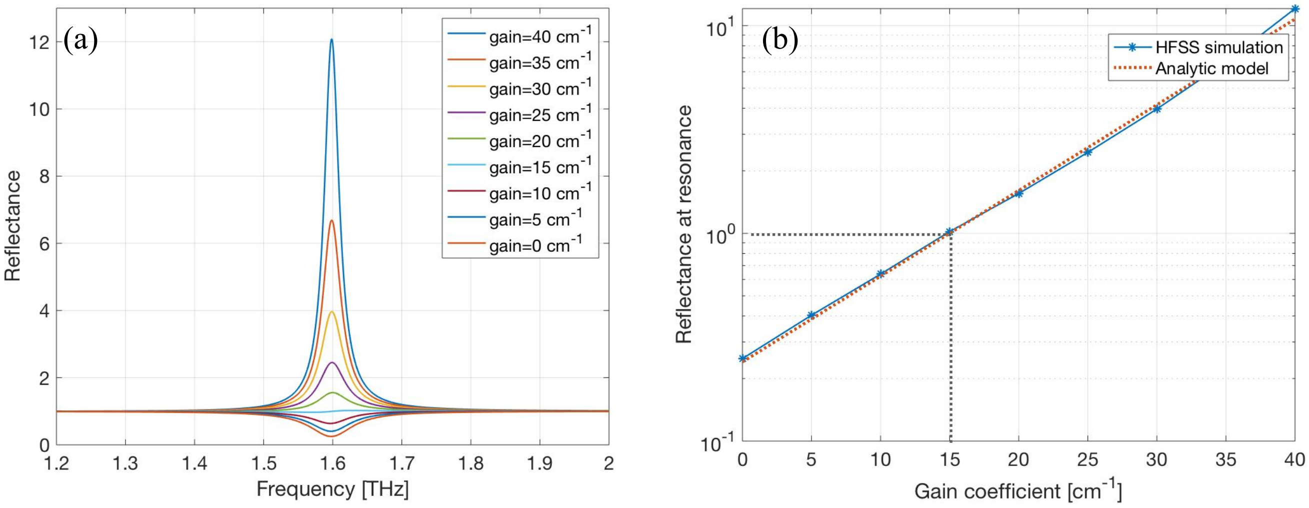

Figure 3.13 (a) Reflectance spectra of traditional metal-metal single-ridge metasurface with different gain coefficients, whose ridge width is designed to be 25.5 μm, thickness of gain medium is 3 μm and the spacing between waveguides is 60 μm. (b) Simulated reflectance (blue line) plotted in log scale with respect to gain coefficients, while red dotted line is the analytic fitting.

For comparison, traditional active metasurface made of metal-metal waveguides is modeled. Its resonance frequency is determined by the ridge width as $\nu = \dfrac{c}{2n_{GaAs}w}$, and to obtain the resonance frequency at 1.6 THz, the width of ridge waveguides is chosen to be $w = 25.5$ μm while the thickness of gain medium is 3 μm, the period between waveguides is 60 μm, the same as optimized LC MM waveguide design. As the uniform gain coefficient provided by quantum cascade active region increases, the reflectance at resonance frequency increases and becomes positive, enabling light amplification as shown in Fig. 3.13 (a). From the spectra, the transparency gain coefficient of traditional metal-metal waveguides needed to balance optical losses is around $g_{tr} = 15$ cm^{-1} indicated by the dotted lines in Fig. 3.13 (b). A commonly used analytic model of the metasurface can be represented by:

$$R_{MS} = R_1 G = e^{\xi(\nu)(g - g_{tr})}, \tag{3.4}$$

where $R_1 = e^{-\xi(\nu)g_{tr}}$ is the passive (unbiased) reflectance of the metasurface, and $R_1 = e^{\xi(\nu)g}$ is the intensity gain with g to be the intersubband gain coefficient. The spectral properties of the metasurface are reflected by the frequency dependent fitting factor $\xi(\nu)$, and after fitting the simulated reflectance using equation (3.4), which is depicted by the red dotted line in Fig. 3.13 (b), the fitting factor at resonance frequency is $\xi(\nu_r) = 0.095$ cm.

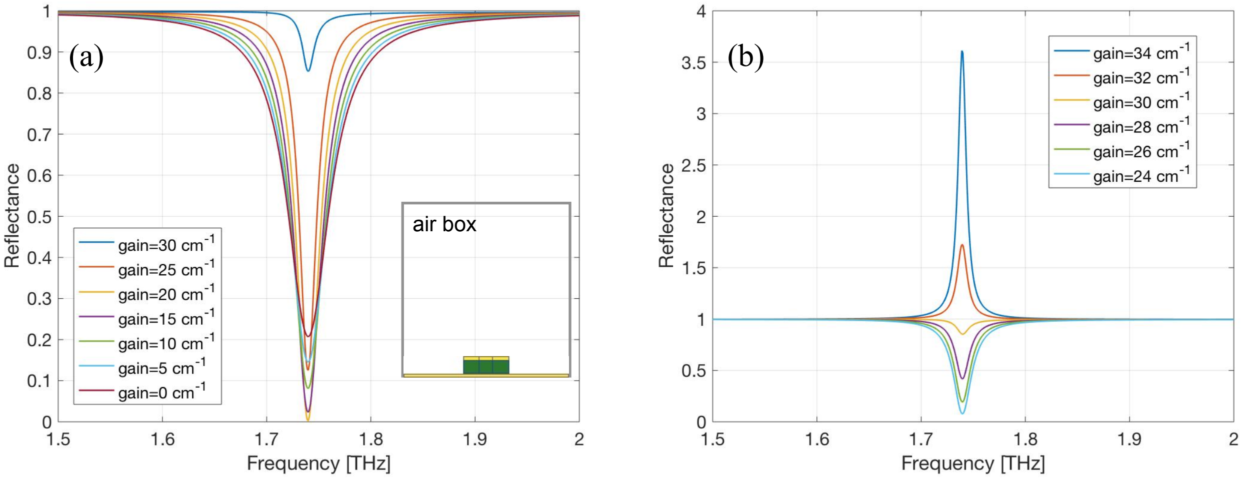

Figure 3.14. Reflectance spectra of LC circuit-based metal-metal waveguides with different gain coefficients in the case when no MgF_2 substrate is put above. The dimension of the LC MM waveguide is: l_{ind} = 28 μm, w_{ind} = 4 μm, l_{cap} = 6 μm, w_{cap} = 3 μm, h_{cap} = 3 μm and the period is 60 μm. The inset shows the side-view diagram of the simulation unit cell.

When LC circuit-based metal-metal waveguides are fabricated by etching holes along the traditional metal-metal waveguides, gain profile as well as transparency gain coefficient become different, and are studied through reflectance spectra at different gain coefficients. The structure applied in the simulation has the same design parameters as discussed in Section 3.3, except the slightly reduced length of capacitor plates in order to compensate for the frequency shift caused by the change of properties of GaAs layer. Light is first assumed to incident from free space, in which case, no optical absorption coming from MgF_2 substrate is taken into consideration yet, and the resonance frequency is therefore shifted from 1.6 THz in absence of the substrate. The spectra depicted in Fig. 3.14 (a) indicate that as gain coefficient increases, the LC resonant mode shows smaller bandwidth with lower minimum reflectance, before the reflectance increases and exceed unity. That is because, the passive LC MM waveguides work in under-coupling regime, $i.e.\ \gamma_r < \gamma_m + \gamma_{sc}$, as gain provided by semiconductor layer increases, it will first compensate for the material losses and transits the system to critical coupling condition, then into over-coupling regime, before the gain coefficient becomes large enough to build up an active metasurface. This is different from traditional metal-metal single-ridge metasurface which works in over-coupling regime with large radiative damping rate and therefore broadband reflectance and much lower quality factor. As gain coefficient increases in metal-metal single-ridge metasurface, the reflectance at resonance frequency keeps increasing (Fig. 3.13(b)), and the transparency gain coefficient is lower compared with that of LC MM waveguides which is $g_{tr} = 30$ cm^{-1} as shown in Fig. 3.14 (b).

If lossy MgF_2 substrate is assumed on top of the active metasurface, extra optical absorption in the 500 μm thick substrate increases the transparency gain. Simulated reflectance at resonance frequency with respect to gain coefficient provided by the active region is plotted in Fig. 3.15 (b) in log scale, where the reduction of reflectance around gain coefficient of 15 cm^{-1} demonstrates the system reaching critical coupling condition as the non-radiative damping rate is compensated by the optical gain. The transparency gain coefficient of LC MM waveguides is indicated by the dotted lines and is increased to $g_{tr} = 41$ cm^{-1} in the existence of lossy MgF_2 substrate. After fitting the simulated reflectance in the range of gain coefficient higher than 30 cm^{-1} using equation (3.4), the fitting factor at resonance frequency is $\xi(\nu_r) = 0.16$ cm (red dotted line in Fig. 3.15 (b))

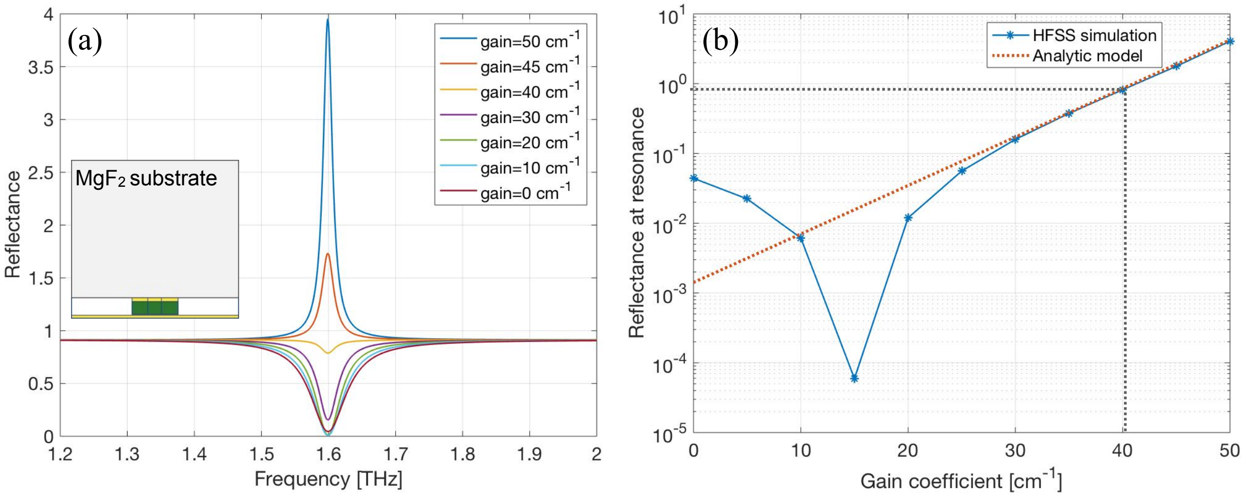

Figure 3.15 (a) Reflectance spectra of LC circuit-based metal-metal waveguides with different gain coefficients in the existence of lossy MgF$_2$ substrate, whose dimension is: l_{ind} = 28 μm, w_{ind} = 4 μm, l_{cap} = 6 μm, w_{cap} = 3 μm, h_{cap} = 3 μm and the period between waveguides is 60 μm. The inset shows the side-view diagram of the simulation unit cell. (b) Simulated reflectance (blue line) plotted in log scale with respect to gain coefficients, while red dotted line is the analytic fitting.

which is higher than that of a metal-metal single-ridge metasurface, leading to higher lasing threshold.

Finally, the antiferromagnetic FeF$_2$ film is added between the active metasurface and MgF$_2$ substrate. Rabi splitting is observed between strongly coupled AF magnons and metasurface-enhanced photons, while the transparency gain coefficient keeps increasing till $g_{tr} \approx 48$ cm^{-1} due to resonant absorption in FeF$_2$. The reflectance spectra are plotted in Figure 3.16 with respect to gain coefficient.

After the study of hybrid active metasurface/antiferromagnet system, several challenges towards the realization of magnon-polariton quantum cascade laser are concluded. First, comparing all the simulation results above, the lasing threshold of LC circuit-based metal-metal waveguide metasurface in existence of antiferromagnetic FeF$_2$ film grown on lossy MgF$_2$ substrate is

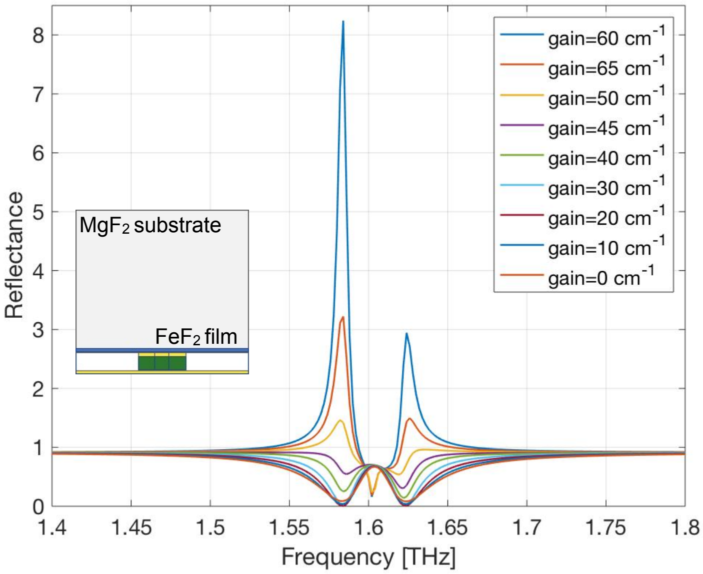

Figure 3.16 Reflectance spectra of LC circuit-based metal-metal waveguides at different gain coefficients. A 200 nm thick antiferromagnetic FeF$_2$ film with its MgF$_2$ substrate is put in proximity to the metasurface. The dimension of the LC MM waveguide is: l_{ind} = 28 μm, w_{ind} = 4 μm, l_{cap} = 6 μm, w_{cap} = 3 μm, h_{cap} = 3 μm and the period is 60 μm. The inset shows the side-view diagram of the simulation unit cell.

dramatically increased compared with traditional metal-metal single-ridge metasurface working at the same lasing frequency. The possible reason may be that the extremely small effective cavity volume supporting strongly coupled hybrid system leads to increasing metallic loss, which also explains the fact that LC resonators barely lase—most of achievable polaritonic applications based on LC MM microcavities are polariton emitters. Second, it is hard to design a quantum cascade laser working at a frequency as low as 1.6 THz because the intersubband energy separation between upper and lower lasing states becomes comparable with subband widths, which decreases the injection selectivity and therefore reduces population inversion. While in the simulations above, the lower frequency tail of broadband gain profile centered at 2 THz is assumed to enable light amplification at 1.6 THz. Third, only part of the thick MgF$_2$ substrate is included in the simulations, while in the full cavity simulation, a total thickness of 500 μm lossy MgF$_2$ substrate will result in more absorption loss as light bouncing back and forth in the laser cavity, leading to even higher lasing threshold. What's more, dispersion of light oscillating in the thick substrate will introduce FP fringes into the reflectance spectra and may overlap with the signals of magnon-polariton states.

Chapter 4: Nested Fabry-Pérot cavity approach to magnon-polariton

4.1 Background of nested Fabry-Pérot cavity

To reach the strong light-matter coupling regime, the energy coupling rate between the photon mode and the material excitation mode should be larger than the irreversible energy decay rate, therefore the electromagnetic resonators supporting vacuum states are expected to have a high quality factor. In a traditional Fabry-Pérot (FP) cavity, optical fields can pass through the cavity only when they are in resonance with it, and cavity eigenfrequencies are expressed as $v = m\frac{c}{2n_d L_{cav}}$, $m = 1,2,3\ldots$ According to the definition of quality factor, *i.e.* 2π times the ratio of the stored energy to the energy dissipated per oscillation cycle, a high quality cavity can be achieved by using high reflectivity surfaces to reduce the optical loss per round trip. A high quality factor FP cavity then becomes a good platform to study strong light-matter coupling system. Material excitations, such as magnon modes carried by antiferromagnetic insulators, can be introduced into the FP cavity and strongly couple with optical cavity modes once the criterion of strong coupling is satisfied. Frequency splitting, as a signature of strong coupling, can be demonstrated through transmission or reflection spectroscopy. One of the advantages of FP cavity is that it is easy to tune the cavity eigenfrequencies by changing the cavity length using a piezoelectric stage. The resonance frequencies of cavity photon modes can be tuned in resonance or off resonance with respect to intracavity material excitations, revealing hybrid dispersion relation of cavity polaritons once the system enters strong light-matter coupling regime.

This section will start with a model describing how optical cavity modes are affected by the intracavity dielectric slab compared with a traditional FP cavity. Then, I will introduce several antiferromagnetic insulators and theoretically study their behaviors in tunable FP cavities based on the knowledge of their optical properties and AF magnon properties. The dispersion of hybrid magnon-photon systems is recorded by tuning the cavity length. A discussion on possible magnon-polariton quantum cascade laser will be provided in the end.

4.2 Analytical model of nested FP cavity

When a dielectric slab is inserted into a traditional two-mirror FP cavity, the interfaces between air and dielectric act as additional mirrors which make the resonance condition of FP cavity more complicated since all multiple reflected beams among all individual mirrors have to be taken into account. A general theory for this kind of multimirror FP cavity or nested FP cavity problems has been developed using matrix method [108, 109] as suggested by the analysis of multilayer thin films. While in this chapter, the dielectric slab is supposed to be bonded with one of the mirrors and the combination of them can be viewed as an equivalent mirror showing different reflection and transmission coefficients at its front and back faces (Figure 4.1). In this way, the system is simplified as a traditional two-mirror FP cavity.

The effective reflection and transmission of the equivalent mirror are therefore not symmetric as light incident from different sides. If light is incident from air towards the dielectric side of the equivalent mirror, the reflection and transmission coefficients are:

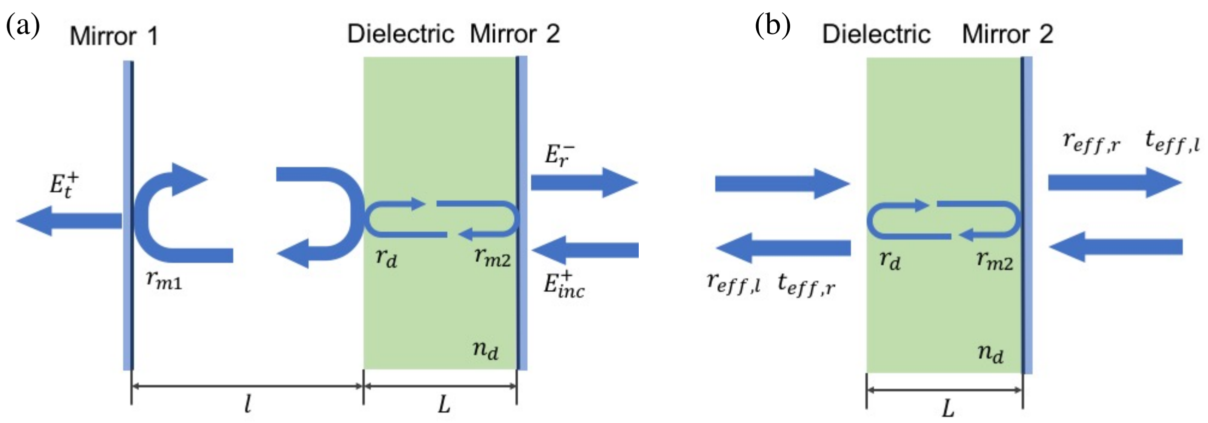

Figure 4.1 (a) Sketch of a nested FP cavity with dielectric slab inserted into a traditional two-mirror FP cavity, and the combination of dielectric slab and one of the mirrors acts as an equivalent mirror (b).

$$r_{eff,l} = -r_d + \frac{\left(1-r_d\right)\left(1+r_d\right) r_{m2} e^{2ik_dL}}{1-r_{m2}r_d e^{2ik_dL}},\ t_{eff,l} = \frac{\left(1-r_d\right)\left(1+r_{m2}\right) e^{ik_dL}}{1-r_{m2}r_d e^{2ik_dL}}. \quad (4.1)$$

If light is incident from air towards the mirror side, the reflection and transmission coefficients are:

$$r_{eff,r} = -r_{m2} + \frac{\left(1-r_{m2}\right)\left(1+r_{m2}\right) r_d e^{2ik_dL}}{1-r_{m2}r_d e^{2ik_dL}},\ t_{eff,r} = \frac{\left(1-r_{m2}\right)\left(1+r_d\right) e^{ik_dL}}{1-r_{m2}r_d e^{2ik_dL}}, (4.2)$$

where $r_d = \dfrac{n_d - 1}{n_d + 1}$, r_{m2} are the reflection coefficients of light illuminating from dielectric towards air and mirror respectively, while the reflection coefficients with reverse incident direction obtain an extra π phase shift. $k_d = n_d\dfrac{2\pi}{\lambda} + i\dfrac{\alpha_d}{2}$ is the effective wave vector of light propagating in the dielectric with index of refraction n_d and absorption coefficient of α_d. L is the thickness of the dielectric slab.

The reflection coefficient of the whole system is in the same form as a traditional two-mirror FP cavity, while the reflection and transmission coefficients of one of the mirrors are now replaced by that of the equivalent mirror obtained from above equations (4.1-4.2):

$$R = \frac{E_r^-}{E_{inc}^+} = r_{eff,r} + \frac{t_{eff,r} t_{eff,l} r_{m1} e^{2ik_0 l}}{1 - r_{eff,l} r_{m1} e^{2ik_0 l}}, \tag{4.3}$$

where k_0 and l are the wave vector of light in free space and length of cavity filled by air. r_{m1} is the reflection coefficient of another mirror consisting the FP cavity, which can be larger than unity if, instead of a traditional mirror, an active metasurface is used.

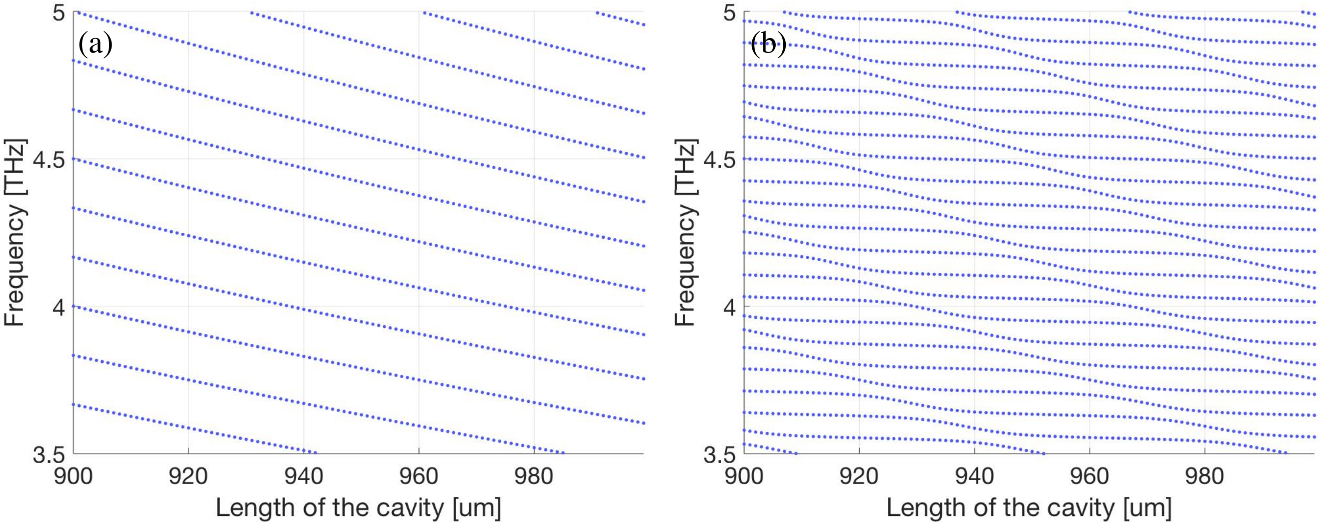

Figure 4.2. Cavity eigenfrequencies vs. cavity length for a traditional two-mirror FP cavity with (a) and without (b) intracavity dielectric slab.

Figure 4.2 shows Matlab simulation results on cavity eigenfrequencies of a FP cavity at different cavity lengths in the case when the cavity is entirely filled by air (a) or consists both air and dielectric slab (b). The reflectances of two mirrors (r_{m1}^2, r_{m2}^2) are supposed to be as high as 97% to achieving high quality factor. The thickness of dielectric slab is fixed at 500 μm with frequency-independent index of refraction $n_d = 3.8$, while the total length of the FP cavity is tuned, resulting in the shift of cavity eigenfrequencies. Compared with traditional two-mirror FP cavity, the optical cavity modes in the existence of an intracavity dielectric slab are not equidistant and show different cavity length dependences.

4.3 Strong coupling between FP cavity eigenmodes and AF magnon mode

If the dielectric slab inserted into the FP cavity is an antiferromagnetic insulator with excited magnon modes, the index of refraction n_d used in the above model is no longer a constant due to the frequency dependence of material excitations. As introduced in Section 1.2, material excitations like AF magnons can be characterized using a classical Lorentzian model with a magnetic susceptibility expressed as:

$$\chi_m = \frac{\mu_r \omega_r}{\omega^2 - \omega_r^2 - \frac{i\omega\omega_r}{Q_m}}, \tag{4.4}$$

where ω_r is the resonance frequency of AF magnon mode, μ_r and Q_m are the oscillator strength and quality factor used to characterize the intensity and lifetime of magnon mode respectively. The index of refraction used in the equations (4.1-4.3) is then modified by the Lorentzian shaped magnetic susceptibility as: $n_d = \sqrt{\epsilon_d \left(1 + \chi_m(\omega)\right)}$.

Several potential antiferromagnetic insulators have been briefly introduced in Section 1.2, while a detailed Lorentzian model characterizing their AF magnon modes will be provided below. CoO is one of the promising candidates with experimentally demonstrated magnon modes falling into THz frequency range. The easy-plane magnetic anisotropy makes it difficult to derive the analytical magnetic susceptibility from its complicated spin dynamics. However, a numerical expression can be obtained from experimental data. Figure 4.3 (a) shows the experimental far infrared absorption spectra of a (001)-oriented CoO single crystal measured at different temperatures provided in Ref. [110]. The overall absorption coefficient is contributed by both background absorption increasing with temperature and frequency, and resonant AF magnon absorptions, where the absorption peaks located around 146 cm^{-1} are attributed to the single magnon excitations. By fitting the experimental absorption coefficient at 2 K with a Lorentzian function (Fig .4.3 (b)), the unknown parameters used in the expression of magnetic susceptibility given in equation (4.4) are: $\omega_{AFMR}/(2\pi) = 4.44$ THz, $\mu_r = 0.00045$, $Q_{magnon} = 20$. The background absorption coefficient around magnon resonance frequency at 2K is obtained as $\alpha_d = 11$ cm^{-1}, while the permittivity of CoO is $\epsilon_d = 3.8^2$.

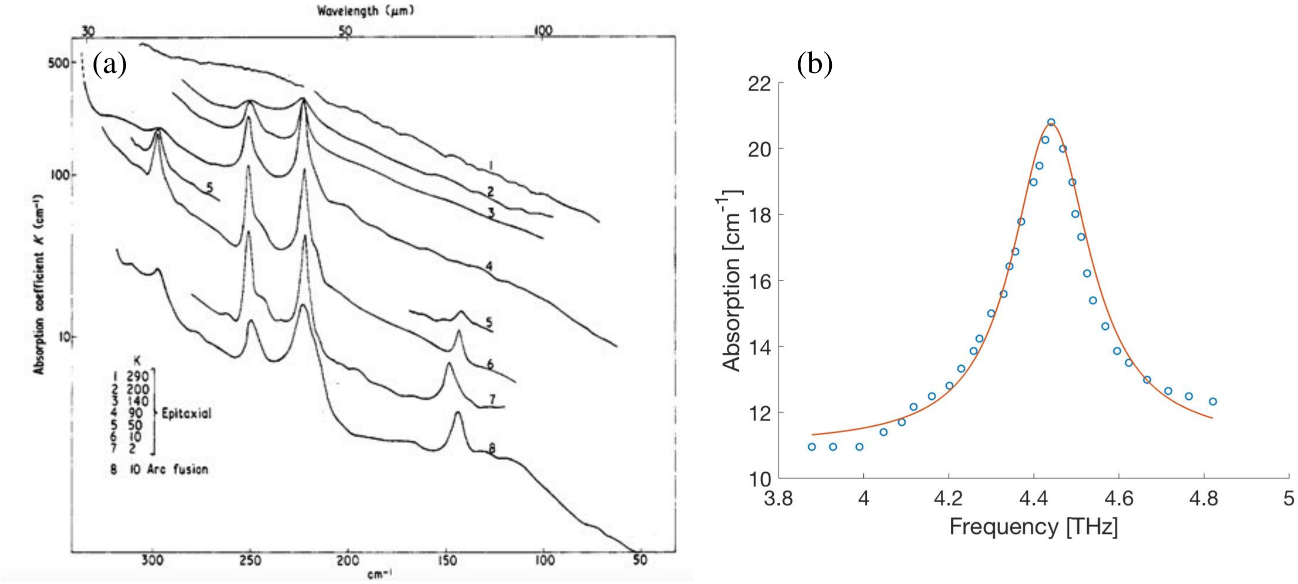

Figure 4.3 (a) Far infrared absorption in (001)-oriented CoO single crystal at different temperatures, while the value of curve 7 has been reduced by a factor of 3 for clarity. (b) Lorentzian fitting of one-magnon absorption in CoO at 2 K, *i.e.* curve 7 in (a), around 146 cm^{-1}.

Substituting the magnetic susceptibility of CoO into the expression of reflection coefficient given in equation (4.3), the reflectance spectrum of nested FP cavity with intracavity CoO slab is simulated by Matlab and is shown in Fig. 4.4 (a). The thickness of CoO slab is assumed to be 500 μm while the total thickness of the whole cavity is 825 μm. The short cavity length requires carefully designed mechanical mounts and high resolution piezoelectric stepper in future experiments, but also enables high overlapping between optical cavity modes and AF magnons, which promotes strong light-matter coupling.

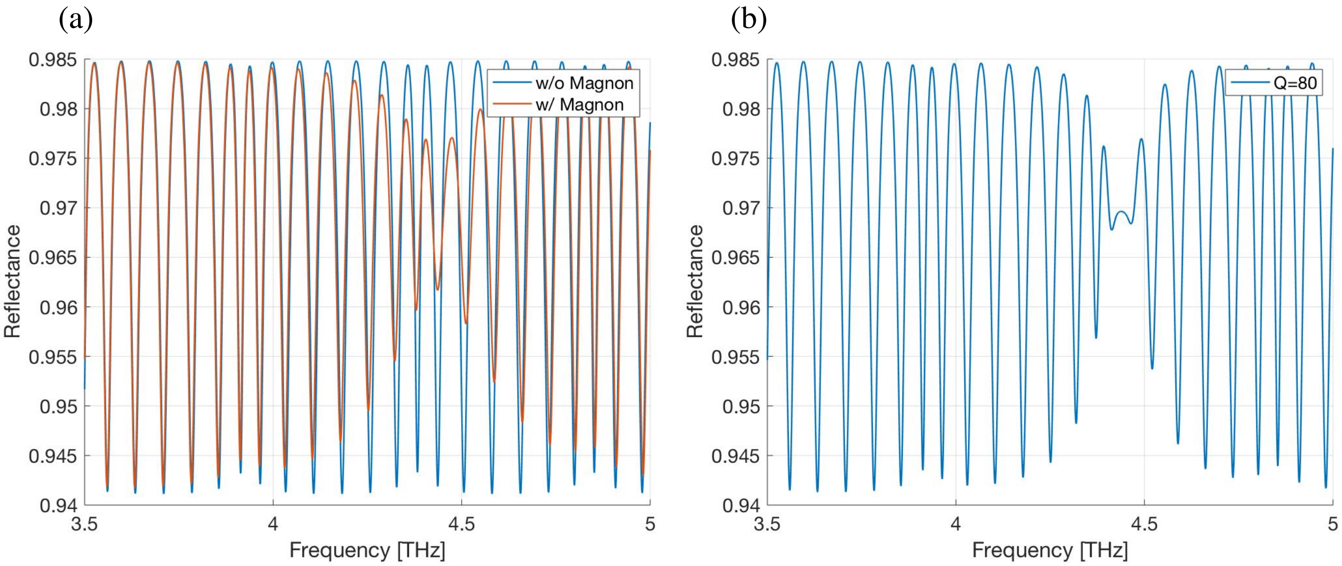

Figure 4.4. (a) Reflectance of nested FP cavity with intracavity CoO slab. Blue line and orange line represent spectra in the case when no magnon mode is excited in CoO and when magnon modes are excited. (b) Reflectance of nested FP cavity when the intracavity CoO has an artificial quality factor as high as 80.

In the case when the whole system is put at room temperature, there is no magnon mode excited in CoO and the reflectance spectrum with bare FP cavity eigenmodes is depicted by the blue line in Fig 4.4(a). When AF magnons are excited in CoO at liquid helium temperature, the linewidth of optical cavity eigenmodes located around magnon resonance frequency are slightly broadened and FP oscillations are decreased due to increasing round trip loss. However, no frequency splitting is observed. The possible reason is that a low quality factor and a small oscillator strength of the AF magnon mode in CoO obtained from the experimental datas lead to high energy decay rate but small light-matter coupling strength, which prevents the hybrid system from entering the strong light-matter coupling regime. As I artificially increase the quality factor used in the simulation from 20 to 80, frequency splitting of cavity eigenmodes occurs around the magnon resonance frequency, demonstrating the strong coupling between magnons and cavity photons in this case.

NiO is another promising antiferromagnetic material whose magnon properties as well as coherent interaction with light have been widely studied. Its parameters in the Lorentzian shaped magnetic susceptibility are obtained from Ref. [111] using a (111)-cut NiO single crystal, with the value of magnon frequency, oscillator strength and quality factor demonstrated to be $\omega_{AFMR}/(2\pi) = 1.1$ THz, $\mu_r = 0.0197$, $Q = 100$. The permittivity and absorption coefficient of NiO are assumed to be constants which are obtained from Ref. [112] around the values of: $\epsilon_d = 10$, $\alpha_d = 8$ cm^{-1}.

In knowledge of the optical properties of NiO, the reflectance spectra of nested FP cavity consisting 500 μm thick NiO and 330 μm long air can be obtained through equation (4.3) and are plotted in Figure 4.5. The left graph shows bare optical cavity modes when frequency-independent index of refraction with no magnon mode included, *i.e.* $n_d = \sqrt{\epsilon_d}$, is used in the simulation, and one of the cavity modes is designed around magnon resonance frequency in NiO, *i.e.* 1.1 THz. While the right graph plots the reflectance spectrum when Lorentzian shaped susceptibility is introduced into the expression of index of refraction $n_d = \sqrt{\epsilon_d\left(1+\chi_m(\omega)\right)}$, and as the cavity eigenfrequency is in resonance with the magnon frequency, the single reflection dip shown in Fig. 4.5 (a) splits, resulting in multiple new cavity eigenmodes and a reflectance around 97%, *i.e.* the reflectance of mirror 2, around magnon resonance frequency.

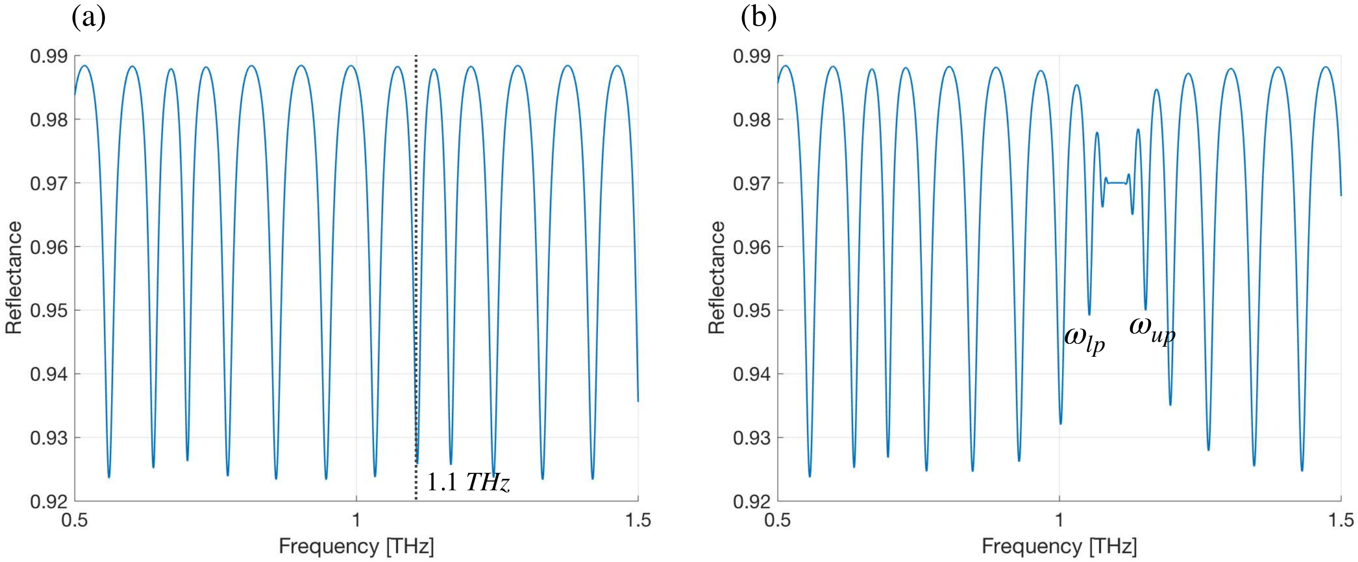

Figure 4.5 Reflectance of nested FP cavity with intracavity NiO in the case when no magnon excitation is considered (a) and when magnon excitations are included in the simulation (b).

To better understand the behavior of cavity eigenmodes near magnon resonance frequency, the dispersion relation of magnon-polaritons which has been derived in Section 1.1 is provided, while no decay term is included for simplicity (equation (1.6)):

$$(\beta c-\omega)(\omega_0-\omega)=\frac{\mu_r'\omega_0^2}{4},$$

Oscillator strength in this model is further scaled by an overlapping factor between optical mode which fills the entire cavity, including air and antiferromagnet, and magnon mode which is carried by the antiferromagnetic slab, $i.e.\ \mu_r'=\mu_r\dfrac{L}{L+l}$. The dispersion relation is plotted in Figure 4.6, where the x-axis labels the frequencies of incident EM wave while y-axis labels the frequencies of hybrid magnon-photon system. When optical field is in resonance with magnon mode, magnon-polaritons are generated revealed by the anticrossing and hybrid dispersion relations. Dashed lines point out the uncoupled cavity eigenfrequencies shown in Fig. 4.5 (a), while their intersections with hybrid dispersions (red dots) are new eigenmodes in the hybrid magnon-photon system.

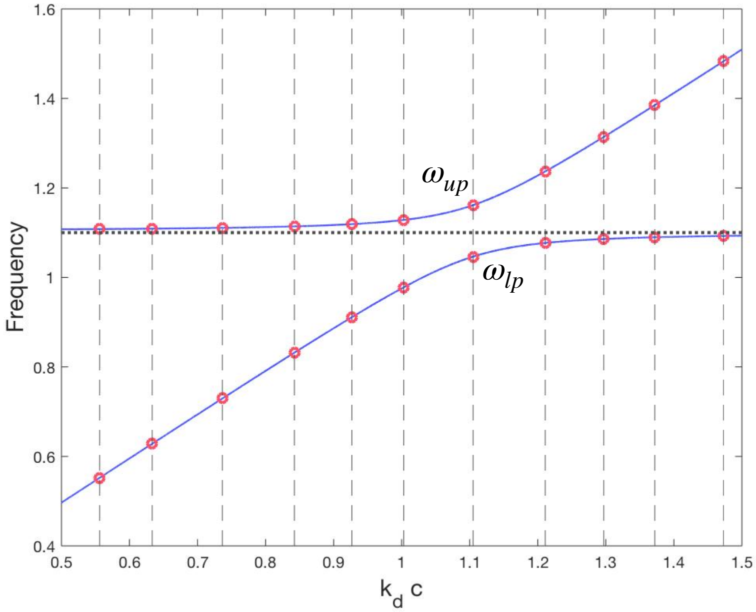

Figure 4.6 Dispersion relation of strongly coupled magnon-photon system. Vertical dashed lines and horizontal dotted line point out the uncoupled cavity eigenmodes and magnon mode respectively. Blue lines are the hybrid magnon-polariton modes. ω_{up} and ω_{lp} label the upper and lower polariton modes at resonance point.

If a single optical mode strongly interacts with AF magnon mode, two hybrid magnon-polariton states ω_{up}, ω_{lp} separated by the Rabi splitting at resonance point are expected to be observed in transmission or reflection measurements. However, in a FP cavity supporting multiple optical modes, extra modes both above and below the "polariton gap" occur, which come from the strong coupling between magnon mode and off-resonant optical cavity modes. These modes show lower intensity as the optical cavity modes are getting more and more off-resonant with respect to the magnon mode, and result in multiple small reflection dips between $\omega_{up}/(2\pi) \approx$ 1.15 THz and $\omega_{lp}/(2\pi) \approx 1.05$ THz shown in Fig. 4.5 (b), while as the incident frequency falls into the "polariton gap", no light could propagate through the antiferromagnetic slab, leading to flat reflectance with a value equals to the reflectance of the second mirror ($r_{m2}^2 = 97\,\%$). Rabi splitting obtained from the reflectance spectrum is around 0.1 THz which generally fits the analytical splitting derived from equation (1.6) in the case of no decay term, *i.e.* $\Omega_r = \sqrt{\mu_r'}\omega_{AFMR} \approx 120 \times (2\pi)$ GHz.

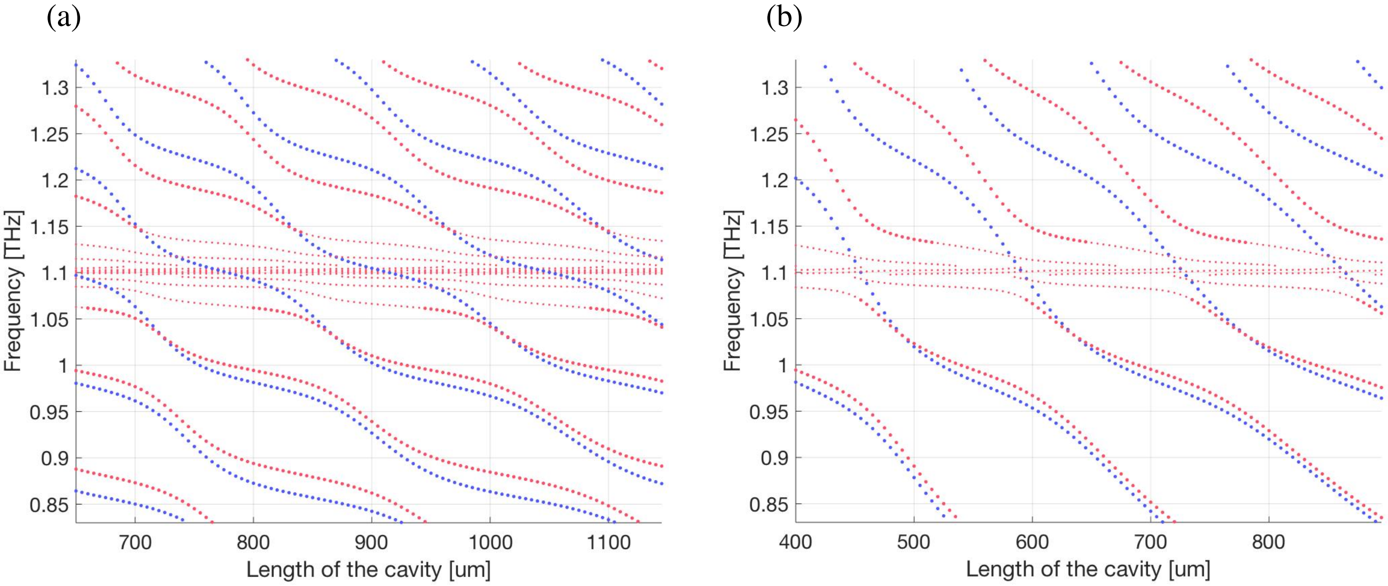

Figure 4.7 Cavity eigenfrequencies vs. cavity length. Blue dots represent uncoupled optical cavity modes, while red dots represent hybrid dispersion when strong coupling is realized between optical cavity photons and AF magnons in 500 μm NiO (a) and 250 μm NiO (b) respectively.

Hybrid dispersion relation of magnon-polaritons can be obtained by changing the cavity length using a piezoelectric stage which leads to the shift of cavity eigenfrequencies as well as the magnon-polariton modes correspondingly. Figure 4.7 provides the relationship of cavity eigenfrequencies with respect to cavity length. Blue dots are plotted as a reference in the case when no magnon mode is included, while red dots represent hybrid dispersion in the existence of magnon-polaritons. The size of dots is set to be proportional to the relative signal strength of the reflection dips, where numerous small dots between ω_{up} and ω_{lp} are attributed to extra modes coming from coupling between off-resonant cavity eigenmodes and magnon mode. Fig. 4.7 (a) shows the hybrid dispersions in the nested FP cavity consisting 500 μm NiO, while the thickness of NiO simulated in Fig. 4.7 (b) is reduced to 250 μm in order to reduce the total cavity length and increase the free space ranging. Sparser cavity eigenmodes then make it clear to distinguish the anticrossings between magnons and different ordered cavity modes.

4.4 Discussion on possible lasing behavior based on nested FP cavity

If one of the reflective mirrors used in the nested FP cavity is replaced by an active reflector with a reflectivity larger than unity, amplification and even lasing of intracavity polaritons is possible. A quantum cascade active region with intersubband transitions falling into THz frequency range could be inserted between metal-metal waveguides, and a array of metal-metal ridge waveguides would make up an active metasurface once population inversion is realized through external bias. If the active metasurface is further paired with an output coupler, a quantum cascade vertical external cavity surface emitting laser (QC-VECSEL) is built up, which shows the same geometry as a nested FP cavity if an antiferromagnetic slab is bonded with the output coupler. In this case, QC-VECSEL based magnon-polariton laser becomes possible once the intersubband gain in QC active region is large enough to compensate for the reflection loss from out coupler and light absorption in thick antiferromagnetic slab.

In general, the far-infrared AF properties of CoO are not well characterized, with only a few reports in the literature, and little understanding of the relationship between material quality and crystal growth techniques. However, if we simply consider the extracted parameters for CoO discussed in this section, the quality factor of CoO provided in Ref. [110] is too low to realize strong light-matter coupling; further experimental demonstrations of magnon mode in CoO crystal with different spin orientations or different growing methods are required. The AF magnon mode in NiO shows much higher quality factor and oscillator strength, and the phenomena of strong magnon-photon coupling have been theoretically predicted to be observable using THz spectroscopy. However, its magnon resonance frequency of 1.1 THz is too low for any intersubband transition based quantum cascade laser at this time.

Generally, in order to realize the novel magnon-polariton quantum cascade laser, several requirements have to be considered in choosing antiferromagnetic materials. First, AF magnons should have suitable quality factor and oscillator strength to enable the system entering strong light-matter coupling regime; second, magnon frequency should fall in the common QCL working frequency range, which is between 1.2 THz and 5.6 THz; third, the absorption coefficient in thick antiferromagnetic slab should be as low as possible to reduce the optical round trip loss in the FP cavity; moreover, existing growth technology has to be taken into consideration, since the thickness of antiferromagnetic slab should be comparable to the length of the FP cavity to ensure a large overlapping factor between the photon and the magnon modes. Once a suitable material is found, the possibility towards VECSEL-based magnon-polariton laser as well as polariton lasers based on other types of material excitations will be open.

Chapter 5: Conclusions

In this thesis, I have reviewed the basic definition of strong light-matter coupling in great detail with both classical and quantum mechanics descriptions, which has been realized in a wide range of material systems. Our study focuses on the exploitation of strong coupling between cavity photons and antiferromagnetic magnons, in order to compensate for the lack of study in the area of antiferromagnetic magnon-polaritons, as well as evaluate the feasibility of potential polaritonic devices working up to THz frequency. The application of polaritons on a novel type of laser source is highlighted, which has raised great attention nowadays. Based on our knowledge of quantum cascade THz laser sources, we are seeking the possibility of building a magnon-polariton quantum cascade laser.

The key components of this project are the selection of suitable antiferromagnetic materials and the special design of electromagnetic structures supporting magnon-polaritons. FeF_2 is considered to be one of the more promising candidates due to its magnon mode resonant at 1.6 THz and large magnon-photon interaction strength. Furthermore, it is possible to grow thin films of FeF_2 by molecular beam epitaxy, which opens the promise of integration with microfabricated devices. However, at this time only FeF_2 films of up to 200 nm thick are available which sets additional limitations on highly confining THz resonators. Metastructures, including split ring resonators and LC circuit-based metal-metal waveguides, are considered to be good approaches, which benefit from the strongly-confined evanescent magnetic field. In this thesis, I have proposed several candidate metasurface geometries, and the signatures of strong light-matter coupling have been observed in numerical simulations of hybrid antiferromagnet/metastructure systems, while further experimental demonstrations are under progress.

The compatibility of LC circuit-based metal-metal waveguides with semiconductor quantum well heterostructures makes the unique tripartite intersubband-magnon-photon coupling possible, which is demonstrated theoretically by the Rabi splitting between AF magnon mode and the lower branch of intersubband-polaritons.

When population inversion is further achieved via electrical pumping among the semiconductor quantum wells, magnon-polaritons confined in hybrid antiferromganet/metastructure are expected to get amplified or even lase. However, the predicted lasing threshold is much higher compared with that of a commonly used metal-metal single-ridge metasurface. The possible reason is that the geometry of LC MM waveguide was chosen with the goal of maximizing the quality factor of the metasurface - this condition is beneficial for the realiation of strong light-matter coupling. In this case, the radiative loss decreases dramatically, however, the metallic absorption increases in the highly confined subwavelength cavity and results in the increased lasing threshold as a trade-off. Further work is needed to fully optimize designs for both the observation of strong coupling and reduced lasing threshold.

Other promising antiferromagnetic materials with THz magnon resonances are also considered, e.g. CoO and NiO, for which bulk crystals are commercially available. A nested FP cavity concept has been developed integrating with these antiferromagnetic slabs to study their properties of magnon-phonon interaction. Finally the possibility of a QC-VECSEL based magnon-polariton laser is discussed, which will require suitable antiferromagnetic materials with high quality factor magnon modes falling into QCL working frequency as well as low absorption loss.

References

[1]L. Novotny, "Strong coupling, energy splitting, and level crossings: A classical perspective," *American Journal of Physics,* vol. 78, no. 11, pp. 1199-1202, 2010.

[2]P. Torma and W. L. Barnes, "Strong coupling between surface plasmon polaritons and emitters: a review," *Rep Prog Phys,* vol. 78, no. 1, pp. 013901-013935, 2015.

[3]G. Khitrova *et al.,* "Vacuum Rabi splitting in semiconductors," *Nature Physics,* vol. 2, pp. 81-90, 2006.

[4]G. Grynberg, A. Aspect and C. Fabre, "Introduction to Quantum Optics," New York, NY, USA: Cambridge, 2010.

[5]I. I. Rabi, "Space Quantization in a Gyrating Magnetic Field," *Physical Review,* vol. 51, no. 8, pp. 652-654, 1937.

[6]E. T. Jaynes and F. W. Cummings, "Comparison of quantum and semiclassical radiation theories with application to the beam maser," *Proceedings of the IEEE,* vol. 51, pp. 89-109, 1963.

[7]E. M. Purcell, "Spontaneous emission probabilities at radio frequencies," *Phys. Rev.,* vol. 69, p. 681, 1946.

[8]Y. Kaluzny, P. Goy, M. Gross, J. M. Raimond, and S. Haroche, "Observation of Self-Induced Rabi Oscillations in Two-Level Atoms Excited Inside a Resonant Cavity: The Ringing Regime of Superradiance," *Physical Review Letters,* vol. 51, no. 13, pp. 1175-1178, 1983.

[9]D. Meschede, H. Walther, and G. Muller, "One-atom maser," *Phys Rev Lett,* vol. 54, no. 6, pp. 551-554, 1985.

[10]M. G. Raizen, R. J. Thompson, R. J. Brecha, H. J. Kimble, and H. J. Carmichael, "Normal-mode splitting and linewidth averaging for two-state atoms in an optical cavity," *Phys Rev Lett,* vol. 63, no. 3, pp. 240-243, 1989.

[11]R. J. Thompson, G. Rempe, and H. J. Kimble, "Observation of normal-mode splitting for an atom in an optical cavity," *Phys Rev Lett,* vol. 68, no. 8, pp. 1132-1135, 1992.

[12]J. P. Reithmaier *et al.*, "Strong coupling in a single quantum dot-semiconductor microcavity system," *Nature,* vol. 432, no. 7014, pp. 197-200, 2004.

[13]K. Hennessy *et al.*, "Quantum nature of a strongly coupled single quantum dot-cavity system," *Nature,* vol. 445, no. 7130, pp. 896-9, 2007.

[14]E. Peter *et al.*, "Exciton-photon strong-coupling regime for a single quantum dot embedded in a microcavity," *Phys Rev Lett,* vol. 95, no. 6, p. 067401, 2005.

[15]A. Wallraff *et al.*, "Strong coupling of a single photon to a superconducting qubit using circuit quantum electrodynamics," *Nature,* vol. 431, no. 7005, pp. 162-167, 2004.

[16]A. Thomas *et al.*, "Ground-State Chemical Reactivity under Vibrational Coupling to the Vacuum Electromagnetic Field," *Angew Chem Int Ed Engl,* vol. 55, no. 38, pp. 11462-11466, 2016.

[17]J. G. E. Orgiu *et al.*, "Conductivity in organic semiconductors hybridized with the vacuum field," *Nat. Mater.,* vol. 14, pp. 1123-1130, 2015.

[18]T. Chervy *et al.*, "High-Efficiency Second-Harmonic Generation from Hybrid Light-Matter States," *Nano Lett,* vol. 16, no. 12, pp. 7352-7356, 2016.

[19]A. Imamoglu, R. J. Ram, S. Pau, and Y. Yamamoto "Nonequilibrium condensates and lasers without inversion: Exciton-polariton lasers," *Phys. Rev. A,* vol. 53, p. 4250, 1996.

[20]S. Christopoulos *et al.*, "Room-temperature polariton lasing in semiconductor microcavities," *Phys Rev Lett,* vol. 98, no. 12, p. 126405, 2007.

[21]D. S. Dovzhenko, S. V. Ryabchuk, Y. P. Rakovich, and I. R. Nabiev, "Light-matter interaction in the strong coupling regime: configurations, conditions, and applications," *Nanoscale,* vol. 10, no. 8, pp. 3589-3605, 2018.

[22]C. Weisbuch, M. Nishioka, A. Ishikawa, and Y. Arakawa, "Observation of the coupled exciton-photon mode splitting in a semiconductor quantum microcavity," *Phys Rev Lett,* vol. 69, no. 23, pp. 3314-3317, 1992.

[23]R. Ameling and H. Giessen, "Cavity plasmonics: large normal mode splitting of electric and magnetic particle plasmons induced by a photonic microcavity," *Nano Lett,* vol. 10, no. 11, pp. 4394-4398, 2010.

[24]S. Pau, G. Björk, J. Jacobson and Y. Yamamoto, "Phonon-polariton interaction in a microcavity," *Il Nuovo Cimento D,* vol. 17, pp. 1657-1662, 1995.

[25]Y. Tabuchi *et al.*, "Hybridizing ferromagnetic magnons and microwave photons in the quantum limit," *Phys Rev Lett,* vol. 113, no. 8, p. 083603, 2014.

[26]Y. Todorov *et al.*, "Strong light-matter coupling in subwavelength metal-dielectric microcavities at terahertz frequencies," *Phys Rev Lett,* vol. 102, no. 18, p. 186402, 2009.

[27]C. Kittel, "Introduction to solid state physics," 8th ed., New York, NY, USA: John & Wiley, 2004.

[28]F. Bloch, "Zur Theorie des Ferromagnetismus," *Z. Phys.,* vol. 61, pp. 206–219, 1930.

[29]A. V. Chumak, V. I. Vasyuchka, A. A. Serga, and B. Hillebrands, "Magnon spintronics," *Nature Physics,* vol. 11, no. 6, pp. 453-461, 2015.

[30]A. V. Chumak, "Fundamentals of magnon-based computing," arXiv: Mesoscale and Nanoscale Physics, 2019.

[31]A. Khitun, M. Bao, and K. L. Wang, "Magnonic logic circuits," *Journal of Physics D: Applied Physics,* vol. 43, no. 26, p. 264005, 2010.

[32]A. Khitun, "Multi-frequency magnonic logic circuits for parallel data processing," *Journal of Applied Physics,* vol. 111, no. 5, p. 054307, 2012.

[33]J. D. Adam, "Analog signal processing with microwave magnets," *Proc. IEEE,* vol. 76, p. 159, 1988.

[34]T. Seifert *et al.,* "Efficient metallic spintronic emitters of ultrabroadband terahertz radiation," *Nature Photon,* vol. 10, pp. 483–488, 2016.

[35]W. Jin *et al.*, "Raman fingerprint of two terahertz spin wave branches in a two-dimensional honeycomb Ising ferromagnet," *Nat Commun,* vol. 9, no. 1, p. 5122, 2018.

[36]T. Kampfrath *et al.*, "Coherent terahertz control of antiferromagnetic spin waves," *Nature Photonics,* vol. 5, no. 1, pp. 31-34, 2010.

[37]C. Braggio, G. Carugno, M. Guarise, A. Ortolan, and G. Ruoso, "Optical Manipulation of a Magnon-Photon Hybrid System," *Phys Rev Lett,* vol. 118, no. 10, p. 107205, 2017.

[38]C. Hahn *et al.*, "Measurement of the intrinsic damping constant in individual nanodisks of $Y_3Fe_5O_{12}$ and $Y_3Fe_5O_{12}|Pt$," *Applied Physics Letters,* vol. 104, no. 15, p. 152410, 2014.

[39]P. Pirro *et al.*, "Spin-wave excitation and propagation in microstructured waveguides of yttrium iron garnet/Pt bilayers," *Applied Physics Letters,* vol. 104, no. 1, p. 012402, 2014.

[40]Ö. O. Soykal and M. E. Flatte, "Strong field interactions between a nanomagnet and a photonic cavity," *Phys Rev Lett,* vol. 104, no. 7, p. 077202, 2010.

[41]Ö. O. Soykal and M. E. Flatté, "Size dependence of strong coupling between nanomagnets and photonic cavities," *Physical Review B,* vol. 82, no. 10, p. 104413, 2010.

[42]H. Huebl *et al.*, "High cooperativity in coupled microwave resonator ferrimagnetic insulator hybrids," *Phys Rev Lett,* vol. 111, no. 12, p. 127003, 2013.

[43]X. Zhang, C. L. Zou, L. Jiang, and H. X. Tang, "Strongly coupled magnons and cavity microwave photons," *Phys Rev Lett,* vol. 113, no. 15, p. 156401, 2014.

[44]R. W. Sanders, "Magnetic polariton, impurity mode enhancement, and superradiance effects in FeF2," *Solid State Communications,* vol. 28, pp. 907-910, 1978.

[45]T. Jungwirth, X. Marti, P. Wadley, and J. Wunderlich, "Antiferromagnetic spintronics," *Nat Nanotechnol,* vol. 11, no. 3, pp. 231-241, 2016.

[46]A. V. Kimel *et al.*, "Ultrafast non-thermal control of magnetization by instantaneous photomagnetic pulses," *Nature,* vol. 435, no. 7042, pp. 655-657, 2005.

[47]A. V. Kimel *et al.*, "Optical excitation of antiferromagnetic resonance inTmFeO$_3$," *Physical Review B,* vol. 74, no. 6, p. 060403-1, 2006.

[48]S. Baierl *et al.*, "Nonlinear spin control by terahertz-driven anisotropy fields," *Nature Photonics,* vol. 10, no. 11, pp. 715-718, 2016.

[49]T. F. Nova *et al.*, "An effective magnetic field from optically driven phonons," *Nature Physics,* vol. 13, no. 2, pp. 132-136, 2016.

[50]K. Grishunin *et al.*, "Terahertz Magnon-Polaritons in TmFeO$_3$," *ACS Photonics,* vol. 5, no. 4, pp. 1375-1380, 2018.

[51]M. Białek, A. Magrez and J. -. Ansermet, "Magnon-polaritons in dysprosium ferrite," 2019 44th International Conference on Infrared, Millimeter, and Terahertz Waves (IRMMW-THz), Paris, France, 2019, pp. 1-1.

[52]P. Sivarajah *et al.*, "THz-frequency magnon-phonon-polaritons in the collective strong-coupling regime," *Journal of Applied Physics,* vol. 125, no. 21, p. 213103, 2019.

[53]E. V. Gomonay and V. M. Loktev, "Spintronics of antiferromagnetic systems (Review Article)," *Low Temperature Physics,* vol. 40, no. 1, pp. 17-35, 2014.

[54]R. C. Ohlmann and M. Tinkham, "Antiferromagnetic Resonance in FeF_2 at Far-Infrared Frequencies," *Physical Review,* vol. 123, no. 2, pp. 425-434, 1961.

[55]M. T. Hutchings, "Spin waves in antiferromagnetic FeF_2," *J. Phys. C: Solid State Phys.,* vol. 3, p. 307, 1970.

[56]D. J. Lockwood, "Raman scattering from one-magnon excitations in FeF_2," *J. Phys. C: Solid State Phys.,* vol. 17, p. 6009, 1984.

[57]C. Manohar and G. Venkataraman, "Magnon-Photon Coupling in Antiferromagnets," *Physical Review B,* vol. 5, no. 5, pp. 1993-1999, 1972.

[58]H. Kondoh, "Antiferromagnetic resonance in NiO in Far-infrared region," *J. Phys. Soc. Jpn.,* vol. 15, p. 1970, 1960.

[59]D. J. Lockwood, M. G. Cottam and J. H. Baskey, "One- and two-magnon excitations in NiO," *Journal of Magnetism and Magnetic Materials,* vol. 104-107, pp. 1053-1054, 1992.

[60]T. Higuchi, N. Kanda, H. Tamaru, and M. Kuwata-Gonokami, "Selection rules for light-induced magnetization of a crystal with threefold symmetry: the case of antiferromagnetic NiO," *Phys Rev Lett,* vol. 106, no. 4, p. 047401, 2011.

[61]I. G. Austin and E. S. Garbett, "Far infrared electronic excitations of the Co^{2+} ions in antiferromagnetic CoO," *J. Phys. C: Solid State Phys.,* vol. 3, p. 1605, 1970.

[62]R. R. Hayes and C. H. Perry, "Magnetic excitations in cobalt oxide," *Solid State Communications,* vol. 14, pp. 173-175, 1974.

[63]H. h. Chou and H. Y. Fan, "Light scattering by magnons in CoO, MnO, and α-MnS," *Physical Review B,* vol. 13, no. 9, pp. 3924-3938, 1976.

[64]G. V. Kozlov *et al*., "Submillimeter backward-wave oscillator spectroscopy of the rare-earth orthoferrites," in *IEEE Transactions on Magnetics*, vol. 29, no. 6, pp. 3443-3445, 1993.

[65]A. V. Kavokin, J. J. Baumberg. G. Malpuech and F. P. Laussy, "Microcavities," New York, NY, USA: Oxford University Press, 2007.

[66]R. Colombelli and J.-M. Manceau, "Perspectives for Intersubband Polariton Lasers," *Physical Review X,* vol. 5, no. 1, p. 011031-1, 2015.

[67]H. Deng, G. Weihs, D. Snoke, J. Bloch, and Y. Yamamoto, "Polariton lasing vs. photon lasing in a semiconductor microcavity," *Proc Natl Acad Sci U S A,* vol. 100, no. 26, pp. 15318-15323, 2003.

[68]P. Bhattacharya, B. Xiao, A. Das, S. Bhowmick, and J. Heo, "Solid state electrically injected exciton-polariton laser," *Phys Rev Lett,* vol. 110, no. 20, p. 206403, 2013.

[69]C. Schneider *et al*., "An electrically pumped polariton laser," *Nature,* vol. 497, no. 7449, pp. 348-352, 2013.

[70]P. Bhattacharya *et al*., "Room temperature electrically injected polariton laser," *Phys Rev Lett,* vol. 112, no. 23, p. 236802, 2014.

[71]M. D. Fraser, S. Hofling, and Y. Yamamoto, "Physics and applications of exciton-polariton lasers," *Nat Mater,* vol. 15, no. 10, pp. 1049-1052, 2016.

[72]D. Dini, R. Kohler, A. Tredicucci, G. Biasiol, and L. Sorba, "Microcavity polariton splitting of intersubband transitions," *Phys Rev Lett,* vol. 90, no. 11, p. 116401, 2003.

[73]L. Sapienza *et al*., "Electrically injected cavity polaritons," *Phys Rev Lett,* vol. 100, no. 13, p. 136806, 2008.

[74]M. Scheller *et al.*, "Room temperature continuous wave milliwatt terahertz source," *Optics Express,* vol. 18, p. 27112, 2010.

[75]M. Geiser, G. Scalari, F. Castellano, M. Beck, and J. Faist, "Room temperature terahertz polariton emitter," *Applied Physics Letters,* vol. 101, no. 14, p. 141118, 2012.

[76]L. Sapienza *et al.*, "Photovoltaic probe of cavity polaritons in a quantum cascade structure," *Applied Physics Letters,* vol. 90, no. 20, p. 201101, 2007.

[77]P.-B. Vigneron *et al.*, "Quantum well infrared photo-detectors operating in the strong light-matter coupling regime," *Applied Physics Letters,* vol. 114, no. 13, p. 131104, 2019.

[78]G. Gunter *et al.*, "Sub-cycle switch-on of ultrastrong light-matter interaction," *Nature,* vol. 458, no. 7235, pp. 178-181, 2009.

[79]S. Zanotto *et al.*, "Ultrafast optical bleaching of intersubband cavity polaritons," *Physical Review B,* vol. 86, no. 20, p. 201302-1, 2012.

[80]A. A. Anappara *et al.*, "Signatures of the ultrastrong light-matter coupling regime," *Physical Review B,* vol. 79, no. 20, p. 201303-1, 2009.

[81]Y. Todorov *et al.*, "Ultrastrong light-matter coupling regime with polariton dots," *Phys Rev Lett,* vol. 105, no. 19, p. 196402, 2010.

[82]S. De Liberato and C. Ciuti, "Stimulated scattering and lasing of intersubband cavity polaritons," *Phys Rev Lett,* vol. 102, no. 13, p. 136403, 2009.

[83]J. M. Manceau *et al.*, "Resonant intersubband polariton-LO phonon scattering in an optically pumped polaritonic device," *Applied Physics Letters,* vol. 112, no. 19, p. 191106, 2018.

[84]K. Ohtani *et al.*, "An electrically pumped phonon-polariton laser," *Science Advances,* vol. 5, p.:eaau1632, 2019.

[85]M. Franckié, C. Ndebeka-Bandou, K. Ohtani, and J. Faist, "Quantum model of gain in phonon-polariton lasers," *Physical Review B,* vol. 97, no. 7, p. 075402, 2018.

[86]K. Unterrainer *et al*., "Quantum cascade lasers with double metal-semiconductor waveguide resonators," *Applied Physics Letters,* vol. 80, no. 17, pp. 3060-3062, 2002.

[87]R. A. Shelby, D. R. Smith, S. Schultz, "Experimental Verification of a Negative Index of Refraction," *Science,* vol. 292, p. 77, 2001.

[88]S. Linden *et al*., "Magnetic Response of Metamaterials at 100 Terahertz." *Science,* vol. 306, p.1351, 2004

[89]N. Katsarakis, T. Koschny, M. Kafesaki, E. N. Economou, and C. M. Soukoulis, "Electric coupling to the magnetic resonance of split ring resonators," *Applied Physics Letters,* vol. 84, no. 15, pp. 2943-2945, 2004.

[90]G. Scalari, *et al*., "Ultrastrong Coupling of the Cyclotron Transition of a 2D Electron Gas to a THz Metamaterial," *Science,* vol. 335, p. 1323, 2012.

[91]C. Maissen *et al*., "Ultrastrong coupling in the near field of complementary split-ring resonators," *Physical Review B,* vol. 90, no. 20, 2014.

[92]D. Dietze, A. Benz, G. Strasser, K. Unterrainer, and J. Darmo, "Terahertz meta-atoms coupled to a quantum well intersubband transition," *Optics Express,* vol. 19, p. 13700, 2011.

[93]A. Gabbay *et al*., "Interaction between metamaterial resonators and intersubband transitions in semiconductor quantum wells," *Applied Physics Letters,* vol. 98, no. 20, p. 203103, 2011.

[94]D. J. Shelton *et al*., "Strong coupling between nanoscale metamaterials and phonons," *Nano Lett,* vol. 11, no. 5, pp. 2104-2108, 2011.

[95]Gavin B. G. Stenning *et al*., "Magnetic control of a meta-molecule," *Optics Express,* vol. 21, p. 1456, 2013.

[96]B. Bhoi *et al*., "Study of photon–magnon coupling in a YIG-film split-ring resonant system," *Journal of Applied Physics,* vol. 116, no. 24, p. 243906, 2014.

[97]Y. Mukai, H. Hirori, T. Yamamoto, H. Kageyama, and K. Tanaka, "Antiferromagnetic resonance excitation by terahertz magnetic field resonantly enhanced with split ring resonator," *Applied Physics Letters,* vol. 105, no. 2, p. 022410, 2014.

[98]Y. Mukai, H. Hirori, T. Yamamoto, H. Kageyama, and K. Tanaka, "Nonlinear magnetization dynamics of antiferromagnetic spin resonance induced by intense terahertz magnetic field," *New Journal of Physics,* vol. 18, no. 1, p. 013045, 2016.

[99]Q. Shen, B. Hou, Z. Chen, and Z.-L. Wang, "Effect of gap width on enhanced magnetic optical fields in metallic split ring resonators," *AIP Advances,* vol. 2, no. 4, p. 042175, 2012.

[100]F. Yu, L. Zhang, H. Zhong, C. Deng and C. Zhang, "The birefringence property of magnesium fluoride crystal in THz frequency region," Proc. SPIE 7854, Infrared, Millimeter Wave, and Terahertz Technologies, 78541S, 2010.

[101]A. S. Husein, R. MS, Sri W. Suciyati, "Theoretical Analysis of Reflection and Refraction of Electromagnetic Waves on an Anisotropic, Inhomogeneous and Linear Medium," *arXiv: 1203.1725,* 2012.

[102]C. Walther, G. Scalari, M. I. Amanti, M. Beck, J. Faist, "Microcavity Laser Oscillating in a Circuit-Based Resonator," *Science,* vol. 327, p. 1495, 2010.

[103] C. Walther, G. Scalari, M. Beck, J. Faist, "Purcell effect in the inductor-capacitor laser," *Optics Letters,* vol. 36, p. 2623, 2011.

[104]M. Geiser *et al.*, "Strong light-matter coupling at terahertz frequencies at room temperature in electronic LC resonators," *Applied Physics Letters,* vol. 97, no. 19, p. 191107, 2010.

[105]M. Geiser *et al.*, "Ultrastrong coupling regime and plasmon polaritons in parabolic semiconductor quantum wells," *Phys Rev Lett,* vol. 108, no. 10, p. 106402, 2012.

[106]J. M. Manceau, S. Zanotto, I. Sagnes, G. Beaudoin, and R. Colombelli, "Optical critical coupling into highly confining metal-insulator-metal resonators," *Applied Physics Letters,* vol. 103, no. 9, p. 091110, 2013.

[107]J. M. Manceau *et al.*, "Mid-infrared intersubband polaritons in dispersive metal-insulator-metal resonators," *Applied Physics Letters,* vol. 105, no. 8, p. 081105, 2014.

[108]H. v. d. Stadt and J. M. Muller, "Multimirror Fabry–Perot interferometers," *Journal of the Optical Society of America A,* vol. 2, p. 1363, 1985.

[109]S. J. Hogeveen and H. v. d. Stadt, "Fabry-Perot interferometers with three mirrors," *Applied Optics,* vol. 25, p. 4181, 1986.

[110]T. Moriyama *et al.*, "Intrinsic and extrinsic antiferromagnetic damping in NiO," *Physical Review Materials,* vol. 3, p. 051402, 2019.

[111]Z. Thacker and P. J. Pinhero, "Terahertz Spectroscopy of Candidate Oxides in MIM Diodes for Terahertz Detection," *IEEE Transactions On Terahertz Science And Technology,* vol. 6, p. 414, 2016.